Stony Brook University

X-ray diffraction microscopy on frozen hydrated specimens

A Dissertation Presented

by

Johanna Nelson

to

The Graduate School

in Partial Fulfillment of the Requirements

for the Degree of

Doctor of Philosophy

in

Physics

Stony Brook University

August 2010

Stony Brook University

The Graduate School

Johanna Nelson

We, the dissertation committee for the above candidate for the Doctor of Philosophy degree, hereby recommend acceptance of this dissertation.

Chris Jacobsen – Dissertation Advisor
Professor, Department of Physics and Astronomy

Peter Stephens – Chairperson of Defense
Professor, Department of Physics and Astronomy

Marivi Fernandez Serra
Professor, Department of Physics and Astronomy

Markus Seeliger
Professor, Department of Pharmacological Sciences

This dissertation is accepted by the Graduate School.

Lawrence Martin
Dean of the Graduate School

Abstract of the Dissertation

X-ray diffraction microscopy on frozen hydrated specimens

by

Johanna Nelson

Doctor of Philosophy

in

Physics

Stony Brook University

2010

X-rays are excellent for imaging thick samples at high resolution because of their large penetration depth compared to electrons and their short wavelength relative to visible light. To image biological material, the absorption contrast of soft X-rays, especially between the carbon and oxygen K-shell absorption edges, can be utilized to give high contrast, high resolution images without the need for stains or labels. Because of radiation damage and the desire for high resolution tomography, live cell imaging is not feasible. However, cells can be frozen in vitrified ice, which reduces the effect of radiation damage while maintaining their natural hydrated state.

X-ray diffraction microscopy (XDM) is an imaging technique which eliminates the limitations imposed by current focusing optics simply by removing them entirely. Far-field coherent diffraction intensity patterns are collected on a pixelated detector allowing every scattered photon to be collected within the limits of the detector's efficiency and physical size. An iterative computer algorithm is then used to invert the diffraction intensity into a real space image

with both absorption and phase information. This technique transfers the emphasis away from fabrication and alignment of optics, and towards data processing.

We have used this method to image a pair of freeze-dried, immunolabeled yeast cells to the highest resolution (13 nm) yet obtained for a whole eukaryotic cell. We discuss successes and challenges in working with frozen hydrated specimens and efforts aimed at high resolution imaging of vitrified eukaryotic cells in 3D.

Contents

List of Figures

List of Tables

Acknowledgements

I wish to thank the X-ray Microscopy research group at Stony Brook University including Christian Holzner, Rachel Mak, Holger Fleckenstein, Bjorg Larson, Simon Moser, Benjamin Hornberger, and especially those in diffraction microscopy: Jan Steinbrener, Xiaojing Huang, Huijie Miao, Josh Turner, and Andrew Stewart. I also want to acknowledge Sue Wirick at the NSLS at Brookhaven National Lab and my thesis advisor Chris Jacobsen.

Thanks to Aaron Neiman and his entire lab in the Department of Biochemistry and Cell Biology for all of their help with the yeast and immunolabeling. I would also like to thank Jim Quinn in Material Science and Engineering for the SEM imaging and Rosanne Csencsits at Donner Lab in Berkeley, CA for help with the cryo TEM. Also a big thanks to Janos Kirz, Stefano Marchesini, David Shapiro, and David Sayre.

The biological imaging work is funded by the National Institute for General Medical Services at the National Institutes for Health under Contract 5R21EB6134. The XDM methods and instrumentation development is funded by the Division of Materials Sciences and Engineering, Office of Basic Energy Sciences, at the Department of Energy under Contract DE-FG02-07ER46128. The XDM experiments were conducted at the Advanced Light Source, which is supported by the Director, Office of Science, Office of Basic Energy Sciences, of the U.S. Department of Energy under Contract No. DE-AC02- 05CH11231.

Finally, I wish to thank my family for all of their support.

Chapter 1

X-ray microscopy

Since the first recorded x-ray image taken by Wilhelm Conrad Röntgen in 1895, the interaction of X-rays with matter has been exploited by astronomers, physicians, biologists, chemists, comic book heros, and even art historians. X-rays span the electromagnetic spectrum from 100 eV to 200 keV where energies below several keV are considered "soft" and X-rays with higher energies are "hard" X-rays. The wavelength range of X-rays is from approximately 10 nm to less than 0.01 nm or 0.1 Ångstroms since a photon's energy E is related to its wavelength λ by

$$E = \frac{hc}{\lambda} = \frac{1239.842}{\lambda} \text{ eV} \cdot \text{nm}, \tag{1.1}$$

where Planck's constant $h = 4.136 \times 10^{-15}$ eV·s and the speed of light $c = 2.998 \times 10^8$ m/s. This wavelength range places X-rays between the wavelengths of visible light (350 to 650 nm) and electrons (2.43×10^{-3} nm for 510 keV).

1.1 X-rays interaction with bulk matter

The macroscopic interaction of x-rays with bulk matter including both refraction and absorption can be described by the complex refractive index which is conventionally[1] defined as

$$\tilde{n} = 1 - \delta - \mathrm{i}\beta, \tag{1.2}$$

where δ and β are positive, real numbers that are small compared to unity [1] and the equation for a time dependent wave propagating in the positive z

[1] Alternatively the complex refractive index can be defined as $\tilde{n} = 1 - \delta + \mathrm{i}\beta$; in this case a wave would propagate in the $+z$ direction as $I = I_0 e^{\mathrm{i}(kz - \omega t)}$

direction is

$$I = I_0 e^{-\mathrm{i}(kz-\omega t)}. \tag{1.3}$$

The positive parameters δ and β, called the refractive index decrement and the absorption index respectively [2], depend on both the bulk material and the frequency or wavelength of the interacting X-rays. The former quantifies how X-rays bend while the latter describes the removal or absorption of X-rays. The complex refractive index is relates to the real refractive index n, which is the quantity that describes how light is bent by a material, by

$$\tilde{n} = n(1 + \mathrm{i}\kappa), \tag{1.4}$$

where κ is the attenuation index [3] or extinction coefficient of the medium.

The change in phase velocity v of an electromagnetic wave due to the interaction with matter can be described in terms of Maxwell's equation as

$$v = \frac{c}{\sqrt{\mu_\mathrm{m}\epsilon}}. \tag{1.5}$$

For nonmagnetic material ($\mu_\mathrm{m} = 1$), the complex refractive index relates to the complex dielectric constant $\tilde{\epsilon}$ by

$$\tilde{n} = \sqrt{\tilde{\epsilon}} = 1 - \frac{n_\mathrm{a} r_\mathrm{e} \lambda^2}{2\pi}(f_1 + \mathrm{i}f_2), \tag{1.6}$$

where n_a is the number of atoms per unit volume, r_e is the classical electron radius, and $f = f_1 + \mathrm{i}f_2$ is the atomic scattering factor for the forward scattering direction [4]. We can rewrite δ and β in terms of these parameters as

$$\delta = \frac{r_\mathrm{e}\lambda^2}{2\pi} n_\mathrm{a} f_1 \tag{1.7}$$

and

$$\beta = \frac{r_\mathrm{e}\lambda^2}{2\pi} n_\mathrm{a} f_2. \tag{1.8}$$

The atomic scattering factors for 92 elements ($Z = 1 - 92$) were calculated for the energy range 50 eV to 30 keV by Henke *et al.* in 1993 [5].

1.1.1 Phase shift and absorption

Using the complex refractive index we can describe the phase shift and absorption of a wave propagation through a medium. Consider the plane wave $\psi_0 e^{-\mathrm{i}kz}$ propagating in the positive z direction through a medium of refractive

index $\tilde{n}$

$$\psi(z) = \psi_0 e^{-\mathrm{i}\tilde{n}kz} = \psi_0 e^{-\mathrm{i}(1-\delta-\mathrm{i}\beta)kz}$$
$$\psi(z) = \psi_0 e^{-\mathrm{i}kz} e^{-\beta kz} e^{\mathrm{i}\delta kz}. \tag{1.9}$$

To emphasize the attenuation and the phase advance of the plane wave through the distance z, we can write Equation 1.9 in terms of the absorption coefficient

$$\mu = 2\beta k = \frac{4\pi\beta}{\lambda} \tag{1.10}$$

and the phase change

$$\phi(z) = \delta kz = \frac{2\pi}{\lambda}\delta z, \tag{1.11}$$

where the wave number is $k = \frac{2\pi}{\lambda}$, leading to

$$\psi(z) = \left[\psi_0 e^{-\mathrm{i}kz}\right] e^{-\mu z/2} e^{\mathrm{i}\phi(z)}. \tag{1.12}$$

The transmission intensity of the wave is

$$I = |\psi(z)|^2 = \psi_0^2 e^{-2\beta kz} = \psi_0^2 e^{-\mu z}. \tag{1.13}$$

1.1.2 Penetration depth

With the absorption coefficient μ in hand, we can calculate the penetration distances of X-rays though specific material. Figure 1.1 shows the penetration depth in both water (in blue) and protein (in green) at which the X-ray intensity has dropped to e^{-1}, in other words, when depth $z = \frac{1}{\mu}$. For comparison, the mean free paths λ for both elastic (solid line) and inelastic (dashed line) scattering of electrons in these materials are also plotted where again the curves are colored blue and green for water and protein respectively.

With this plot one can see that X-rays with energies greater than 200 eV can travel much longer distances through material in contrast to electrons. Furthermore, as X-ray energy increases the penetration depth continues to length; however, for electrons the penetration depth begins to plateau with increased energy. For this reason, electron microscopes are severely limited by the short mean free path of the electron through the object of interest. Doubling the electron energy does not double the allowable object thickness.

Finally, notice the two drastic jumps in penetration depths depending on the X-ray energy. These jumps occur when a new absorption energy level for ejecting an inner-shell electron for the particular element is crossed, in this case the carbon (284 eV) and oxygen (540 eV) K-shell edges. When an atom

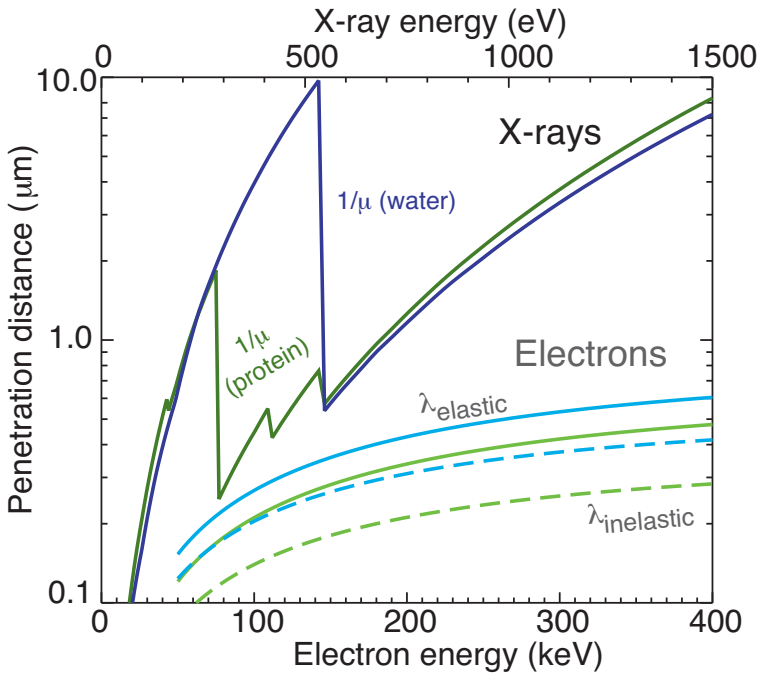

Figure 1.1: Penetration distance in water and protein of X-rays and electrons. The dark green and blue curves are the penetration depth of X-rays in protein and water respectively. The light blue and green lines are the mean free paths for electrons in protein and water respectively, where the solid lines are for elastic scattering and the dashed lines are the depths for inelastic scattering. The plot is modified from Kirz *et al.* [4] which calculated the X-ray penetration distances using data from Henke *et al.* [5] and the mean free paths λ for elastic and inelastic electron scattering using the approximate expressions of Langmore and Smith [6].

absorbs a photon an electron is ejected from one of the inner-shells and an electron from a higher shell moves down to fill the hole. A larger energy is required to eject an electron which is in a shell closer to the nucleus and therefore more tightly bound. These X-ray absorption edges allow contrast between different materials, such as protein and water in this particular case, to be maximized by tuning the X-ray energy used for imaging. In addition, finely measured energy scans across a particular edge can reveal information about the chemical makeup of the specimen at each image pixel (x-ray absorption near edge structure or XANES). No such chemical specificity or tuning of contrast can be done in electron microscopy, though inelastic electron scattering provides chemical information for sub-100 nm thick specimens.

1.2 X-ray sources

The first x-ray sources were x-ray vacuum tubes which operate by colliding electrons into metal targets to produce a continuous spectrum of *Bremsstrahlung* and peaked x-ray fluorescence emission characteristic of the target. Since then other more efficient tabletop x-ray sources have emerged; however, for high resolution imaging especially in 3D, synchrotron sources which have orders of magnitude higher brightness than even the best tabletop sources are crucial. Synchrotron radiation is typically produces in the lab either by changing the direction of the electrons gradually with bending magnets or by sending electrons through an insertion device such as a wiggler or undulator. An insertion device is a set of periodic magnetic structures which cause the electrons to undulate as they travel between them. The synchrotron radiation from a bending magnet or wiggler is a broad energy spectrum, while the radiation from an undulator interferes coherently producing sharp peaks of energies at harmonics from the fundamental energy. The fundamental energy can be changed by increasing or decreasing the distance between the two sets of periodic magnets. See for example Thompson *et al.* [2].

1.3 Zone plate imaging

One of the most oft used focusing optics for x-ray microscopy is the Fresnel zone plate. A zone plate is a circular diffraction grating with alternating absorbing, phase shifting material and transparent zones whose widths decrease with increased distance from the center such that the path difference of adjacent zones to the first order focus is a wavelength (Fig. 1.2). The distance

from the center of a zone plate to the edge of the n^{th} zone is given by

$$r_n^2 = mnf\lambda + \frac{m^2n^2\lambda^2}{4}, \tag{1.14}$$

where m is the diffractive order, f is the focal length of the lens, and λ is the wavelength. Since a zone plate is a diffractive optic, the incident light is focused into different orders with focal distances $f_m = f_1/m$. For the case of zone plates with opaque and transparent zones, the majority of incident light is absorbed (50%) or passes through unfocused into the $m = 0$ order (25%). The rest of the radiation is divided between the positive and negative odd numbered orders where the sign of the order indicates the direction of the diffracted light with respect to the direction of the incident wave. Even numbered orders have theoretically zero intensity because of destructive interference, though variations and imperfections in the zones leads to light in the even diffraction orders. Only 10% of the total X-rays are focused to the first order for an ideal zone plate. Zone plates fabricated with zones which are phase shifting instead of completely absorbing can have 4× higher theoretical efficiency; therefore, first order focus efficiency of 40% [7]. In reality, first order focus efficiencies are around 15 – 30% [8]. The first order is the order that is typically used and all other orders are blocked by the use of a central stop and pinhole aperture placed downstream of the optic (Fig. 1.3).

Fresnel zone plates are monochromatic lenses which obey the thin lens equation

$$\frac{1}{s_{\text{o}}} + \frac{1}{s_{\text{i}}} = \frac{1}{f}, \tag{1.15}$$

where s_{o} and s_{i} are the object and image distance respectively, for on and near-axis imaging. The larger the spectral bandwidth of the incident beam, the fewer zone N required before chromatic aberrations become significant

$$mN < \frac{\lambda}{\Delta\lambda}. \tag{1.16}$$

The resolution Δ_t of an ideal zone plate, as for any lens, is set by its numerical aperture $\text{NA} = \sin\theta$, where θ is the half angle for a source at infinity (Fig. 1.2). As defined by Rayleigh, the resolution Δ_t is given by

$$\Delta_t = \frac{0.61\lambda}{\text{NA}} \simeq \frac{1.22\lambda f_m}{D} = \frac{1.22\Delta_{r_N}}{m}, \tag{1.17}$$

where the diameter of the zone plate is related to the outermost zone width

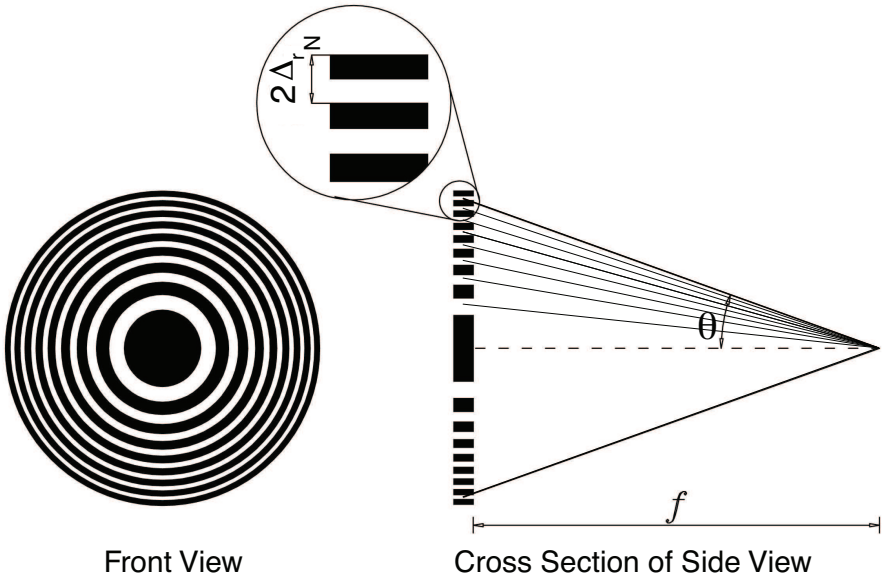

Figure 1.2: Front and side views of a zone plate schematic. Constructive interference of light from adjacent zones focuses the light to odd numbered focal length orders. The outer most zone width Δ_{r_N} determines the theoretical resolution of the optic. Image modified from the original courtesy of Beetz [9].

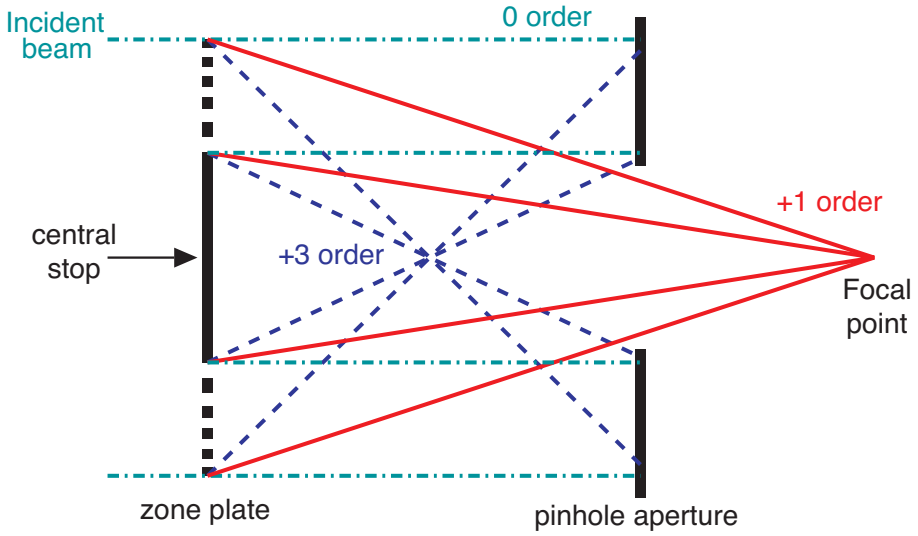

Figure 1.3: Schematic of a zone plate with central stop and pinhole aperture for blocking all but the desired first order focus. The central stop blocks the unfocused zero order which would otherwise pass through the pinhole aperture. Modified from original image courtesy of Kirz *et al.* [4].

$\Delta_{r_n} \equiv r_N - r_{N-1}$ by

$$D = 4N\Delta_{r_N} \tag{1.18}$$

and the m^{th} order focal length is given by

$$f_m = \frac{4N(\Delta_{r_N})^2}{\lambda m}. \tag{1.19}$$

Thus the resolution of a zone plate is theoretically determined by the width of the outermost zone and can be improved by fabricating lenses with finer zones or by imaging with a higher zone plate order at the cost of further reducing the efficiency of the optic [10]. To date, the finest resolved feature demonstrated using a Fresnel zone plate was 12 nm using soft x-rays. Unfortunately, the optics efficiency was only 0.6% [11]. Although higher efficiency focusing optics for X-rays exist such as Kirkpatrick-Baez mirrors and glass capillaries, they are not image preserving and therefore cannot be used as objective lenses.

1.4 X-ray microscopy of biological material

With the deep penetration depth of X-rays compared to electrons highlighted in Fig. 1.1, high resolution imaging of biological material with thicknesses of more than a few hundred nanometers becomes conceivable. Most bacteria fall in the 0.2 to 10 μm thickness range while many plant, animal, and fungi cells extend to 100 μm; therefore the majority of biological electron microscopy is performed on cells and tissue which have been sliced to fall within the penetration depths of transmission electron microscopes.

1.4.1 Resolution limited by radiation damage

For biological imaging one cannot forget that x-ray radiation is ionizing. As noted in Sec. 1.1.2, the absorption of an X-ray results in the ejection of an inner-shell electron. This hole is subsequently filled from a more loosely bound electron and the energy difference is release either in the form of an Auger electron or a fluorescence photon. The absorption of the initial photon creates a chain of secondary and tertiary damage primarily in the form of electrons and (in hydrated specimens) hydrogen gas (H^+) and hydroxide (OH^-) free radicals.

While higher level damage is hard to quantify and tends to be exceedingly sample dependent, primary radiation damage can be measured in terms of the energy deposited per unit mass or the absorbed skin dose

$$D = \frac{N}{A}\frac{\mu E}{\rho}, \tag{1.20}$$

where N is the number of incident photons, A is the irradiated area, μ is the absorption coefficient, E is the energy of the photons, and ρ is the density of the material. This is only a calculation of the dose on the surface of the material, but succeeding layers will have a reduced dose as photons are absorbed. Dose is measured in Grays, where 1 Gray = J/kg.

Although very low resolution, very low dose x-ray imaging on live patients is routinely done in the medical field, a dose of around 3 Gray is enough to kill about half the cells in a colony [12], effectively preventing even moderate resolution x-ray imaging of cells without causing lethal damage. For imaging hydrated, room temperature, living cells doses between $10^4 - 10^5$ Gray are possible before damage is visible (see for example Kirz *et al.* [4]). For true high resolution imaging, samples must either be dehydrated or ideally frozen hydrated. A frozen hydrated sample has been shown to withstand skin doses greater than 10^{10} Gray [13]. The dose required to image a 50 nm protein cube

in 10 μm thick ice is around 10^5 Gray, assuming a signal to noise ratio greater than or equal to five (Rose criterion) and 100% efficient optics and detector [4]. However, the required dose for imaging to a resolution d has been found to scale as an inverse third (d^{-3}) or fourth power law (d^{-4}) depending on the coherence of the system [14]. In other words, to improve the resolution from 50 nm to 25 nm the required imaging dose increases by around an order of magnitude.

Figure 1.4 shows an estimate of the ultimate resolution limit of x-ray microscopy using experimental damage studies to define a maximum tolerable dose before damage is visible and assuming Rose criterion and an inverse fourth power law scaling of resolution to dose [14]. The yellow region is the required radiation dose for x-ray imaging of non-crystalline material at both 1 keV and 10 keV. The blue area is the radiation dose up to which no damage is visible at the imaging resolution. The crossing of these two regions at approximately 10 nm gives an estimate for the resolution limit for damage-free hard X-ray imaging.

This plot gives a ballpark estimate of the expected resolution that radiation dose sets on x-ray microscopy of biological material, but it is also important to remember that radiation damage is known to be heavily sample dependent and a measure of dose is not directly related to the resulting damage. For example, it has been shown that imaging at cryogenic temperatures can prevent mass loss in Poly(methyl methacrylate) (PMMA) film, but does not prevent the breaking of the carbon oxygen double bonds [15]. Furthermore, the use of radioprotectants and free radical scavengers such as 1,4-benzoquinone in crystallography has shown to result in a ninefold improvement of the radiation hardiness of certain crystals [16].

Most of the damage studies used in Fig. 1.4 were performed by tracking Bragg-spot fading in diffraction patterns from crystals at cryogenic temperatures with either 8 to 13.1 keV X-rays or 100 keV electrons. On the other hand, the three x-ray microscopy studies shown in the plot were taken using 0.52 keV X-rays on either frozen hydrated cells showing no radiation damage from the dose required to image [13, 17] or by observing the degradation from radiation damage of diffraction patterns from freeze-dried, room temperature cells [14]. It is not clear that comparing such vastly different radiation studies is meaningful.

1.4.2 "Water window" imaging

For high resolution biological imaging, one must also consider the energy at which the x-ray imaging is performed. Figure 1.4 considers only hard x-rays where phase contrast dominates, but absorption contrast is minimal. The

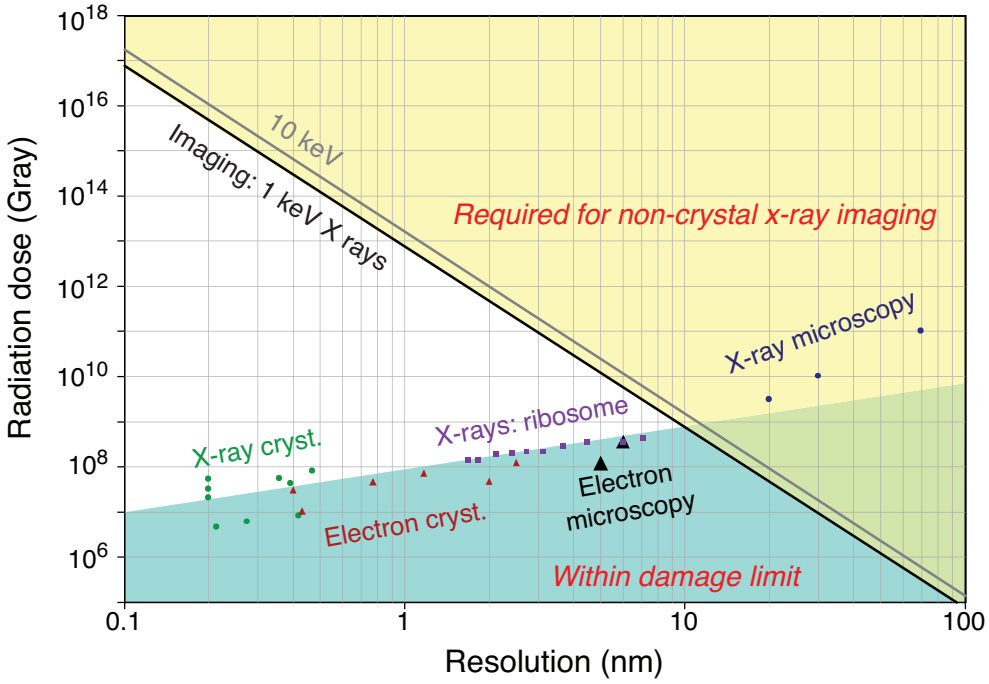

Figure 1.4: Graph comparing tolerable dose (blue region) and required dose for non-crystal coherent x-ray imaging (yellow region). The lower black line is the minimum dose for imaging with 1 keV X-rays and the upper gray line is for 10 keV imaging. For artifact-free imaging one should remain in the green overlapping region. This limits the resolution of non-crystal hard x-ray imaging to approximately 10 nm. [14]

frozen hydrated x-ray microscopy experiments considered [13, 17] utilized soft x-rays in the "water window" for imaging. Recall the jumps in penetration distance through water and protein in Fig. 1.1 that are due to the K-shell absorption edges for carbon and oxygen. The "water window" is the energy region in between those edges where the contrast between carbon and oxygen is large. Figure 1.5 plots the required skin dose for imaging a 20 nm protein cube in 5 μm ice in the "water window." The doses required for both phase and absorption contrast are significantly lower in these regions. The phase contrast drops again between 1 and 10 keV and levels off, but not to a dose as low as for the energies just below the 540 eV edge.

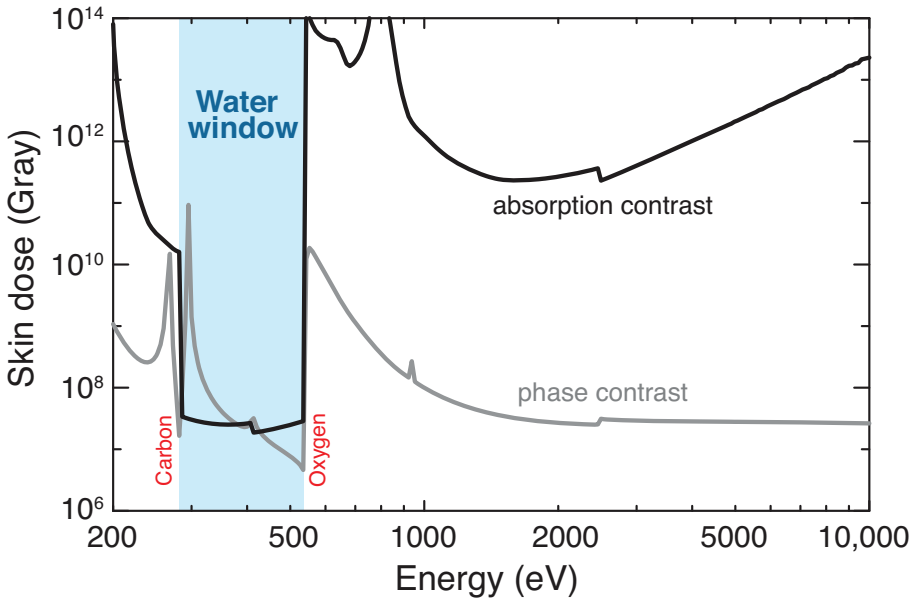

Figure 1.5: Plot of skin dose required to image a 20 nm protein structure in 5 μm of ice at different x-ray energies. The region highlighted in blue between the carbon and oxygen K-shell absorption edges is termed the "water window" for its ideal protein to water contrast for both absorption and phase. Imaging of frozen hydrated organic material is typically done in this soft x-ray energy region. Adapted from plot by Chris Jacobsen.

Considering how sample dependent radiation damage has shown to be and the added absorption contrast between carbon and oxygen when imaging in the "water window," the damage free area in blue may extend higher for x-ray imaging of frozen hydrated biological material with soft X-rays. Nevertheless, there is no expectation of damage-free imaging of non-crystalline biological

samples below 1 nm resolution.

1.5 Contributions of this dissertation

The work presented in this dissertation was performed in a research group environment with members contributing to particular aspects of the project. My contributions include the following:

- leading the experiments in XDM of chemically dried [18], freeze-dried [19], and frozen hydrated yeast at beamline 9.0.1 at the ALS, including the preparation of specimens, from January 2008 through May 2010,
- developing a nanogold labeling protocol for reliable surface labeling, including SEM imaging of labeled yeast (Sec. 3.1),
- contributing to the reconstruction of the freeze-dried yeast described in Sec. 3.3,
- analyzing the correlative microscopy between the reconstructed XDM and STXM images (Sec. 3.4.1),
- performing correlative microscopy of surface labeling on the reconstructed XDM and SEM of the freeze-dried yeast, including the Fresnel propagation of the XDM reconstruction (Sec. 3.4.2),
- performing two independent measurements of the resolution of the reconstruction of the freeze-dried yeast described in Sec. 3.5,
- analyzing the effects of a poor support constraint using experimental data as well as comparing the performance of two different reconstruction algorithms (Sec. 3.6),
- contributing to a test of bubbling in x-ray microscopy of frozen, organic samples using the cryo TXM at BESSY II (Sec. 4.1.1),
- designing, installing, and testing an in-vacuum visible light microscope (Sec. 4.2.2),
- calculating the possible contribution of higher energies in the 520 eV x-ray illumination in our XDM system and simulating the effects (Sec. 4.3),
- contributing to a platform independent reconstruction code [20],
- and contributing to a shared code archive of common post-reconstruction data analysis routines.

Chapter 2

X-ray diffraction microscopy

X-ray diffraction microscopy (XDM), also called coherent diffractive imaging, is a high resolution lensless imaging technique that forgoes the use of optics which can be inefficient and resolution limiting as discussed in Sec. 1.3. Coherent far-field diffraction intensities are collected from a non-crystalline structure and an iterative computer algorithm is used to reconstruct the real-space image of the object. In the present chapter, we will motivate the use of XDM, outline its requirements, and describe our experimental setup for XDM at the Advanced Light Source (ALS) in Lawrence Berkeley National Lab (LBNL) in Berkeley, CA.

2.1 Lensless imaging

In Sec. 1.3 it is mentioned that an ideal phase shifting Fresnel zone plate has only a 40% efficiency for its first order focus and that higher order foci are even less efficient. Furthermore, we know that the ultimate resolution limit for biological x-ray imaging is not diffraction limited, but limited by the tolerable radiation dose of the sample (Sec. 1.4.1). It is therefore prudent to attempt to detect all photons which have interacted with the specimen. Standard, full-field microscopy is done with a condenser lens which focuses light onto the sample and an objective lens behind to form an image from the light scattered off the sample. Although in x-ray microscopy the focusing optic used as the condenser lens can be a high efficiency optic such as a capillary, the image forming objective lens must be a Fresnel zone plate. This requirement for full-field x-ray imaging (called x-ray transmission microscopy or TXM) directly translates to a loss of 60% of the X-rays scattered from the sample for even the most perfect zone plate.

Figure 2.1 shows schematics for transmission x-ray microscopy (TXM)

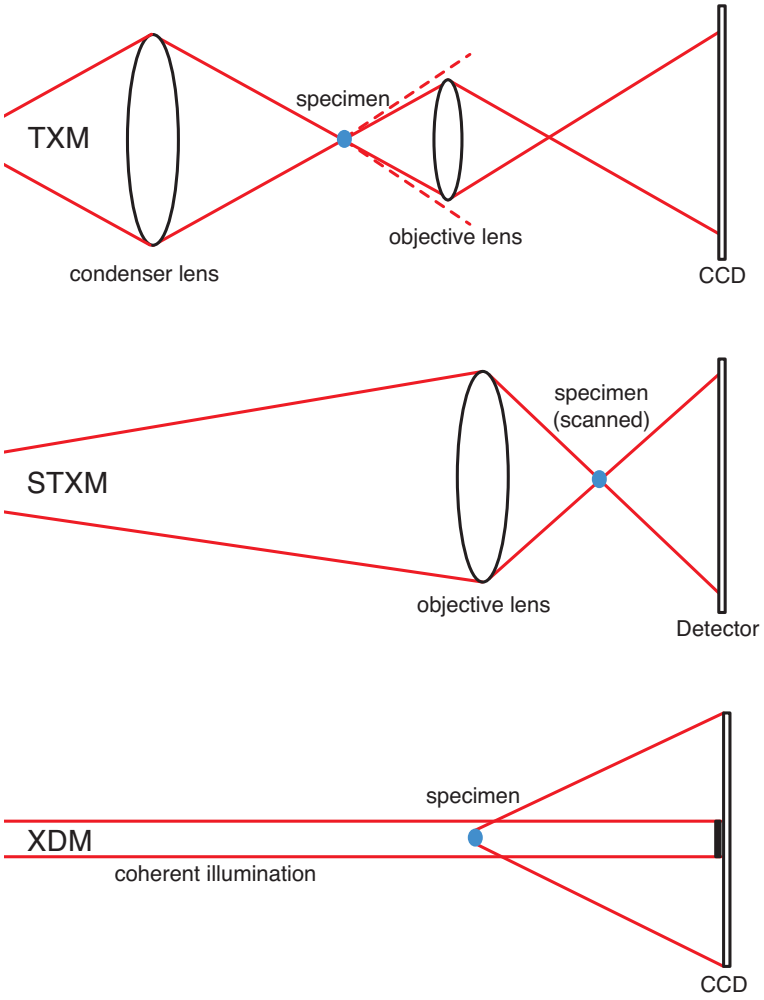

Figure 2.1: Diagram of three different x-ray imaging techniques: transmission x-ray microscopy (TXM), scanning transmission x-ray microscopy (STXM) and x-ray diffraction microscopy (XDM). TXM requires the most dose to the specimen because a zone plate objective lens must be placed between the specimen and the CCD detector. The technique's resolution is primarily limited by the numerical aperture of the objective lens since light scattered to higher angles (represented as dashed, red lines) are not collected by the objective. STXM significantly reduces the required dose to the specimen; however, the specimen must be raster scanned through the illumination. The resolution is limited by the size of the focus and the motion of the scanning motors. XDM requires no lenses, but a coherent illumination and a method of retrieving the real-space image. The theoretical resolution limit of this technique is the extend of the far-field intensity pattern collected and the maximum dose tolerated by the specimen.

and two other alternative imaging techniques scanning transmission x-ray microscopy (STXM) and x-ray diffraction microscopy (XDM). Both alternatives eliminate the need for a zone plate behind the sample. The first alternative, STXM, uses a lens to focus X-rays into a very small spot onto the specimen. The specimen is then raster scanned[1] and transmitted X-rays are collected. A pixel in the final image corresponds to a single illuminated location on the specimen. This technique reduces the total dose required for an image, but the resolution depends not only on the focal spot on the specimen, but also the reliability of the position of the scanned sample. The second alternative, XDM, requires a coherent illumination source (typically assumed to be plane wave) and the far-field diffraction intensities are collected on a CCD detector. This technique requires the least dose [21] and the resolution is theoretically limited only by the extent of the diffraction intensity pattern collected and the dose tolerated by the specimen.

2.2 Finding the missing phases

The idea behind x-ray diffraction microscopy is to replace the microscope's lens with a computer which would perform the phasing of the lens. Unfortunately, a CCD detector records intensity, but not phase. In this section we will discuss the missing phase problem and how this information can be recovered through iterative algorithms if the proper sample of the diffraction intensities are recorded.

2.2.1 Fraunhofer diffraction in the Born approximation

Assuming the distance from a scattering object to the detector plane is long compared to the size of the object, the Fraunhofer or far-field diffraction limit can be used. Furthermore, if we have a weakly scattering object the first-order Born approximation simplifies the far-field scattering to be the Fourier transform of the scattering potential of the object

$$\psi(x,y) \sim \int_{x'}\int_{y'} o(x',y') e^{-\mathrm{i}2\pi(f_x x' + f_y y')} \mathrm{d}x' \mathrm{d}y' = \mathcal{F}\{o(x',y')\} \tag{2.1}$$

where the scattering potential is defined as

$$o(x,y) = \frac{k^2}{4\pi}[1 - \tilde{n}^2(x,y)] \simeq \frac{k^2}{2\pi}[\delta(x,y) + \mathrm{i}\beta(x,y)], \tag{2.2}$$

[1]This scanning is in contrast to how scanning is done in scanning electron microscopes (SEM) where the electron beam is scanned and the specimen is held in place.

$f_x = \frac{x}{\lambda z}$ and $f_y = \frac{y}{\lambda z}$ are spatial frequencies [3], and the two dimensional Fourier transform and its inverse are defined as

$$\mathcal{F}\{g(x,y)\} = G(f_x, f_y) = \int\int g(x,y) e^{-\mathrm{i}2\pi(f_x x + f_y y)} \mathrm{d}x \ \mathrm{d}y \tag{2.3}$$

and

$$\mathcal{F}^{-1}\{G(f_x, f_y)\} = g(x,y) = \int\int G(f_x, f_y) e^{\mathrm{i}2\pi(f_x x + f_y y)} \mathrm{d}f_x \ \mathrm{d}f_y. \tag{2.4}$$

For a more detailed outline of far-field scattering within the first-order Born approximation see Appendix A.

The first-order Born approximation is valid in the limit that the object's thickness $t < 2\pi\lambda C/|\delta + i\beta|$, where $C \sim 0.2$ [22]. Assuming a cell that is a mixture of 20% protein, 20% lipid, and 60% water the first-order Born approximation limits the thickness of a biological sample to approximately 5 μm for 520 eV X-rays. However, at 5 keV this same material could be over 30 μm thick. Therefore, even relatively large samples can be considered weakly scattering if the energy of the incident X-ray is increased.

Since the scattering potential of an object is related to the far-field scattering by a Fourier transform, it follows that if one can measure this scattering from an unknown object then the object can be directly calculated by an inverse Fourier transform. In x-ray diffraction microscopy the scattering from an object that is plane wave illuminated is collected on a CCD detector. Assuming the object is small compared to the distance to the camera and the scattering is weak, which is easily achievable for cells, the scattering intensity that is recorded is

$$I(x,y) = |\psi(x,y)|^2 \sim |\mathcal{F}\{o(x',y')\}|^2. \tag{2.5}$$

Unfortunately, because the intensities (or magnitudes squared) of the complex scattered wave $|\psi(x,y)|^2 = |Ae^{\mathrm{i}\phi}|^2 = A^2$ are measured, a simple inverse Fourier transform is not sufficient for retrieving the object. The missing phase information $e^{\mathrm{i}\phi}$ must first be recovered. This is the classic phase problem which is not unique to x-ray diffraction microscopy.

2.2.2 Proper sampling of coherent diffraction intensities

In 1952, Sayre wrote a short, yet far-reaching paper which argued that if the Patterson function of a single unit cell is Shannon sampled then direct determination of structures in crystallography could be achieved [23]. The

implications of this statement to x-ray diffraction microscopy may not be directly apparent without further explination. The Patterson function is the Fourier transform of the measured diffraction intensities

$$\mathcal{F}^{-1}\{|Ae^{i\phi}|^2\} = \mathcal{F}^{-1}\{|\mathcal{F}\{o(x',y')\}|^2\} = \mathcal{F}^{-1}\{|O(f_x,f_y)|^2\}, \tag{2.6}$$

which is by definition the autocorrelation of $o(x,y)$. The autocorrelation is defined as the cross-correction of function with itself

$$(g \star g)(x) = \int g(x')g^*(x'-x)\mathrm{d}x' \tag{2.7}$$

(see for example Goodman [24]). For a compact object, the autocorrelation is twice the size of the object in each dimension.

The Nyquist-Shannon sampling theory, which was first introduced by Nyquist in 1928 [25] and was proven by Shannon over 20 years later [26], states that to properly sample a signal one must measure with a frequency which is at least twice that of the the highest frequency. In other words, if the highest frequency of a signal is $1/a$ then one must measure at points separated by $2/a$ or less. Without proper sampling, aliasing can occur.

To Shannon sample the autocorrelation of an object or diffracted intensities, one must oversample the object or the diffracted amplitudes by twofold. Practically this translates to having a sufficiently compact specimen such that its width W in either dimension is small enough so that the coherence width of the incident beam is at least $2W$ [27]. This is twice the required coherence width of a Young's double slit experiment with a slit space of W.

2.2.3 Coherence

The coherence of a electromagnetic wave includes both its temporal (or longitudinal) and spatial (or transverse) coherence. The first relates to the wave's finite bandwidth or energy resolution, while the second to the transverse distance over which phases are correlated. An ideal, monochromatic plane wave is perfectly coherent both temporally and spatial.

The temporal coherence is the temporal interval over which the phase of the wave is predictable at a given point in space. As noted in Sec. 1.2, undulator x-ray sources have sharply peaked energy harmonics. The inverse of the energy bandwidth of the n^{th} harmonic is given as

$$\frac{\lambda}{\Delta\lambda} \simeq nN, \tag{2.8}$$

where N is the number of magnetic periods. The beamline 9.0.1 undulator at the Advanced Light Source that is the x-ray source for our microscope has 43 periods and we currently image using exclusively the third harmonic. Thus before any further monochromitizing, the inverse of the intrinsic bandwidth of that harmonic is $\frac{\lambda}{\Delta\lambda} = 129$. For high resolution imaging a narrower bandwidth is required.[2] A discussion of the microscope's monochromator system and the resulting monochromaticity is given in Sec. 2.3.1.

In the previous section (Sec. 2.2.2), it was concluded that the required spatial coherence must be twice the length of the object. According to the van Citter-Zernike theorem one can achieve the required coherence from an incoherent, quasi-monochromatic source with an aperture such as a pinhole (see for example Born and Wolf [3]). For a circular aperture the degree of coherence is proportional to the first-order Bessel function relating the size of the pinhole and the distance from it. The first coherence minimum from a pinhole of radius r at a distance z in the far-field is a separation of width of

$$d_{\text{coh}} = \frac{0.61\lambda z}{r}. \tag{2.9}$$

Assuming our current microscope setup of a 5 μm pinhole approximately 25.4 mm from the specimen, the coherence length spans to a width of 7.4 μm for 520 eV illumination. This limits the object size to around 3.7 μm, which compares nicely with the 4.6 μm limit assumed by the first-order Born approximation (Sec. 2.2.1) at 520 eV for a frozen hydrated cell. To lengthen the coherence width a smaller pinhole or a longer pinhole to specimen distance could be used, but the illumination on the specimen would be reduced. For a detailed discussion of the validity of the van Cittert-Zernike theorem for our partially coherent, quasi-monochromatic source and an experimental measurement of our microscope's coherence length see Chapter 2 of [28].

2.2.4 Phase retrieval

An iterative approach to solving the phase problem was first proposed and demonstrated by Gerchberg and Saxton in 1972 [29] in electron microscopy where the magnitude information from both the image and Fourier planes are known. The algorithm iterates between enforcing the two known parameters, moving between the real and reciprocal spaces by Fourier transforms. Six years later Fienup reworked the Gerchberg-Saxton algorithm to fit the specific knowns of the phase problem of measuring only far-field diffraction intensities

[2] To image a 3 μm wide object at 10 nm resolution a coherence of $\lambda/\Delta\lambda \geq 300$ is required [18].

and suggested a more robust algorithm for noisy data [30]. Fienup's modification uses a new constraint on the object to fit with the requirement that the object must be compact. More specifically one sets a region in real space called the support where the object is known to fit within. Outside this support region the image is set to zero. This is not strictly true for an isolated object because it assumes a fully opaque background instead of fully transparent, but according to Babinet's principle the scattered diffraction patterns of the two cases are identical except for the undiffracted beam intensity at the very center (see for example Born and Wolf [3]). Fienup also required that the image be nonnegative, although he showed later that with a sufficiently strong support constraint even the phase information from complex-valued objects can be retrieved [31].

It was not until 1981 that Bates showed that the phase problem was "effectively" uniquely solvable in more than one dimension for localized images which are properly sampled [32]. An example of a non-uniqueness that remains is that an object with a centrosymmetric diffraction pattern is indistinguishable in reciprocal space from its conjugate reflection called its enantiomorph. The phase retrieval is also not unique with respect to shifts of the entire object in real space since these translations manifest as shifts in the phase of the diffracted wave. The phase problem is not uniquely solvable in 1D.

Since Fienup's reformulation of the Gerchberg-Saxton algorithm, other alternative iterative algorithms have been suggested and implemented [33–35]. These modifications attempt to increase the speed of recovering the phases as well as avoid local minima which can trap the algorithm. With noisy data an algorithm is considered to have reached convergence when its error metric (not globally defined for all algorithms) stagnates.

There are a few comparative studies of the different algorithms [18, 36, 37], but comprehensive yet meaningful comparisons are difficult because of the diverse application of these algorithms and varying definitions of the performance of an algorithm. However, based on these comparisons, we have decided to exclusively use the Difference Map algorithm [34] or its special case the Hybrid Input-Output [33] for the work described here. Both algorithms are summarized in Appendix B.

2.3 XDM experimental setup

The experimental apparatus that we currently use for all of our x-ray diffraction microscopy experiments was developed at Stony Brook [38] and is located at beamline 9.0.1 on a 0° bend at the Advanced Light Source (ALS) in Lawrence Berkeley National Laboratory (LBNL). As described briefly in

Sec. 2.2.3, the x-ray source is a U10 undulator with 43 magnetic periods of 10 cm, which is shared with the 9.0.2 beamline. A multilayer mirror bends the X-rays at a grazing angle of 2.25° down the 9.0.1 beampipe. When it is removed the X-rays travel into the 9.0.2 beampipe; therefore, although only one beamline can operate at a time, switching between the two is straightforward. A beryllium window separates the ultra-high vacuum of the undulator from the somewhat lower vacuum of the rest of the beamline. It also is efficient at filtering out energies below 400 eV. Further downstream, where downstream is in the positive direction of the x-ray propagation, an aluminum coated silicon nitride window removes any additional visible light which may have entered the beampipe.

The microscope is designed to irradiate an isolated specimen with coherent, plane wave illumination and collect the far-field diffraction pattern on a CCD detector. There are two critical components of the apparatus upstream of the specimen. The first is the monochromator zone plate segment and pinhole, which also defines the illumination. The second is the corner; a diamond-shaped aperture very close to the sample to block all but the center of the Airy pattern from the pinhole. Downstream of the specimen is a movable beamstop which allows low spatial frequency information to be collected while protecting the detector from the direct, unscattered x-ray beam. In the following section each of these components are explained in detail.

2.3.1 Monochromator system

Before illuminating the specimen the pink x-ray beam traveling from the multilayer mirror must be monochromatized. Beamline 9.0.1, has a monochromator system consisting of a small segment of a larger, mathematical Fresnel zone plate and pinhole positioned at the focal length of the particular wavelength desired. Although this system done not allow for much energy tunablity, it does provide a temporal coherence $\lambda/\Delta\lambda$ of at least 500 [39]. The small zone plate segment is taken from the top of a much larger theoretical zone plate. It functions similarly to a horizontal grading and focuses primarily in the vertical direction. Since zone plates are chromatic optics, each wavelength focuses to a distinct focal length (Eq. 1.19). An approximately 5 μm diameter pinhole is placed at the focus of the desired energy to both monochromatize and define the beam size and spatial coherence. Figure 2.2 shows a diagram of the pinhole blocking all but the desired energy focused by the zone plate segment. Typically the pinhole is place 25 mm upstream of the sample and either the zone plate segment is used 110 cm upstream of the pinhole for 750 eV or 80 cm upstream for 520 eV.

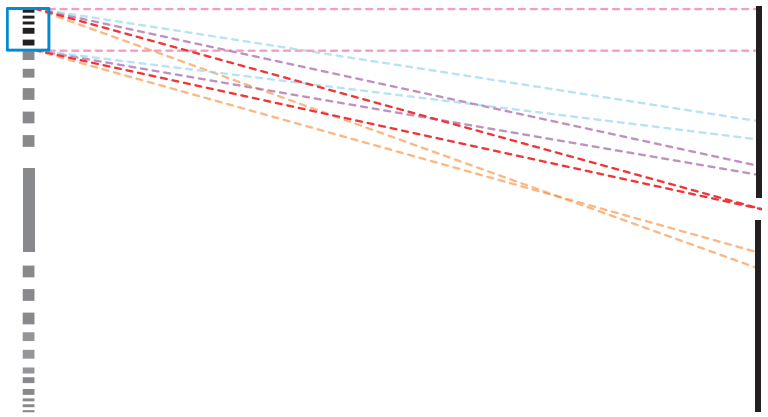

Figure 2.2: Diagram of the side view of monochromator zone plate and pinhole system. From a larger, mathematical zone plate, only a small segment (indicated by the blue box) is fabricated. This segment of a zone plate focuses the pink, incident x-ray beam primarily in the vertical. Since zone plates are chromatic optics, each wavelength focuses to a distinct focal length. A pinhole is placed at the focus of the desired energy to both monochromatize and define the beam size and spatial coherence.

2.3.2 Corner

Directly upstream of the sample is the corner. It is a square aperture rotated by 45° to form a diamond (Fig. 2.3). This aperture blocks most of the scattered photons from the pinhole from hitting the sample. An ideal pinhole will produce an Airy pattern in its far-field. In x-ray diffraction microscopy we wish to illuminate the specimen with a plane wave. The center illumination of an Airy pattern is a sufficient approximation of a plane wave; however, the higher order Airy rings must be blocked. When the corner is out and not blocking the pinhole scatter, a shadow of the EM grid that holds the specimen overpowers any coherent diffraction scattering from the specimen (Fig. 4.7). This shadow can be used to orient oneself on the EM grid and gain a quick overview of its quality.

2.3.3 Movable beamstop

Downstream of the sample and directly in front of a CCD detector, is a moveable beamstop. Its shape is diamond to match the aperture of the corner. Its size is also chosen to cover the entire undiffracted illumination from the corner so that when no specimen is in the x-ray beam, the only light hitting the

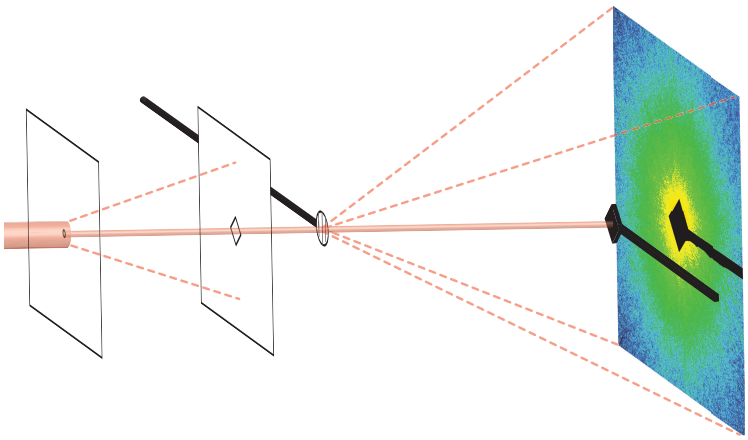

Figure 2.3: Diagram showing experimental setup (not to scale). From left to right are the following components: pinhole, corner, sample, moveable beamstop, and CCD. Upstream is to the left. The direct beam is the solid pink while the scattered signal is outlined as dashed lines.

detector is the slight scattering off the corner's sharp edges. The beamstop is required so the CCD is not damaged by the intense direct beam. A moveable beamstop allows a larger stop to be used and moved in concert with the corner to cover more or less of the direct beam using different exposure time lengths to record both the intense low spatial frequencies and the significantly dimmer high spatial frequency scatter (Fig. 2.4). By stitching together CCD images of different beamstop positions and exposure times, a single diffraction intensity pattern which spans approximately six orders of magnitude is attained.

In February 2010, we installed a second, semitransparent beamstop, which is now used in addition to the original to collect the direct beam and very central speckles. This semitransparent beamstop was constructed by depositing an approximately 100 nm layer of gold onto of a 1 mm by 1 mm silicon nitride window. This corresponds to an attenuation of the direct beam of over 90% for 520 eV and around 80% for 750 eV [5].

Hybrid pixel array detectors, such as the Pilatus [40], which among other features have very fast readout times and high dynamic range, are now becoming more readily available. Such single photon detectors would significantly reduce the required time for data acquisition with our microscope since the full dynamic range of the diffraction data could be taken without the need of a beamstop. Speed is especially important for sample which must be kept at cryogenic temperatures and for 3D data collection. However, currently such detectors are too large to fit inside our present vacuum chamber and they have

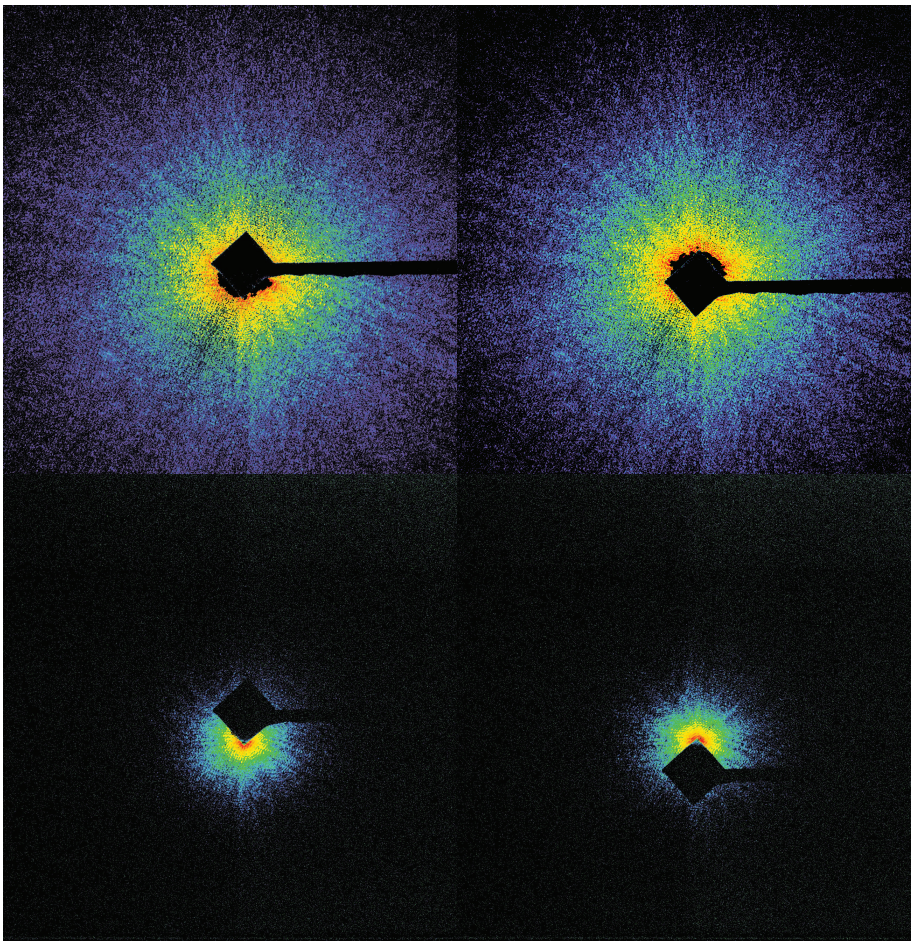

Figure 2.4: Four example beamstop positions which are used to collect a full six or more orders of magnitude of intensity information. The top two beamstop positions are more centered on the direct beam allowing longer exposure times to collect the high spatial frequency reaching to the edge of the CCD detector. The bottom two beamstop positions scarcely cover the most intense portion of the beam allowing only the very shortest exposure times to collect the low spatial frequency information.

oxide surface layers which make them inefficient for soft x-ray detection.

Chapter 3

XDM of freeze-dried surface labeled yeast

For high resolution imaging, x-ray microscopy provides unique capabilities for image entire eukaryotic cells. Confocal microscopy along with other high resolution visible light imaging techniques such as two-photon excitation [41] and stimulated emission depletion [42] continue to push resolution beyond the diffraction limit of visible light; however, fluorescent tagged molecules cannot be viewed in the context of the untagged bulk material of the specimen of the same beyond-diffraction-limit resolution. On the other end of the imaging spectrum, electron microscopes can achieve sub-nanometer resolution, but sample thickness and radiation damage typically limit biological samples imaging to far coarser resolutions. For frozen hydrated biological specimens a resolution of 10 nm requires a specimen thickness of no thicker than 450 nm for 120 kV electrons and only 100 nm thick specimens for 2 nm resolution [43]. Using the penetration power of X-rays we have imaged freeze-dried, whole, eukaryotic yeast cells approximately 2 μm thick to at least 13 nm resolution. We have investigated the distribution of the α–mannan sugar in the cell wall of the yeast with silver-enhanced immunogold labels and by employing the additional phase information gained by using XDM we have some limited ability to distinguish the depth of specific labels.

In this chapter we will describe an x-ray diffraction microscopy experiment on freeze-dried immunogold labeled *Saccharomyces cerevisiae* yeast with 750 eV X-rays [19]. Currently, it represents the highest resolution image of a whole eukaryotic cell and the highest resolution real-space x-ray image of any non-crystalline biological specimen. The chapter will detail the protocol for the gold labeling and silver enhancement along with freeze-drying process (Sec. 3.1). We will then discuss the data collection (Sec. 3.2), phase retrieval process (Sec. 3.3), and the validity of the final image by examining the phase

retrieval transfer function (Secs. 3.3.5 and 3.6) and by using correlative microscopy (Sec. 3.4). Finally we will describe two independent methods used to determine the resolution of the final XDM images (Sec. 3.5).

3.1 Labeling and drying protocols

Here we describe the materials and methods used to prepare the yeast before imaging. Cells were immunolabeled in solution, then cryogenically fixed and freeze-dried. We used the *whi5* mutant [44] of *Saccharomyces cerevisiae*, which produces smaller (3 – 4 μm diameter) yeast cells than the 6 – 7 μm diameter typical of the wild type. The advantages of this strain is that it has the complex structures found in all eukaryotic cells, but is small enough to satisfy the Born approximation (Sec. 2.2.1) for 750 eV energetic X-rays.

To label the α-mannan sugar found in the cell walls of both the wild type and *whi5* mutant of *Saccharomyces cerevisiae* [45], we used the mannose binding protein concanavalin A (conA; a lectin protein originating from the *Canavalia ensiformis* or jack bean plant). The protein was conjugated to both a 1.8 nm gold particle and a Texas Red fluorescent label and was custom made for this experiment by Nanoprobes Incorporated (Yaphank, NY). The advantages to this particular immunoprobe is that we were able to visualize the labeled cells with a standard fluorescence microscope (courtesy of Aaron Neiman's molecular biology laboratory at Stony Brook University) before a closer inspection with a scanning electron microscope (SEM) or x-ray microscope. Furthermore, it was found that gold particles on the order of 10 – 40 nm in diameter did not label uniformly and a significant portion of the yeast cells remained unlabeled. Therefore, we chose a label which we knew to be below our resolution and utilized a light-sensitive silver enhancer, also from Nanoprobes Incorporated (Yaphank, NY), to increase the size of the immunoprobes after labeling (Appendix C.1). In addition, a six carbon linker molecule was used to separate the conA protein from the gold label and further increase the likelihood that the conA would find the α-mannose sugar.

Figure 3.1 compares SEM images of chemically dried yeast with α-mannan sugar labeled using different immunogold label sizes. Panels (A) and (B) show 40 nm diameter gold labels conjugated with streptavidin (a protein from the bacterium *Streptomyces*). A second conjugate between conA and biotin (a B-complex vitamin), which binds specifically to the streptavidin, was used to attach the gold conjugate indirectly to the α–mannan sugar. Panel (A) demonstrates the result of first binding the biotin-conA conjugate to the sugar and then allowing the streptavidin-nanogold conjugate to attach to the biotin. Panel (B) shows the result of first binding together the two conjugates and

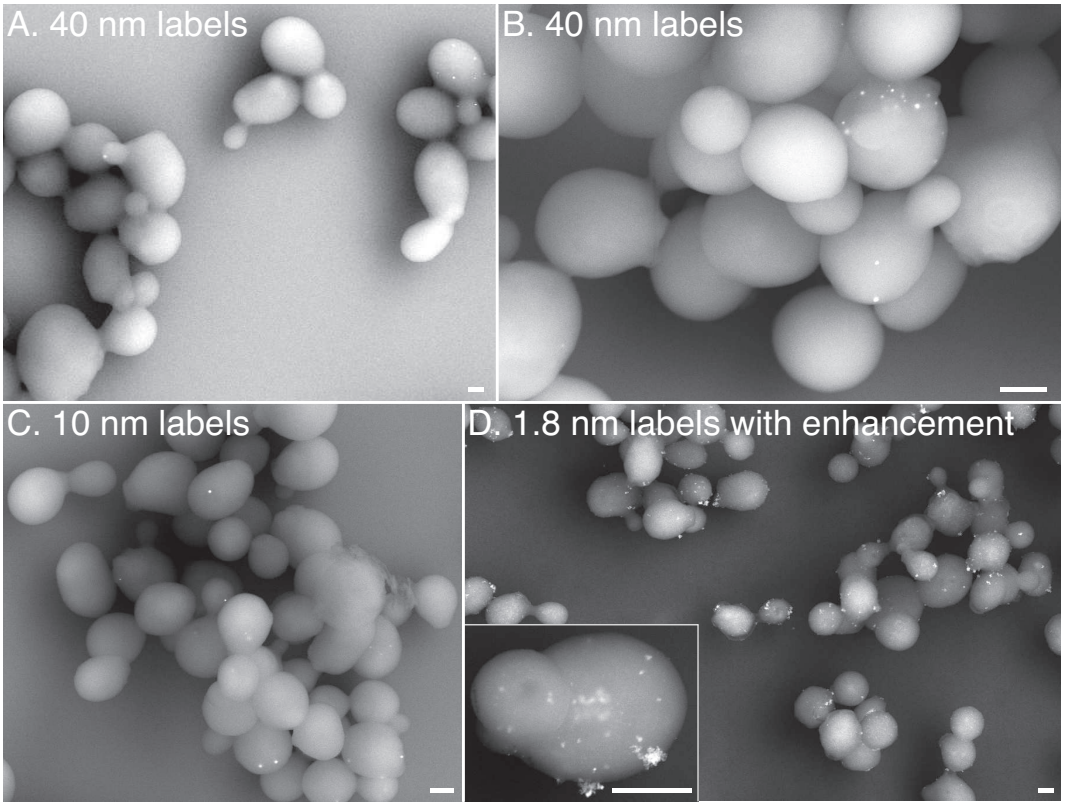

Figure 3.1: Scanning electron microscope images of chemically fixed and dried immunogold labeled *Saccharomyces cerevisiae* yeast showing vastly different labeling rates and distributions for gold labels in the 10 – 40 nm diameter range (A – C) compared to 1.8 nm diameter with silver enhancement (D). (A and B) are SEM micrograph of 40 nm diameter gold labels conjugated with streptavidin (a protein from the bacterium *Streptomyces*) which specifically binds to biotin (a B-complex vitamin) that is conjugated to the concanavalin (conA). The first is the result of binding the biotin-conA conjugate to the cell wall and then the streptavidin-gold label to the biotin. The latter was done by first binding the biotin-conA to the streptavidin-gold and then attaching the entire label to the cell wall. Both methods result in moderate labeling of a handful of cells, with the majority of cells remaining unlabeled. (C) is an SEM micrograph of 10 nm diameter gold labels conjugated with conA. The result is similar both (A) and (B). (D) is an SEM micrograph of 1.8 nm diameter gold labels conjugated to conA with an additional six carbon linker in between. The inset shows a close up on an individual budding yeast cell. The gold labels are silver-enhanced to enlarge them enough to be visible in the SEM. One can see that these smaller labels cover all of the cells and the silver-enhancement connects the small labels to form larger clusters. All scale bars are 1 μm.

then attaching the entire chain to the cell wall. Both methods were found to be equally poor at producing well distributed gold labels. (C) is an SEM micrograph which demonstrates the effectiveness of using 10 nm diameter gold labels conjugated directly with conA. Labels are more evenly distributed; however, there are still too few of them. (D) shows the labeling scheme that was eventually used in the x-ray diffraction microscopy experiment. Gold labels with 1.8 nm diameter conjugated with conA with an additional six carbon linker. Labels were then silver enhanced to increase their overall size.

In this study of gold labeling using the scanning electron microscope, it is found that the electron beam is initially unable to penetrate the cell wall deep enough to image most immunogold because the labels are often partially embedded into the biological material. However, with longer exposures and without a thin sputter coated gold layer, the electron beam burns off the top most layers and the labels appear.

After labeling and silver enhancement, the yeast cells were either chemically fixed and dried on silicon nitride wafer fragments for scanning electron microscopy imaging (Appendix C.2) or freeze-dried on formvar-coated, carbon stabilized electron microscopy grids for the high resolution x-ray diffraction microscopy imaging (Appendix C.3). Freeze-drying uses rapid plunge freezing into liquid ethane to fix the cells in vitreous ice. Pure water that is cooled at a rate of 10^6 K/s forms a glasslike amorphous ice state. This state of ice is ideal for preserving biological samples because ice crystals do not form thereby causing intracellular structural damage. Furthermore, the fixation by rapid freezing is fast compared to molecular diffusion time for a distance on the order of the microscopy resolution. This ensures that proteins do not denature before fixation. In contrast, the slow process of fixation by organics such as glutaraldehyde can take 30 minutes or longer. However, because both processes require the dehydration of specimens which are comprised mostly of water, dehydration artifacts are unavoidable [46].

3.2 Data collection

Following specimen labeling and freeze-drying, coherent x-ray diffraction data were recorded at 750 eV photon energy using the experimental apparatus (described in Sec. 2.3) located at beamline 9.0.1 of the Advanced Light Source (ALS) at Lawrence Berkeley Laboratory (LBNL). To collect a single coherent diffraction intensity data set on the freeze-dried yeast, a total of 34 diffraction patterns were collected at different beamstop positions and exposure times using a Roper Scientific (Trenton, NJ) MTE-2 CCD detector. The detector has 1340×1300 pixels of 20 μm size and was located 12.8 cm downstream from

the specimen. In addition, background diffraction patterns were collected from a clean region of the sample substrate to eliminate any scatter not originating from the specimen, such as X-rays scattering from the corner. Because the background diffraction data recorded for this specimen was contaminated with faint scattering from a nearby object, no subtraction of background files was used to create the final diffraction intensity pattern. The following section describes the data merging procedure of the different beamstop positions, the skin dose applied to the specimen at each tilt angle, and the preliminary analysis of the diffraction data.

3.2.1 Data merging

To combine the 34 data files per angle into one diffraction intensity pattern for each viewpoint, the automated merging program (`AMP`), newly developed by Jan Steinbrener in our group, was used. The program generates a beamstop mask, zeros the pixels blocked by the beamstop, quantifies the detector's dark current and subtracts it from both the background and data files, removes outlier pixels such as those from cosmic rays, subtracts background images from the data, and finally stitches together the images. `AMP` requires minimal user input and has been shown to result in higher quality diffraction intensity patterns than more hands-on approaches used previously [20, 47]. The final image obtained with `AMP` had a dynamic range of over six orders of magnitude and a 19×19 missing pixel region in the center due to the saturation limits of the detector.

3.2.2 Skin dose

Recall from Sec. 1.4.1 that dose is a measure of absorbed energy per mass and what is typically calculated is the skin dose, which is the energy absorbed in just the first layer of the material. The total x-ray exposure time per angle for this sample was 406.2 seconds with an estimated cumulative irradiance of $1.7{\times}10^9$ photons/μm^2. Assuming the freeze-dried yeast has an outer layer of pure $\rho = 1.35$ g/cm^3 dense protein, the total skin dose accumulated per angle was $1.2{\times}10^8$ Gray.

However, for freeze-dried yeast cells, we have found diffraction speckle motion during imaging which is consistent with cell shrinkage for radiation doses from 5×10^8 Gray to beyond 5×10^{10} Gray [48]. Figure 3.2 shows that the initial collapse is quite rapid, but slow shrinking continues for much longer. No such diffraction speckle motion is visible in frozen hydrated yeast at those doses. Shrinking is also seen in chemically fixed and dried yeast [18]. Typically dried specimens are irradiated until shrinking has slows to a negligible

rate before data is collected. This significantly increases the total required dose.

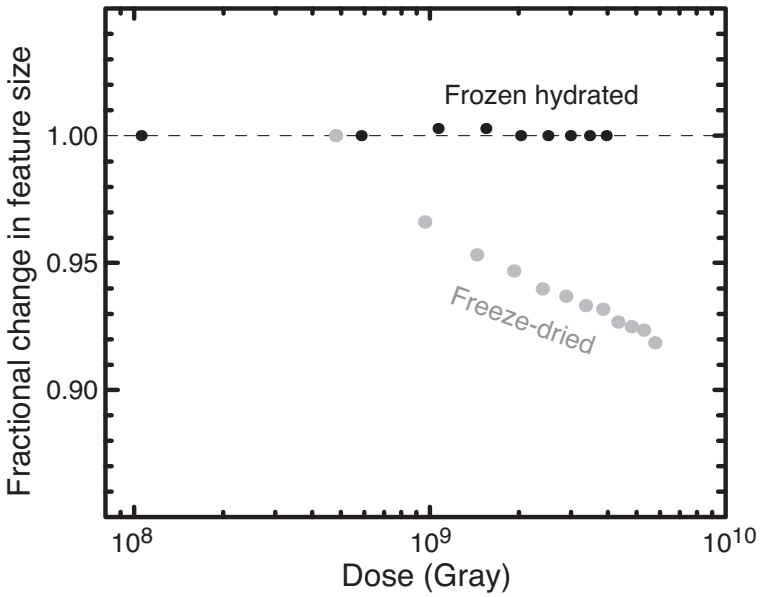

Figure 3.2: Fractional change in diffraction speckle as a consequence of radiation dose of freeze-dried yeast in contrast to the more stable frozen hydrated yeast [48]. Freeze-dried cells initially collapse significantly and then continue to shrink more slowly.

For this particular freeze-dried yeast the radiation dose applied directly prior to data collection amounted to around 2×10^9 Gray, which is appreciably higher than the dose required for imaging. Figure 3.3 demonstrates the damage from this initial exposure with autocorrelations of the yeast after different radiation dosage. The autocorrelation of a real space image is equivalent to the Fourier transform of the diffracted intensity

$$f * f = |F|^2, \tag{3.1}$$

where capitalization denotes the Fourier transform of the corresponding lower case function, a convention which will be used for the remaining of the chapter. The autocorrelation is a convenient estimate of the real space object when only the coherent diffraction intensities are known.

The actual shrinking in Fig. 3.3 is difficult to see as still images; see Supplementary Movie S1 for a video of the shrinking autocorrelation. What is clear

in these images is the drastic increase in boundary sharpness and subsequent degradation of that same boundary.

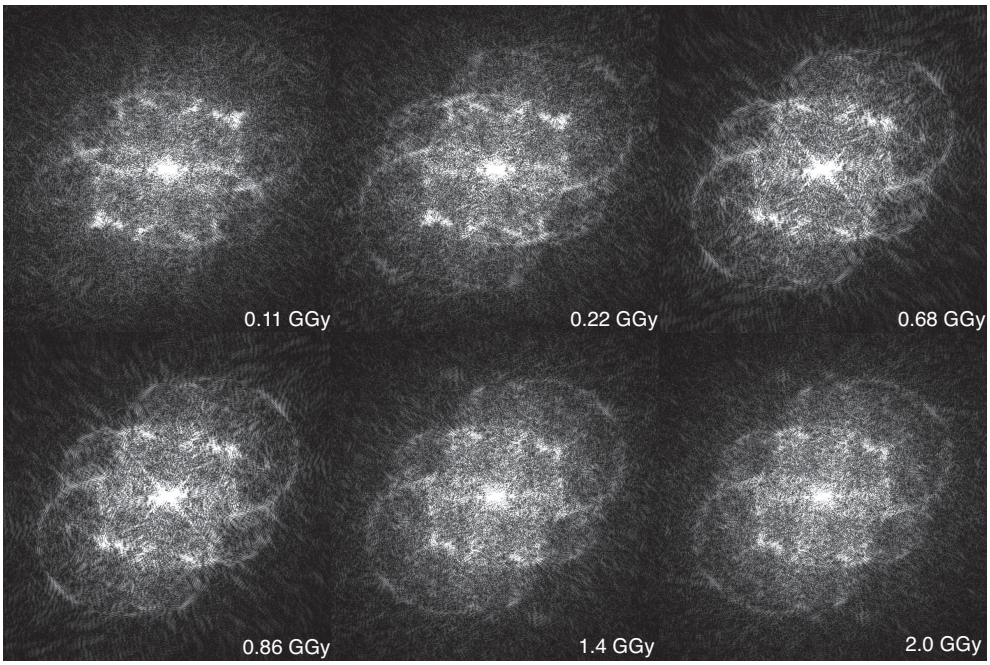

Figure 3.3: Demonstration of radiation damage by examining the autocorrelation functions of the freeze-dried yeast before data collection. In addition to simply shrinking, which is difficult to see when images are placed side-by-side, the radiation dose initially increases the sharpness of the autocorrelation boundary, until around 8.6×10^8 Gray. The boundary subsequently degrades again until shrinking has significantly slowed after 2×10^9 Gray

3.2.3 Centering and preliminary analysis

Before phase retrieval was performed on the `AMP`-assembled diffraction intensity array, the true center of the coherent diffraction pattern had to be determined. Due to the Fourier shift theorem, a shift in diffraction space translates to a phase shift in real space of

$$\mathcal{F}^{-1}\{G(f_x - a)\} = g(x)e^{\mathrm{i}2\pi ax}, \tag{3.2}$$

resulting in retrieved phases which have linear phase ramps with phase jumps after a 2π shift. Although such linear ramps in phase can be removed afterwards,

it is more straightforward to center the diffraction pattern initially and only remove small linear ramps which result from subpixel misalignment and avoid phase jumps.

Since the direct, unscattered beam was not measured because of detector saturation limits, the position of the diffraction center is not known precisely [28]. The location of the diffraction center is found by minimizing the ratio of the sum of the absolute value of the imaginary part of the autocorrelation of the image to the sum of the absolute value of the real part of the autocorrelation at different centers, namely

$$\min\left(\frac{\sum|\mathfrak{Im}\{f*f\}|}{\sum|\mathfrak{Re}\{f*f\}|}\right). \tag{3.3}$$

For the dried yeast diffraction pattern, the full 1300×1340 intensity array was centered and cropped square to a 1140×1140 array. To use the phase retrieval code written in `C` on a parallel processor machine the array was subsequently cropped to a subset with base two dimensions, namely 1024×1024. The result is the real space pixel size increased from 9.3 nm to 10.6 nm. The maximum spatial frequency of this cropped array is 67 μm^{-1} or 7.5 nm half-period at the corners. In Sec. 3.5 we discuss the results of applying the phase retrieval algorithm to the full 1140×1140 array and find that the resolution of the resulting wavefield is not improved despite the improvement in pixel size.

Figure 3.4 shows false color images of the magnitude of centered, cropped diffraction patterns for each of the five recorded specimen tilt angle. Coherent scattering information extends to the corners of most of the arrays, suggesting high resolution information not dominated by noise. A 500% zoomed-in view of the center of the 0° diffraction pattern shows large speckles with good contrast. This is indicative of a small, well isolated object in a sufficiently coherent incident beam. The missing low spatial frequency region in black covers approximately the area occupied by 7 speckles.

To get a clearer indication of the quality of diffraction data, we can plot the power spectral density for each angle (Fig. 3.5). The power spectral density (PSD) is defined as the average intensity per spatial frequency. By examining the five PSD plots it is immediately apparent that 30° is the poorest angle since the plot is dominated by noise at a significantly larger half-period (approximately 10 nm) than the other angles. Radiation damage may be a factor since this was the final angle recorded. Additionally, both $-30°$ and 30° fall off slightly steeper around 8 μm^{-1} (63 nm) than the other angles. This could be the result of the higher tilt angle since the x-rays must pass through more of the substrate and there is more incoherent background scattering from the

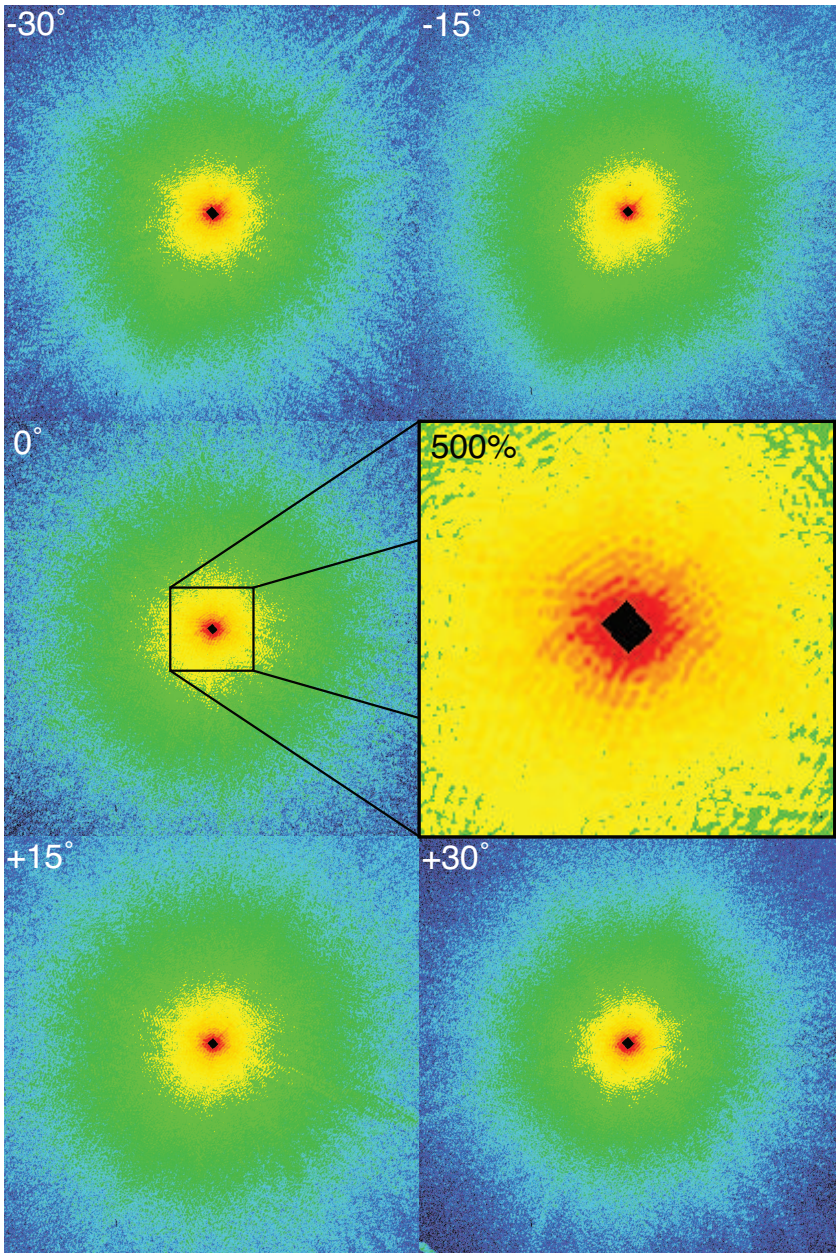

Figure 3.4: False color images of the diffraction magnitudes on a logarithmic scale from five angles: -30°, -15°, 0°, 15°, and 30°. A 500% zoomed-in view of the center speckles of the 0° diffraction pattern is also shown. The missing low spatial frequency region in black covers approximately the area occupied by 7 speckles. Each angle is a mosaic of raw data images stitched together using the program `AMP` written by Jan Steinbrener (Sec. 3.2.1). The arrays were centered then cropped to 1024 $\times$ 1024 with a maximum spatial frequency of 67 μm^{-1} (7.5 nm half-period) at the corners.

larger, elliptically-shaped beam footprint. It is also noteworthy that from the lowest spatial frequencies until around 10 μm^{-1} (50 nm), the power spectrum density for 30° and −15° remain lower than the other angles.

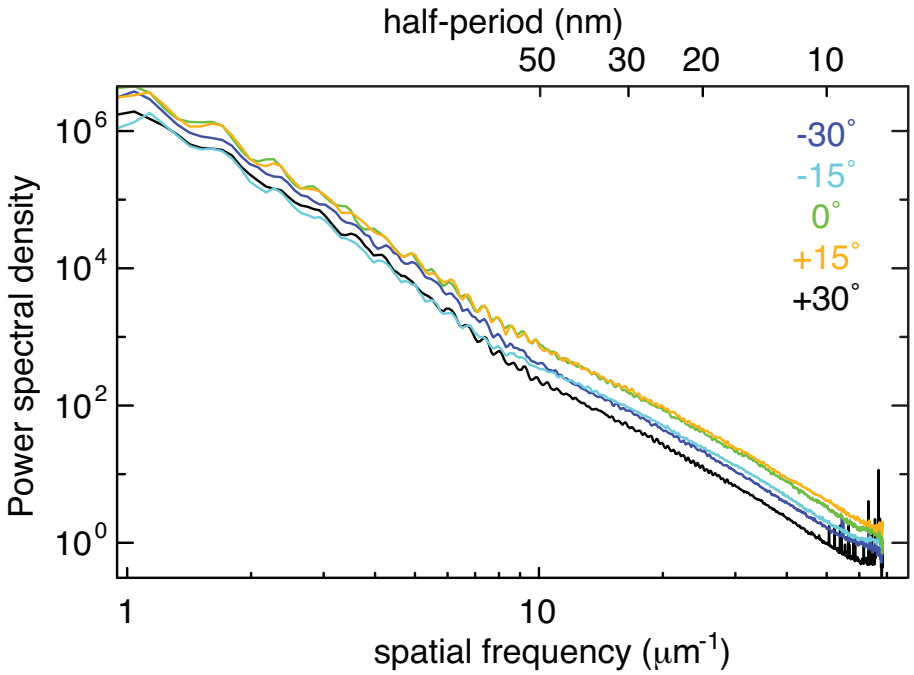

Figure 3.5: Power spectral densities (PSD) from five sample tilt angles: −30°, −15°, 0°, +15°, and +30°. It is immediately apparent that 30° is the poorest angle since the power spectral density is dominated by noise at a significantly larger half-period (approximately 10 nm) than the other angles. Additionally, both −30° and +30° fall off slightly steeper than the other angles. This may be the result of the higher tilt angle.

A final quick test of coherent diffraction data quality is the inspection of the Fourier transform of the intensity or the autocorrelation (Eq. 3.1). We have found that seeing a well-defined object boundary in the autocorrelation of an object is a strong indicator that the object can be successfully reconstructed. In the autocorrelations from all of the recorded tilt angles one can even see a clear double-walled boundary (Fig. 3.6). Ghost images (marked by red arrows), which are holographic images of the sample, are indicative of coherent scattering from a nearby point scatterer. The ghosts are only observable in the 0° autocorrelation (especially visible on the 300% zoomed in view), which was the first angle recorded, suggesting that radiation damage may have

caused them to disappear. In fact, at larger tilt angles the beam footprint is elongated making it more likely to coherently scatter off surrounding objects.

3.3 Complex wavefield reconstruction

This section provides an overview of the iterative phase retrieval algorithm used to recover the lost phases of the scattered wavefield from the freeze-dried yeast. It also details the averaging process and post-reconstruction high-pass filtering. Finally the results of the individually reconstructed diffraction intensity patterns from the five tilt angles are discussed.

3.3.1 Phase retrieval with finite support constraint

To recover the lost phase information for the freeze-dried yeast, the Difference Map algorithm (Appendix B.1) was used with a finite support constraint [34, 49]. This algorithms is a generalization of the Error Reduction algorithm by Gerchberg and Saxton [29] modified to search for a solution which satisfies both the measured diffraction intensities and the best guess of the object's support, which is the reconstruction array subspace within which the specimen is constrained to fit [30]. A full discussion of the support constraint can be found in Sec. 3.6.1, while a detailed outline of phase retrieval algorithms is in Sec. 2.2.4. Furthermore, I will compare the results of using the Hybrid Input-Output algorithm (Appendix B.2) compared to those using Difference Map and show that both algorithms produces very similar phase information in Sec. 3.6.2.

An initial approximation of the object's support was obtained from the Fourier transform of the diffraction intensity pattern. That support guess was subsequently tightened using a combination of the `Shrinkwrap` algorithm [50] and manual adjustment. A detailed discussion of the validity of a specific support constraint guess is discussed in Sec. 3.6.1. For all of the iterative reconstructions performed on the freeze-dried yeast, a nonnegativity constraint was applied to the imaginary part of the complex array. This nonnegativity constraint effectively limits the maximum phase shift through the specimen to π. This corresponds to a total projected thickness limit of less than 1.5 μm of solid dry protein [5]. The dried yeast in this experiment fall easily within this protein thickness limit.

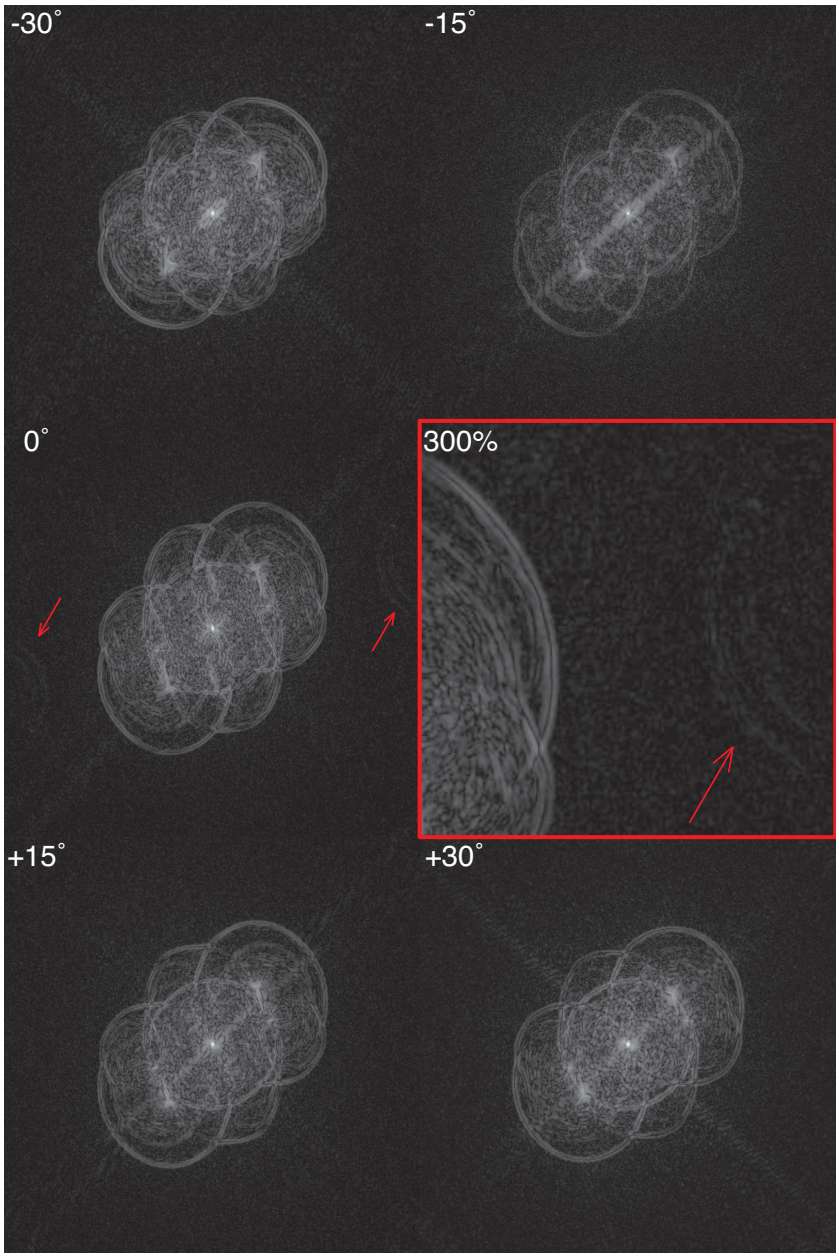

Figure 3.6: Logarithmic-intensity-scale autocorrelations of a yeast cell specimen from five different viewing angles. All angles show well defined double-walled boundaries, which we have found to be a strong indicator of yeast diffraction data that can be successfully reconstructed. Ghost images (marked by red arrows) are indicative of coherent scattering from a nearby point scatterer. The ghosts are only visible in the 0° autocorrelation (especially in the 300% zoomed in view), which was the first angle recorded, suggesting that radiation damage may have caused them to disappear.

3.3.2 Averaging

For each tilt angle a total of ten independent iteration runs was performed using the same object support. Each of the ten runs began with a random initial phase start and ran for 2,000 iterations. At this point, another 8,000 iterations were performed where the complex Fourier projection from every 100^{th} iteration was averaged. This averaging between independent random phase starts [51] and within each start [49] reinforces consistent phases while averaging out fluctuations.

Before results can be averaged, the arbitrary multiplicative phase constant of each Fourier projection must be adjusted to a common value so that variations in this constant do not artificially suppress consistent phases. For this reconstruction the multiplicative phase constants were adjusted using the method suggested by Chapman *et al.* [22]. This method sets the phase of the zeroth Fourier projection, $P_F = \psi^{(0)}(k)$ with the phase constant $e^{\mathrm{i}\phi_0}$, to the phase which maximizes the real part of the image. This is equivalent to finding the phase ϕ_0 which maximizes the square of the real part of the image,

$$\sum_k \Big[\Re\big\{\psi^{(0)}(k)e^{\mathrm{i}\phi_0}\big\}\Big]^2 = \sum_k \Big\{\frac{1}{2}|\psi^{(0)}(k)|^2 + \frac{1}{4}\big[\psi^{(0)}(k)\big]^2 e^{2\mathrm{i}\phi_0} + \frac{1}{4}\big[\psi^{*(0)}(k)\big]^2 e^{-2\mathrm{i}\phi_0}\Big\}; \tag{3.4}$$

with pixel indexes k and complex valued $\psi(k)$. To maximize the square, we can simply maximize either of the last two terms. In other words, find the phase ϕ of $\psi^{(0)}(k)$ and set $\phi_0 = -\phi/2$ so the phase terms multiply to unity. Subsequent Fourier projections $\psi^{(j)}(k)$ are adjusted by the phase constant ϕ_j to minimize the phase difference between the current Fourier projection and the zeroth. The phase difference is simply the phase of the complex value

$$\sum_k \big\{\psi^{(0)}(k)^*\big\}\psi^{(j)}(k). \tag{3.5}$$

In addition to the phase constant adjustments, linear phase ramps were removed from Fourier projections, since these phases can arise from sub-pixel shifts of the true diffraction pattern center with the applied magnitudes (Sec. 3.2.3). This is done in a very basic fashion by fitting the phase column-by-column and row-by-row to a linear function then subtracting the mean phase ramp.

3.3.3 High-pass filtering

After the Fourier projections are averaged, a high-pass filtered is used to reduce the signal from the unconstrained low spatial frequencies corresponding

to the center missing pixels region. The high-pass filter has the form

$$f(q) = \begin{cases} d + (1-d)\frac{q}{\sigma}^4 e^{2-\frac{2q^2}{\sigma^2}} & \text{if } q < \sigma \\ 1 & \text{else,} \end{cases} \tag{3.6}$$

where $d = 0.3$ and $\sigma = 102.4$ or a tenth the size of the array.

Although it is important to reduce the unknown low spatial frequency signal to reduce spurious data, we must be careful to understand the implications of its use. Lacking the low spatial frequency information creates an artificial edge enhancement to the final wavefield image. Figure 3.7 demonstrates the effects of the high-pass filter function on a transmission x-ray microscope (TXM) image of frozen hydrated yeast taken using 525 eV energetic X-rays at beamline U41 at *Berlin Elektronen-speicherring-Gesellschaft für Synchrotronstralung II* (BESSY II) in Berlin, Germany. On the left is the original image (A), which shows a chain of yeast cells surrounded by damage substrate. Part (B) of the figure shows the same image with the high-pass filter function applied using the same procedure as applied to the reconstructed diffraction images in this chapter. The filtered image appears sharper, although the information is actually reduced and the high frequency noise is enhanced. Image (C) has had spatial frequencies corresponding to the size of the missing central pixels in our x-ray diffraction measurements have been zeroed and then the same high-pass filter applied. This image shows a reduction in contrast, but not as much edge-enhancement artifacts as the central image. Note that neither the center nor right image is identical to what happens to the reconstructed XDM wavefield since its center missing pixels are allowed to float instead of either knowing (B) or zeroing (C) them.

3.3.4 Results

Using the method described above (Sec. 3.3), the unknown phases of all five specimen tilt angles ($-30°$, $-15°$, $0°$, $+15°$, and $+30°$) were retrieved with varying success (Fig. 3.8). Since the final image is a complex array, we have displayed the magnitude as brightness and the phase with hue. Although some of the angles reconstructed worse than other, namely $-15°$ and $+30°$ which are plagued by their enantiomorphs, many of the same features can be seen in all images, most notably the two large vacuoles (V). Furthermore, the general shape, namely of a budded yeast, rotates around itself from angle to angle as expected .

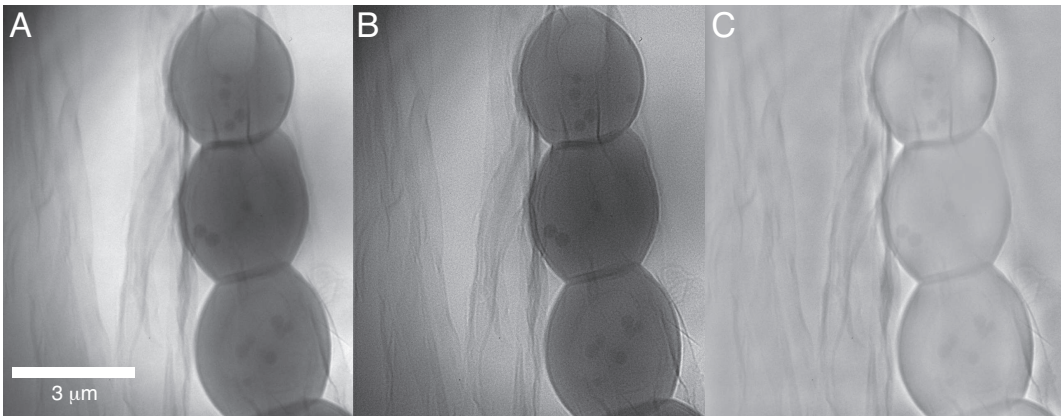

Figure 3.7: Demonstration of the effects of the high-pass filter function on a transmission x-ray microscope (TXM) image of frozen hydrated yeast taken using 525 eV energetic X-rays at beamline U41 at BESSY II in Berlin, Germany. The original image (A) shows a chain of yeast cells on damaged formvar substrate. A high-pass filtered version of this image (B) using the same procedure as applied to the reconstructed diffraction images in this chapter appears sharper, though of course its information content has been reduced and background noise appears to be enhanced. In the image at right (C), spatial frequencies corresponding to the size of the missing central pixels in our x-ray diffraction measurements have been zeroed, and the image has been high-pass filtered using the same procedure as in (B).

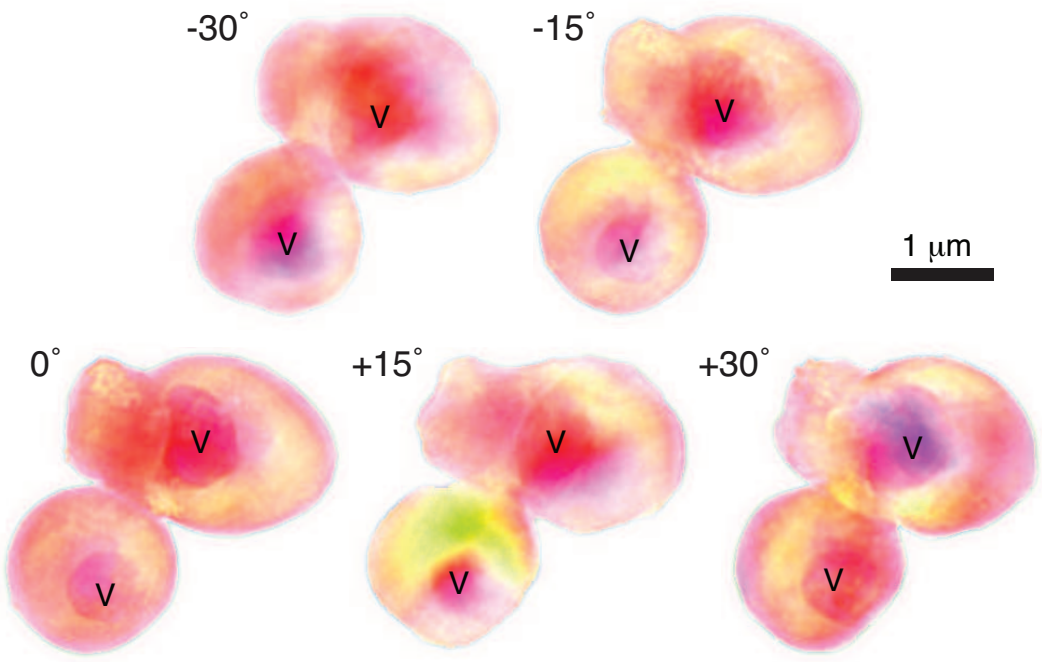

Figure 3.8: Reconstructed wavefields of freeze-dried yeast of tilt angles −30°, −15°, 0°, +15°, and +30°. The largest, most easily identifiable feature is the large vacuole (V) in each cell. The overall shape of the yeast rotates around itself as expected when the tilt angle changes. Enantiomorphs are visible at both −15° and +30°. Magnitude is shown as brightness and phase with hue.

3.3.5 Phase retrieval transfer function

The phase retrieval transfer function (PRTF) [22], which is the square root of the intensity ratio [49, 52], is typically used to plot the reliability of the reconstructed phases as a function of spatial frequency. This function is somewhat similar to the modulation transfer function (MTF) for an optical system which shows the loss of information as a function of spatial frequency. The PRTF is defined as the spatial-frequency-dependent ratio of the magnitudes of the averaged reconstructed wavefield divided by the experimentally recorded diffraction magnitudes, or

$$\text{PRTF} = \sum_k \frac{\left|[\psi(k)e^{\mathrm{i}\phi(k)}]_{\text{avg}}\right|}{\sqrt{I_{\text{measured}}}}. \tag{3.7}$$

Since the averaging of estimates within a single phase retrieval with one random phase start and between multiple random phase starts leads to reproducible Fourier amplitudes being reinforced while non-reproducible amplitudes approach an average of zero, the spatial frequency at which this metric decays sharply tells about the length scale at which reliable phasing declines. The PRTF curve is often used to quantify a resolution for a reconstructed complex wavefield although there is, as of yet, no standard cutoff frequency used by the x-ray diffraction community. Furthermore, sufficient averaging must be performed or the PRTF will be misleadingly high for all frequencies. Figure 3.9 is a plot of PRTF curves of the 0° freeze-dried yeast reconstruction. As the number of iterations which are averaged is increase the PRTF curve drops. Sufficient averaging is such that further increasing the number of iterates averaged does not change the curve.

Comparing the plot of PRTF curves for each of the freeze-dried yeast reconstructed angles, we come to the same conclusion we deducted by simple inspection of the reconstructed wavefields, specifically that −15° (cyan) and +30° (black) recreate the least reliable phase information (Fig. 3.10). The first drops quickly to 40% and remains there until rolling off around a half-period of 15.6 nm (spatial frequency of 32 μm^{-1}). The latter fairs a little better dropping to only about 50%; however, also rolls off around the same half-period, but drops more rapidly.

What is most surprising is how poor the −15° phases are transfered seeing that by studying the power spectral densities we concluded that +30° was the poorest diffraction intensity data because it was dominated by noise at a much lower spatial frequency in comparison to the rest (Fig. 3.5). The effect of this low signal to noise at high frequency manifests in the sharper drop in the PRTF of the +30° compared the other four angles. The inferiority of both

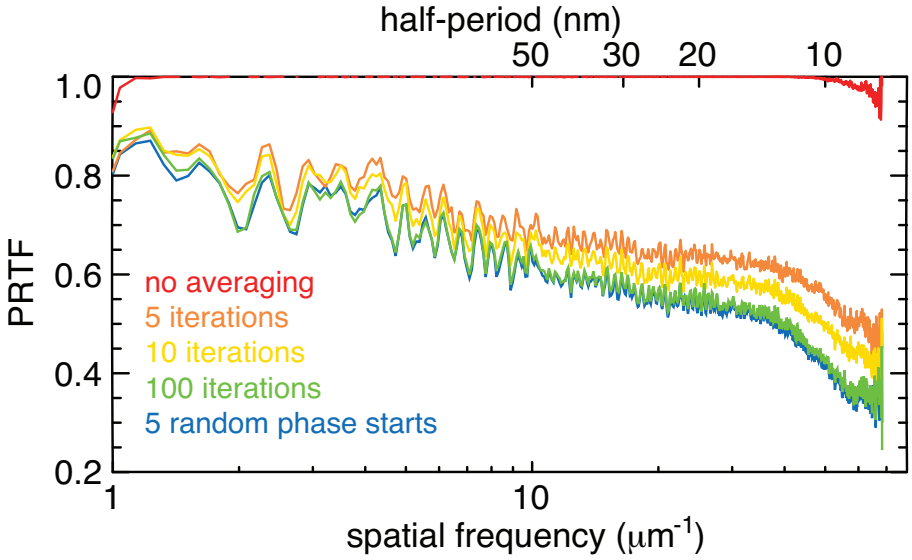

Figure 3.9: Plot demonstrating the effect of averaging on the PRTF. To get an accurate PRTF sufficient averaging must be performed or the curve with be misleadingly high. Averaging is sufficient when additional averaging no longer changes the PRTF curve. There is no change in the PRTF between averaging five (blue) or ten (not shown) random phase starts if each random start has 100 of the final 8,000 iterations averaged.

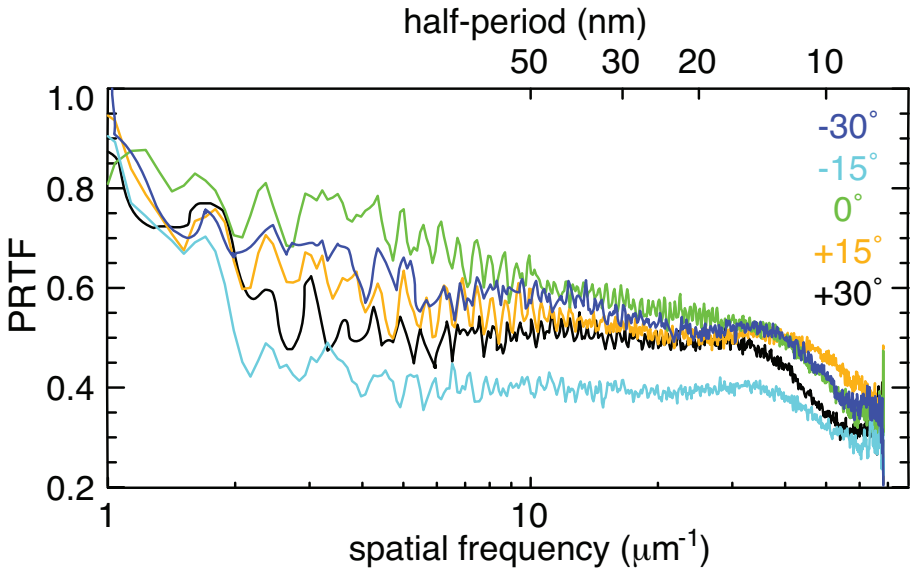

Figure 3.10: Phase retrieval transfer function (PRTF) of the budding dried yeast from five specimen tilt angles: $-30°$, $-15°$, $0°$, $+15°$, and $+30°$. Although the $+30°$ had the least promising power spectral density, the poorest phase reconstruction is of $-15°$. Nonetheless, the $+30°$ PRTF curve rolls off more rapidly than any other angle which can be attributed to the considerably noisier high spatial frequency data visible in the power spectrum density (Fig. 3.5). At low spatial frequencies $0°$ has the most reliable phases, while at high spatial frequencies $+15°$ is more dependable.

reconstructed phases is most notable in the visible enantiomorphs. What is not clear is whether the quality of the recorded diffraction intensities or the support guess is the underlying cause of the enantiomorphs. Figure 3.5 indicates that both intensity patterns had the worst quality low spatial frequency information; however, the power spectrum density for the $-15°$ angle significantly improves after 10 μm^{-1} (50 nm). Instead perhaps this is an indication that the reconstructed phases for $-15°$ could be improved by further tweaking of the support guess.

At low spatial frequencies 0° has the most reliable phases, but falls off similarly to $-30°$. At high spatial frequencies $+15°$ is significantly more dependable. The angle's PRTF curve does not fall below 50% until after 12.5 nm half-period (or 40 μm^{-1} spatial frequency) and continues to stay above 40% well beyond the spatial frequency cut off by the detectors edges, 47 μm^{-1}. These two views (0° and $+15°$) can be viewed in stereo when placed next to each other (Fig. 3.11), which gives a sense of three-dimensionality. To view, either keep your eyes parallel and look through the page as if staring at something at a distance or cross your eyes as through you are looking at something at half the distance to the page. In both cases, a third image should materialize in between the two images. It is this middle image which will appear three-dimensional.

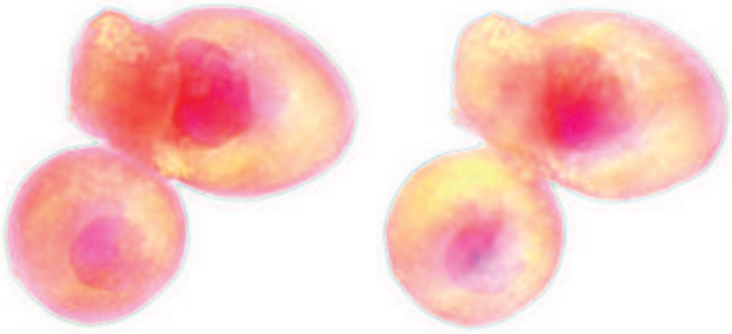

Figure 3.11: Stereo pair of the dried yeast using the 0° and $+15°$ angles. When viewed in stereo a sense of three-dimensionality is possible.

3.4 Correlative microscopy

In this section the reconstructed 0° angle wavefield is used to compare scanning electron microscope (SEM) and scanning transmission x-ray microscopy

(STXM) micrographs taken of the same sample after the reconstructions were performed. Both of these correlative microscopy techniques were performed after the phases of the coherent diffraction data were retrieved and were not used to as *a priori* information except to better estimate the sample to CCD detector distance which was incorrectly measured in the XDM setup.

Correlative microscopy provides strong confirmation of the fidelity of the XDM images and allows for greater confidence in identifying surface labeling and subcellular components such as the nucleus and vacuole. Using a STXM with 520 eV X-rays at beamline 11.0.2 at the Advanced Light Source (ALS) we are able to compare the internal structure from our higher resolution, complex image with a straightforward transmission image (Sec. 3.4.1). The STXM uses a Fresnel zone plate with 25 nm outermost zone width, Δr, which gives a theoretical Rayleigh resolution of 30.5 nm. Recall that the diffraction-limited resolution Δ_t of a Fresnel zone plate is given by $\Delta_t = 1.22\Delta_{r_N}$ (Eq. 1.17).

To compare the surface labeling of the XDM results, images were taken with a Zeiss LEO 1550 Schottky field emission gun (SFEG) scanning electron microscope (Sec. 3.4.2). Although the electrons cannot penetrate very deep into the cells, SEM images give great detail when viewing the surface of specimens.

3.4.1 Scanning transmission microscopy comparison

For correlative microscopy purposes, we imaged the yeast sample after reconstruction with a scanning transmission x-ray microscope using a $\Delta_{r_N} = 25$ nm zone plate. Figure 3.12 compares the intensity of the reconstructed 0° XDM wavefield (left) with the STXM image (right). Nonetheless, it is immediately apparent that the background in the XDM image is inverted in comparison with the STXM. This discrepancy is not surprising for two reasons. First we are not comparing equivalent depictions of the yeast cells. Furthermore, during the reconstruction of phases we have assumed zero intensity outside the support constraint instead of the full signal.

To clarify, let us write the XDM wavefield of the yeast as

$$\psi \sim \psi_0 e^{-kz\beta + \mathrm{i}kz\delta - \mathrm{i}kz}, \tag{3.8}$$

where ψ_0 is the complex incident wave with both a magnitude and phase term, k is the wave number, β and δ are the space-dependent integrated absorption and phase shift from the object, and z is the distance through the material. In the area outside the object, there is no absorption or phase shift and the

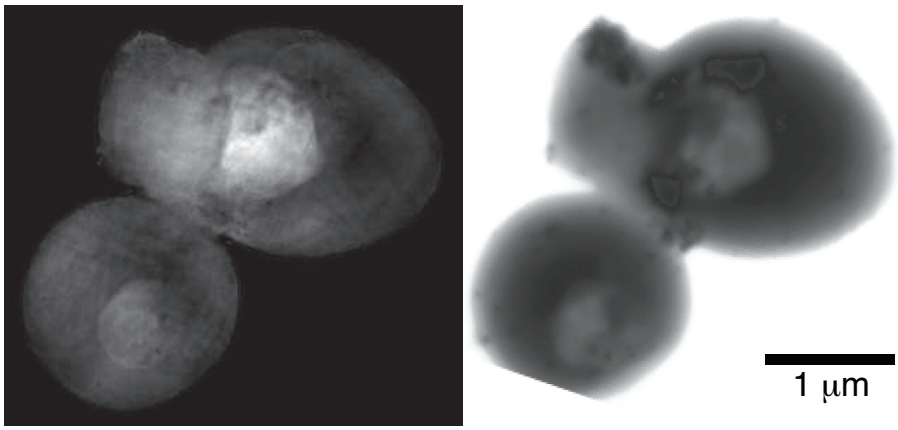

Figure 3.12: Comparison of the intensity of the original reconstructed wavefield (left) with a scanning transmission x-ray microscope (STXM) image (right) of the same specimen. It is clear when compared to the STXM image (right) that the background of the XDM wavefield (left) is inverted. Note that early termination the STXM scan caused the apparent sharp boundary on the lower left of the cell.

exit wave becomes a complex constant which we will write as

$$\psi = \psi_0. \tag{3.9}$$

However, this is not what is imposed by the reconstruction algorithm which sets the magnitude and phase outside the object's support guess to zero. As a result, what is reconstructed is not ψ, but $(\psi - \psi_0)$ instead. The support constraint is still consistent with the diffraction pattern according to Babinet's principle [3] since the center frequency ($q = 0$) is not measured.

Using the same notation, the STXM absorption image is simply the intensity of the wave,

$$|\psi|^2 \sim \psi_0^2 e^{-2k\beta z}, \tag{3.10}$$

while the intensity or absolute value squared of the reconstruction is

$$|\psi - \psi_0|^2 \sim \psi_0^2 |e^{-k\beta z + \mathrm{i}kz\delta - \mathrm{i}kz} - 1|^2 \tag{3.11}$$

Needless to say, the absolute value of the reconstructed image (Fig. 3.12b) will not be equal to the STXM absorption image (Fig. 3.12b). The reconstruction has a phase factor, $e^{\mathrm{i}kz[\delta-1]}$, and is translated by the constant ψ_0 relative to magnitude of the STXM absorption information. Therefore, before

comparing the absolute square of the reconstruction to the STXM image, one must multiply by the correct phase factor and add the proper constant.

Unfortunately, neither of these constants are known. However, we know that the constant magnitude and phase factor should be such that the magnitude and phase outside the support guess are at full signal and zero phase. In other words, in the HSV or Hue, Saturation, and Value representation of the complex wavefield (see e.g. Fig. 3.11) the background should be bright red.

One can also think of the situation in terms of scatter plots on the complex plane. The STXM intensity image is contained entirely on the positive real axis. The scatter plot of the exit wave from an isolated, complex object under plane wave illumination is a distribution which originates at the positive, real value for the full illumination signal and spirals towards the origin (Eq. 3.8) [49]. As an example, Fig. 3.13 is a plot on the complex plane of $e^{-k\beta t+\mathrm{i}k\delta t}$, for a solid protein sphere [5] of radius 0.75 μm in black and 1.5 μm in gray with a wave number k corresponding to 520 eV. As expected, the scatter plot for each sphere starts at full signal and spirals towards the origin with the thicker sphere's plot spiraling further. The wavefield from freeze-dried yeast should follow a similar curve with more variation in thickness and material. Because cells are not as dense as solid protein, such a cell should not spiral into the negative imaginary quadrant. Recall from Sec. 3.3.1 that the phase retrieval algorithm uses nonnegativity of the imaginary part of the wavefield as *a priori* information.

Figure 3.14 shows the scatter plot from the reconstructed wavefield of the freeze-dried yeast pair. The first panel (A) gives the scatter plot of the unfiltered wavefield of the yeast. This plot begins at the origin and spirals into the positive, real quadrant. The second plot (B) is the scatter plot of the high-pass filtered wavefield. This second plot is quite similar except that the filtering condenses the information into a smaller complex region and a plume forms at the start of the spiral (indicated by an arrow).

To start the scatterplot at the full illumination signal and spiral toward the origin, the absolute value of the minimum of the real part of the wavefield was added and then a multiplicative phase term was chosen such that the real part is entirely contained between zero and the start of the scatter plot. The last two panels of Fig. 3.14 show the shifted and rotated wavefield without filtering (C) and with the high-pass filtering (D). Similar to the unshifted, unrotated scatter plots, the high-pass filtering consolidates the information into a smaller complex plane and produces a plume.

The result from shifting and rotating the scatterplot on the absolute value squared complex images is shown in Fig. 3.15. The image on the right is the unfiltered wavefield and on the left is the filtered. The plume on the filtered

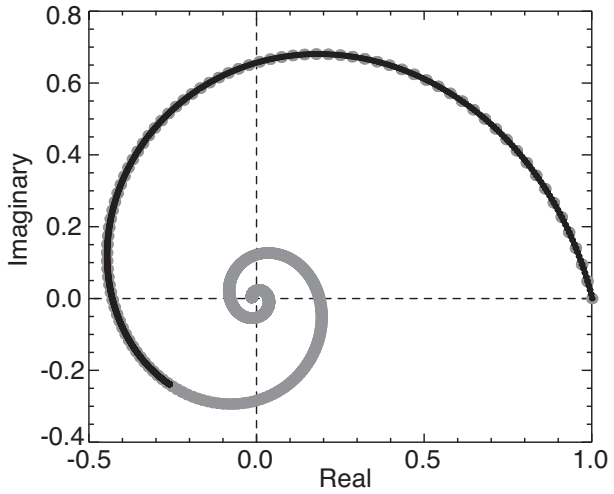

Figure 3.13: Scatter plot in the complex plane of $e^{-k\beta t+ik\delta t}$ for pure protein spheres of radius 0.75 μm (black) and 1.5 μm where the thickness of a sphere is $t = 2r\sin\theta$ and with a wave number k corresponding to 520 eV. Both plots begin at the positive, full signal and spiral toward the origin. The scatter plot of the smaller sphere follows that of the larger, but does not spiral as far.

scatter plot (3.14 d.) produces a bright ring surrounding the specimen which is very striking in the shifted wavefield image (Fig. 3.15) in comparison to the unshifted XDM image (Fig. 3.12).

Comparing the final shifted, high-pass filtered complex XDM micrograph (where brightness is magnitude and phase is hue) to the STXM image (Fig. 3.16) shows the improved resolution and added information from reconstructing the unknown phases. With the complex scatter plot shifted, we can identify specific organelle in the cell pair. The two vacuoles (V) are very large, low density structures which are visible in both XDM and STXM images. The nucleus (N) of the smaller cell is similar in density to the surrounding material, but can be identified by its boundary. A mitochondrion (M), which is smaller than the nucleus, can be recognized where it overlaps with the lower vacuole. The very dark granular material in both micrographs is the gold labels. These labels will be discussed in more detail in Sec. 3.4.2. Additional subcellular structures in the XDM image are visible, but can not be identified with confidence. Without a three-dimmensional image, organelles are difficult to uniquely distinguish because of overlapping information.

Beyond identifying a few of the cellular organelles we can also determine the reproductive phase of the cells. *Saccharomyces cerevisiae* yeast are often

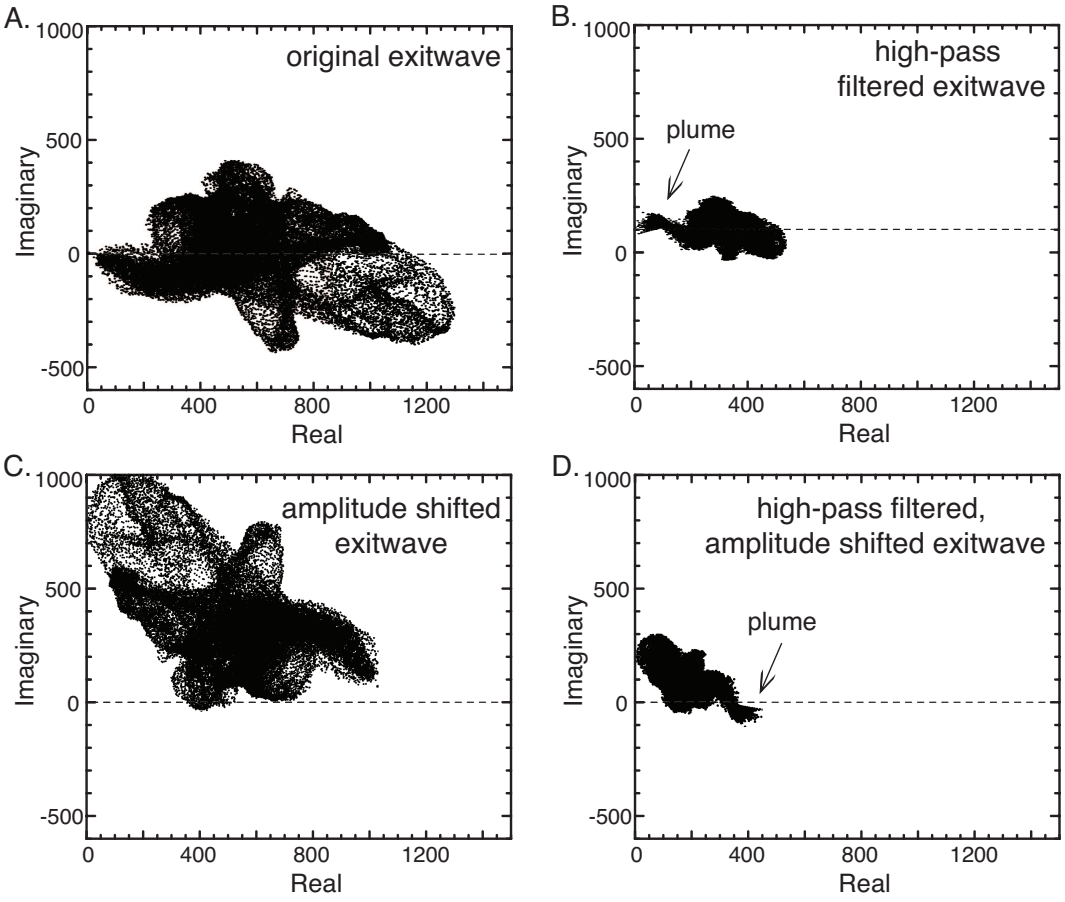

Figure 3.14: Comparison of the scatter plots of the reconstructed 0° wavefield with (B) and without (A) a Gaussian high-pass filter to the amplitude shifted wavefield with (D) and without (C) the high-pass filtering. The expected scatter plot of the wavefield from an isolated, complex object under plane wave illumination is a distribution that originates at the positive, real value for the full signal of the illumination and spirals towards the origin. The scatter plot of the unshifted exitwave (A) begins at the origin and spirals outward. The shift in amplitude and rotation of phase results in a scatter plot (C) which begins at the maximum real value and spirals inward. Both the unshifted spiral distribution (B) and the shifted distribution (D) show the effects of high-pass filtering on a scatter plot. The information is condensed into a smaller complex region and a plume forms at the start of the spiral (indicated by arrows). The plume in (D) causes the bright ring surrounding the specimen in Fig. 3.15 (right).

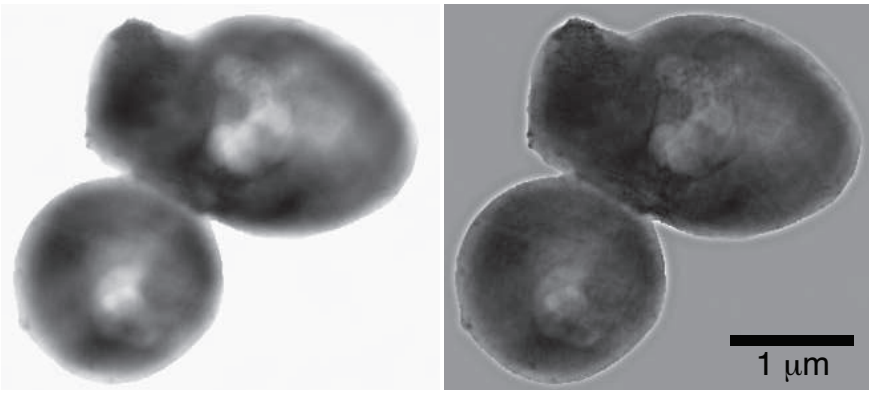

Figure 3.15: XDM intensity images after shifting and rotating the wavefield in the complex plane. On the right is the square of the absolute value of the wavefield after a constant amplitude was added and the global phase was shifted such that the wavefield from outside the specimen's support is at full signal and has no phase shift. The image appears blurred because the Gaussian high-pass filter was not applied. On the left shows the result of applying the filter. A bright ring surrounds the specimen and the background is no longer white, which is the manifestation of the plume visible in Fig. 3.14 (D).

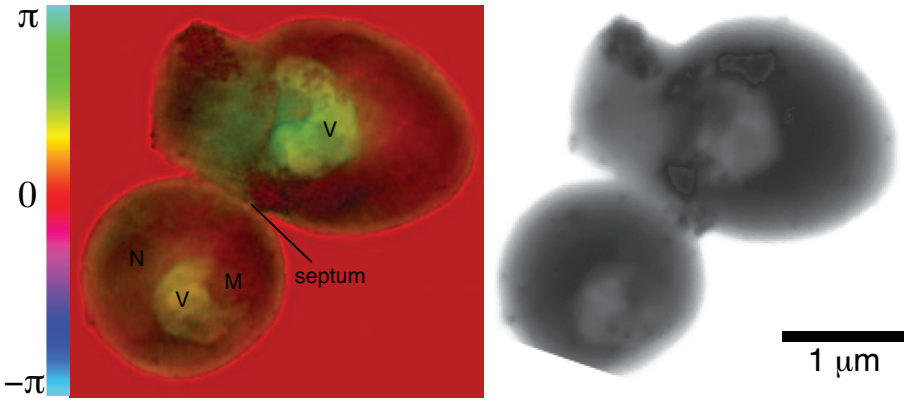

Figure 3.16: Comparing the STXM micrograph (right) with the complex, final XDM wavefield (left) shows clearly the benefits of the resolution improvement and the added phase information of XDM. A few organelles can be identified in the XDM micrograph; namely vacuoles (V), a nucleus (N), a mitochondrion (M), and a distinctly completed septum. The dark, granular material is the immunolabeling.

called budding yeast because of their cell division. Instead of one large cell dividing into two equal smaller cells, this species of yeast forms a small bud which grows as an attached daughter cell until the division is completed and the mother and daughter separate. Assuming they are a bud pair and not two independent cells in close proximity, a number of clues suggest they are post-mitotic (G_0 phase). In other words, they are two distinct cells having completely a reproductive cycle. The first indicator is that the septum, the wall which divides the mother and daughter cell (marked in Fig. 3.16), is complete and the cytoplasms are separated. Secondly, the nucleus in the daughter cell is distinct from that in the mother cell. Finally the relative size of the cells to each other is consistent with a mother and daughter cell, which have already finished dividing.

The unusually shaped area on the top left of the cell pair is what we believe to be an artifact from the dehydration process. We postulate that it is either a scar from a previous bud or the start of a new bud, which deformed as the cells shrank during dehydration. The overall size of the cells is significantly smaller than what is expected, indicating that the cells shrank significantly due to dehydration and irradiation. Typical yeast of the *whi5* strain are $3-4$ μm in diameter.

3.4.2 Scanning electron microscope comparison

Scanning electron microscopes (SEM) provide high contrast images of metals on the exterior surfaces by collecting the backscattered electrons; therefore we chose to use an SEM for correlative microscopy of the immunogold labeling of the α-mannan sugar of the cell wall. We imaged both the "front" (Fig. 3.17 C) and "back" sides (Fig. 3.18 C) of the yeast pair with a Zeiss LEO 1550 SFEG SEM by manually flip and remounting the specimen. Because the electrons first traveled through the support film, the "back" side image is slightly blurred.

The depth of focus (DOF) of this XDM experiment is approximately 130 nm, which does not contain the entire thickness of the yeast and reduces the contrast of a 2D image. Because no lens is used to focus light onto a particular plane, one reconstructs the complex wavefield at the particular focal plane correlating to where the object boundaries best agree with the support. For a spherical object, such as a yeast cell, this corresponds to the mid-plane [49, 53]. Furthermore, since one reconstructs a complex wavefield this focal plane can be shifted forward or backward within the object by convolution with a Fresnel propagation kernel. Appendix D gives an overview of Fresnel propagation.

Fresnel propagation was applied to the 0° reconstruction wavefield of the cell pair to bring into focus silver-enhanced gold labels on the front and back

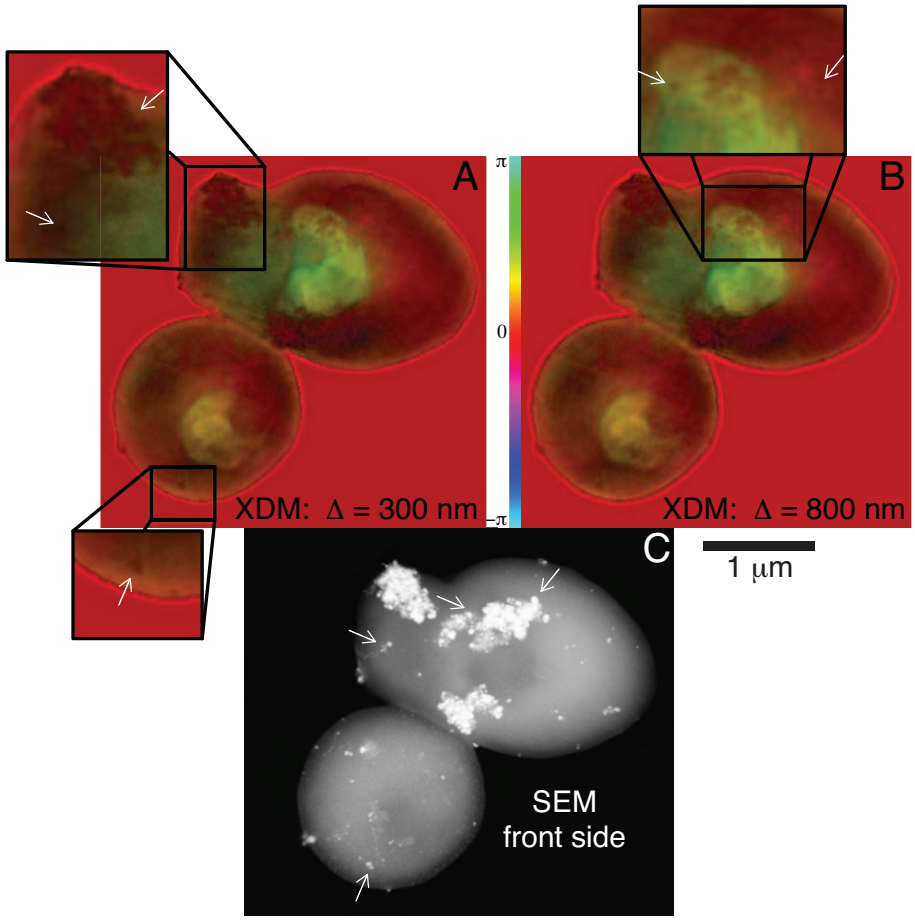

Figure 3.17: Correlation of surface immunolabels (indicated with arrows) between x-ray diffraction microscopy (XDM; A, B) and scanning electron microscopy (SEM; C) image. For XDM, the reconstructed complex wave is represented using brightness for magnitude and hue for phase. Two different focal planes are shown (obtained by Fresnel propagation from the plane of the tight support boundary [49]). Labels on the front surface of the yeast are on two focal planes; one at 300 nm from the reconstructed focal plane (A) and the second at 800 nm (B). Arrows indicate specific labels which are in focus on one of the XDM images and visible on the SEM image. Labels on the thicker regions of the yeast correspond to the focal plane further from the center. Different tilts produce the apparent distortion between the two images. Boxed areas of interest are shown at 2× magnification.

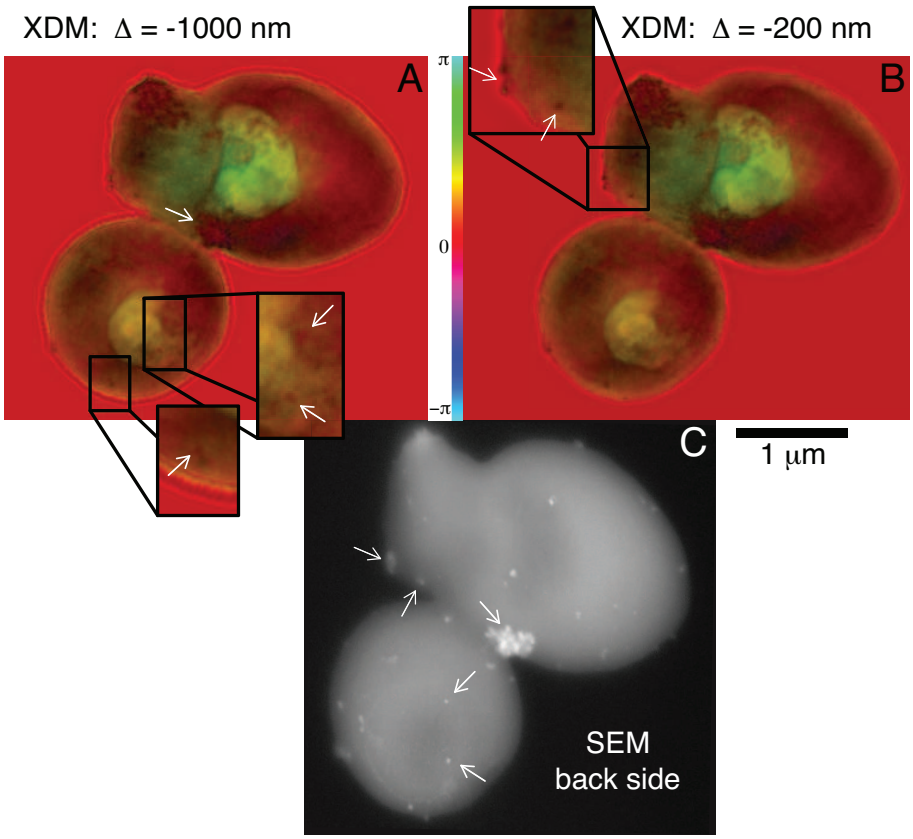

Figure 3.18: Correlation of surface immunolabels (indicated with arrows) between x-ray diffraction microscopy (XDM; A, B) and scanning electron microscopy (SEM; C) image. For XDM, the reconstructed complex wave is represented using brightness for magnitude and hue for phase. Two different focal planes are shown (obtained by Fresnel propagation from the plane of the tight support boundary [49]). Labels on the back surface of the yeast are on two focal planes; one at -1000nm from the reconstructed focal plane (A) and the second at -200 nm (B). The specimen was manually flipped to obtain the back SEM view, which was inverted for easier comparison. Arrows indicate specific labels which are in focus on one of the XDM images and visible on the SEM image. Labels on the thicker regions of the yeast correspond to the focal plane further from the center. Different tilts produce the apparent distortion between the two images. Boxed areas of interest are shown at $2\times$ magnification.

surfaces of the yeast. In Figs. 3.17 and 3.18, the top panels (A, B) show the reconstructed wavefield propagated to a total of four different focal planes: $\Delta = 300$ nm, 800 nm (Fig. 3.17) and $\Delta = -200$ nm, -1000 nm (Fig. 3.18). Arrows indicate specific labels which are in focus on one of the XDM images and visible on the particular SEM image. As expected, labels on the thicker regions of the yeast correspond to the focal plane further from the center. In addition, label positions correlate well with the "front" and "back" side of the yeast as seen in the SEM images despite the geometrical distortion created by different sample tilts in the SEM, and by the difference in appearance of larger features in the SEM image versus in the XDM reconstruction, where the contrast of larger XDM features is compromised due to the missing data obscured by the detector beamstop. For a video of the full propagation see the Supplementary Movie S2.

3.5 Resolution

Here we describe two independent measures of resolution which concur on a resolution range of 11 –13 nm. This is the highest x-ray microscopy image of a eukaryotic cell to date. While resolutions of $12-15$ nm have been shown using test samples [10, 11], lens-based x-ray imaging of cells is currently limited to the $30-60$ nm range. Table E.1 in Appendix E outlines the published pixel/voxel sizes and resolutions of lensless imaging on biological samples.

Section 3.3.5 uses the phase retrieval transfer function (PRTF) to estimate the reliability of the recovered phases of each of the five tilt angles. Although there is currently no standardized cut-off frequency, the curve is generally used to estimate the resolution of the reconstructed wavefield. Recently we have shown that Wiener filtering the PRTF is a more reliable means of determining the resolution of reconstructions from noisy data [20, 47]. The Wiener filter $W(f)$ is defined as

$$W(f) = \frac{|S(f)|^2}{|S(f)|^2 + |N(f)|^2}, \tag{3.12}$$

where the signal, $S(f)$, is estimated by determining the slope of the log-log plot of the power spectral density of the reconstruction and the noise, $N(f)$, is estimated as a spatial frequency independent noise floor. Figure 3.19 shows the Wiener filtered phase retrieval transfer function (wPRTF) curves from the three most reliable angles from Fig. 3.10; 15°, 0°, and −30°. Using 0.5 as a cutoff, the resolution can be estimated to be in the 13 to 11 nm half-period range for all three angles.

To confirm whether the resolution for this specific sample is limited by the spatial extent of the diffraction intensities or the phase retrieval algorithm,

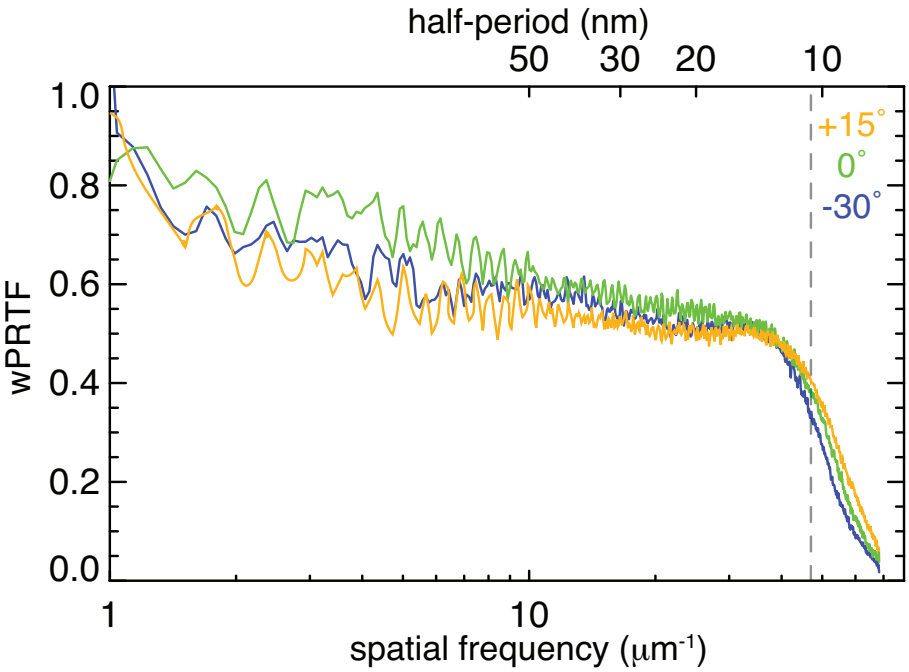

Figure 3.19: Wiener filtered phase retrieval transfer function of the three most reliable sample tilt angles. The gray dashed line shows the 10.6 nm real space pixel size. All three of these curves fall below 50% between the 13 – 11 nm half-period range. We estimate the resolution to fall in this range.

the larger intensity array consisting of 1140 × 1140 pixels was reconstructed. This increase in array size corresponds to a decrease in the real space pixel size from 10.6 nm to 9.26 nm. Figure 3.20 compares the wPRTF curves using identical phase retrieval procedures with the two intensity array sizes. Since the curves follow the same decline and have the same half-period at the 0.5 cutoff, the resolution limit appears to be not limited by the extent of the diffracted intensities collected, but instead the lack of significant data at higher frequencies. The noise dominated highest frequencies are suppressed by the Wiener filtering.

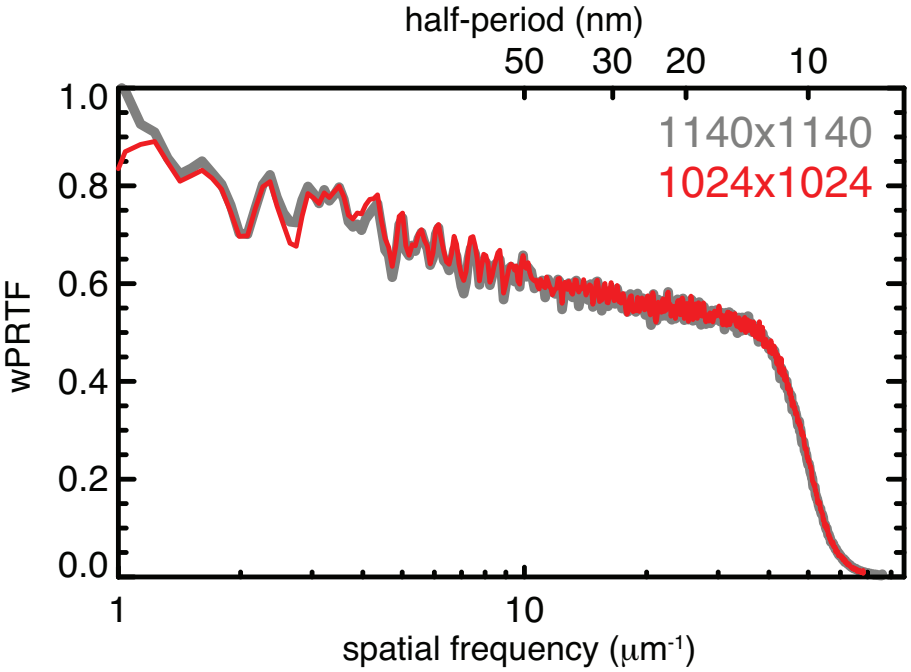

Figure 3.20: wPRTF curves from reconstructing the entire 1140 × 1140 array (gray) vs. the 1024 × 1024 subset (red) of the 0° tilt angle. The full array gives a pixel size of 9.26 nm while the subset has slightly larger pixels of 10.6 nm. Both curves follow the same decline suggesting that the lack of significant data at higher frequencies and not the extent of the diffracted intensities dictated the final resolution for this sample.

Since there is no standard cut-off frequency and the shape of PRTF curves tend to be fairly specimen dependent (although this is improved by the Wiener filtering), an independent measure of resolution would be favorable. For this particular sample we can make use of the 1.8 nm gold labels which were

silver-enhanced. Although these labels cannot be considered point scatterers because of the enhancement process, their high contrast can be exploited to estimate the spatial resolution of the reconstructed image.

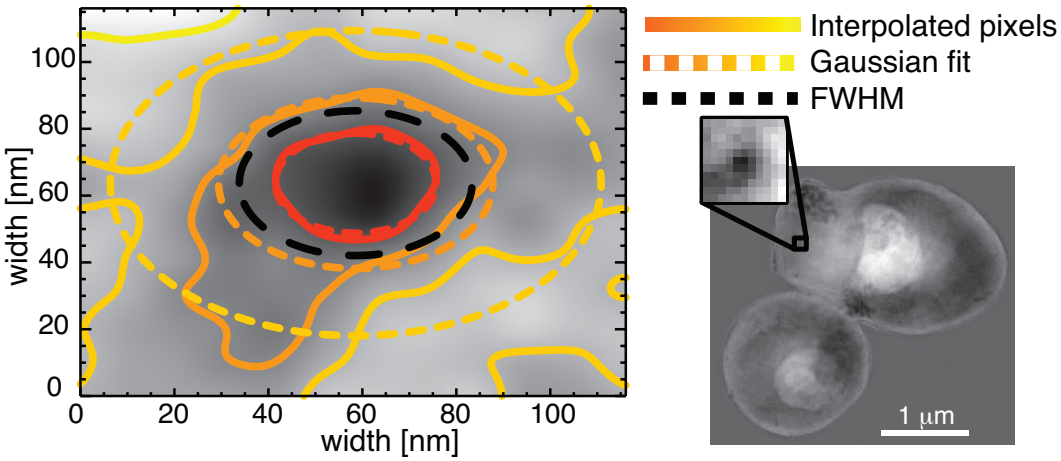

Figure 3.21: Estimation of image resolution based on a view of an isolated silver-enhanced gold label. The magnitude of the XDM wavefield of Fig. 3.16 is shown at right. A subfield of this image centered on the label of interest was extracted as indicated by the box, and cubic interpolation was then used to expand the image from an original pixel size of 10.6 nm to a pixel size of 0.53 nm. This expanded subfield is shown at left, along with solid isomagnitude contour lines (yellower hues indicate contours of higher magnitudes). It was then fit to a 2D Gaussian, with the result of a full width at half maximum (FWHM) major diameter of 51.2 nm (horizontal in this view) and 44.8 nm minor diameter.

Using the 0° reconstructed wavefield, a well isolated label was chosen and the region of interest was smoothed using cubic interpolation to reduce the pixel size from 10.6 nm to 0.53 nm. Figure 3.21 shows the location of the specific label with the region enlarged with its original pixel size retained (right). A contour plot with solid lines of isomagnitude (left) is overlaid on the smoothed region of interest. A yellower hue indicates larger magnitude. The interpolated representation was then fit to a two dimensional Gaussian function to avoid a possible directional bias in the resolution estimation if a single line profile through the object was chosen. The resulting fit is shown as dashed contour lines with the same coloring scheme. It has a full width at half maximum (FWHM) minor diameter of 44.8 nm and a major diameter of

51.2 nm.

Because the immunolabel is not a true point scatterer, its image is a convolution of the label's thickness and the point spread function of the imaging system. Using the SEM image (Fig. 3.17), the radius of the label was estimated to be 31.9 nm ± 2.5 nm (Fig. 3.22, red), where the error in the estimate is due to the finite size of the pixels. In Fig. 3.22 we have convolved the thickness function of a sphere of this radius with Gaussian point spread functions of varying widths to demonstrate that a point spread function of 15 nm FWHM fits very well when compared to the XDM signal shown in black and inverted such that the absorbing feature is a peak in place of a valley, while 25 nm FWHM is too large and 5 nm FWHM is too small. This suggests the XDM wavefield has a resolution in the range of 10 to 20 nm, which agrees well with the previous estimate of 11 to 13 nm.

3.6 Discussion

Here the validity of the support constraint is examined as well as the effects of an incorrect support on the phase retrieval transfer function. The relative success of the Difference Map and Hybrid Input-Output algorithms are then compared using the 0° angle data.

3.6.1 Validity of support constraint

An appreciable unknown in x-ray diffraction microscopy is the support guess, which is typically used as the real-space constraint on both the phase and magnitude of the current estimate. Normally an initial support constraint is assumed to be the shape of the autocorrelation of the real-space object which is easily obtained by taking the Fourier transform of the intensity array (Eq. 3.1), but reduced to approximately half the size. One can also simply use a square array either half the size of the entire array or large enough such that half the size of autocorrelation fits entire within. In some situations, a holographic ghost of the object is fully visible in the autocorrelation due to a small point-like scatterer near the object (Fig. 3.23). In these special cases, one can use the outline of the hologram as an excellent initial support guess.

Whatever the initial support guess, reconstruction of the lost phases proceeds while updating the support constraint as the object's true boundary becomes more apparent. The updates can be done by manually redefining the support guess or automatically by the `Shrinkwrap` algorithm [50], which redefines a new support by first smoothing then thresholding the current real-space estimate. While manual adjustments have shown to outperform on biological

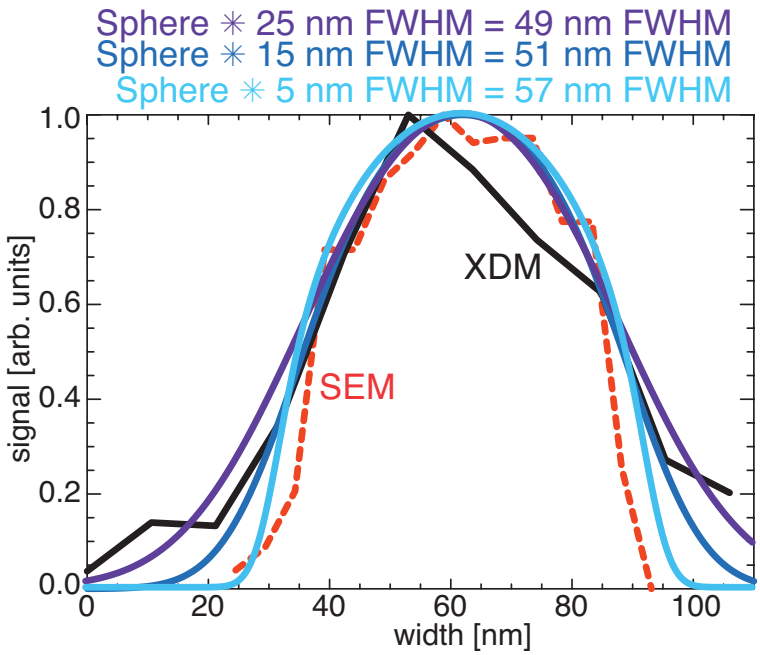

Figure 3.22: Approximation of point spread function of the XDM image by estimating the size of a single silver-enhanced gold label from the SEM image. The solid black line shows the XDM magnitude across the smallest width of label, inverted such that the highly absorbing label is a peak in place of a valley. The pixel size is 10.6 nm. The dashed line shows the same width in the SEM image with a pixel size of 4.9 nm. The radius of the label was estimated from the SEM image to be approximately 32 nm. The solid colored lines show three convolutions of the thickness function of a sphere with radius 32 nm and a Gaussian point spread function (PSF) with either 5 nm, 15 nm, and 25 nm full width at half maximum (FWHM). Although the large pixel size in the XDM image makes it difficult to determine within a few nanometer the PSF which produces the best fitting convolution to the XDM magnitude, the 15 nm PSF is clearly a better estimate for the XDM resolution than 5 nm or 25 nm.

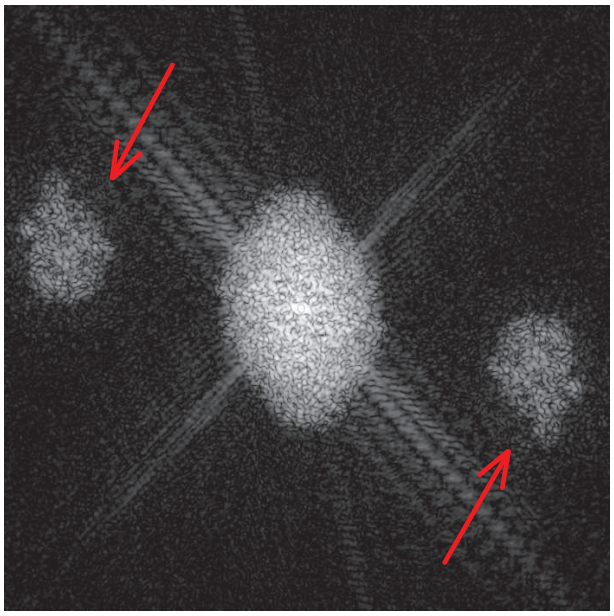

Figure 3.23: Autocorrelation of a different freeze-dried yeast with holographic ghost images indicated with red arrows. Such ghosts, which are enantiomorphs of one another, are a perfect initial support guess for phase reconstructions. This particular specimen was not reconstructed because it appears to have collapsed during the freeze-drying process.

specimens where sharp boundaries are not as common as in manufactured samples, manual adjustments do not lend themselves to quick, user friendly phase retrieval. Nonetheless, the ideal smoothing and thresholding parameters for `Shrinkwrap` can be extremely sample dependent and some care must be taken so that the updated support does not shrink to be smaller than the object, or increase in size well beyond the object. Furthermore, `Shrinkwrap` can become trapped in a support guess that contains both the object and its enantiomorph (or mirror image), which are both equally valid solutions to the phase problem with centrosymmetric data. On the other hand, `Shrinkwrap` can find areas outside the original support guess that also contribute to the recorded scattering intensities. In a typical search for the most accurate support guess for soft, biological specimens, a combination of both techniques is used.

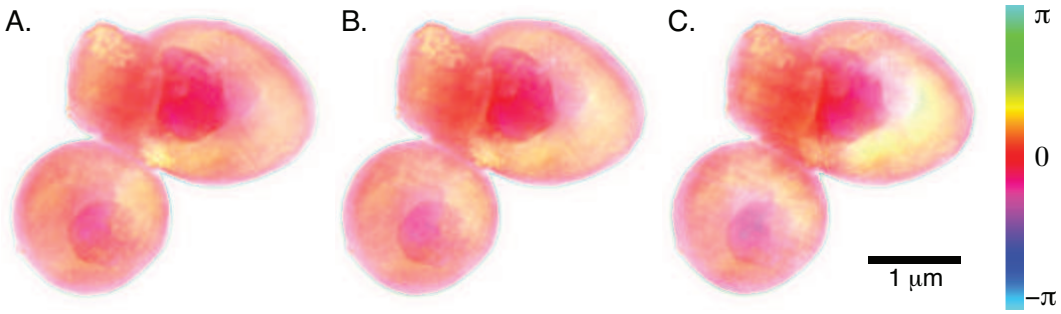

Figure 3.24: Three complex exitwaves for three slightly different supports. The original support used to reconstruct (B) was found using a combination of `Shrinkwrap` and manual adjustments. The support for (A) is 0.09 μm^2 larger than the original support area of 5.82 μm^2 while (C) has a 0.09 μm^2 smaller support. The modified supports were created by rebinning the original 1024×1024 support array to either 1032×1032 or 1016×1016 and either cropping or adding zeros such that the modified array returned back to 1024×1024, thus not modifying the overall shape.

When performing final tweaks on the support constraint either manually or with `Shrinkwrap`, the wPRTF can be used to reveal which support guess reconstructs the phases most reliably. Even with small changes in the support size, the wPRTF can change drastically. Figure 3.24 shows three reconstructed wavefields for three slightly different support guesses. The reconstruction conditions described in Sec. 3.3 were used for all three supports. The three supports share the same overall shape and differ in size by less than 0.2 μm^2

between the largest (A) and smallest (B). By visual inspection it is difficult to say which phase rendering is the most true. However, by plotting the wPRTF curves of each reconstruction (Fig. 3.25), one immediately sees which support most accurately reconstructs the unknown phases.

The wPRTF curves in Fig. 3.25 indicate that both the original support (black) and the one that is 0.09 μm^2 smaller (red) produce reliable phases for spatial frequencies up to the edge of the CCD detector (47 μm^{-1}). The former is slightly higher at low to mid-range spatial frequencies, while the latter is best at the high frequencies. On the other hand, the 0.09 μm^2 larger support (blue) is very consistent at low spatial frequencies, but drops below 50% much earlier than the other two curves. This poorer performance at high resolution could be from a blurring of fine features because the reconstructed object can shift around slightly inside the enlarged support. If images were aligned before averaging this blurring could be reduced. However, because the reconstructions are dominated by their sharp-edged support constraints, attempts at automatic alignment using the images cross-correlation functions have only produced sub-pixel shifts, too small to reduce the resolution. Although with the smaller support constraint one can claim better resolution, the original support was chosen for the final reconstruction because it performs well over the whole range of spatial frequencies.

In addition to small changes in the overall tightness of the support guess, we also want to ensure that sections of the support are not missing or are extraneous. The `Shrinkwrap` algorithm can be beneficial in either adding or subtracting sections to the support guess. Areas of significant magnitude outside the support are included in the updated guess, while areas inside the support with little magnitude are removed. One might think that a support which does not include sections of the object would produce lower quality reconstructions because the support estimate disagrees with the recorded diffraction intensities, while a support with an addition beyond the shape of the object will only require more iterations because less information is known.

To manually test the response of the phase retrieval algorithm to missing or extraneous areas of the support estimate, we performed phase retrieval on the 0° tilt angle of the freeze-dried yeast using the original support estimate with either a section added or removed. Figure 3.26 shows the resulting reconstructed wavefields with either an excess area added (left) or a necessary area removed (right). The identical reconstruction protocol as used in Fig. 3.24 was used. The phase retrieval algorithm performs well when a region of the support is increased beyond the outline of the object. In fact, the added support area (indicated with an arrow) is free of extraneous reconstructed image contrast. On the other hand, if the support guess does not include the entire

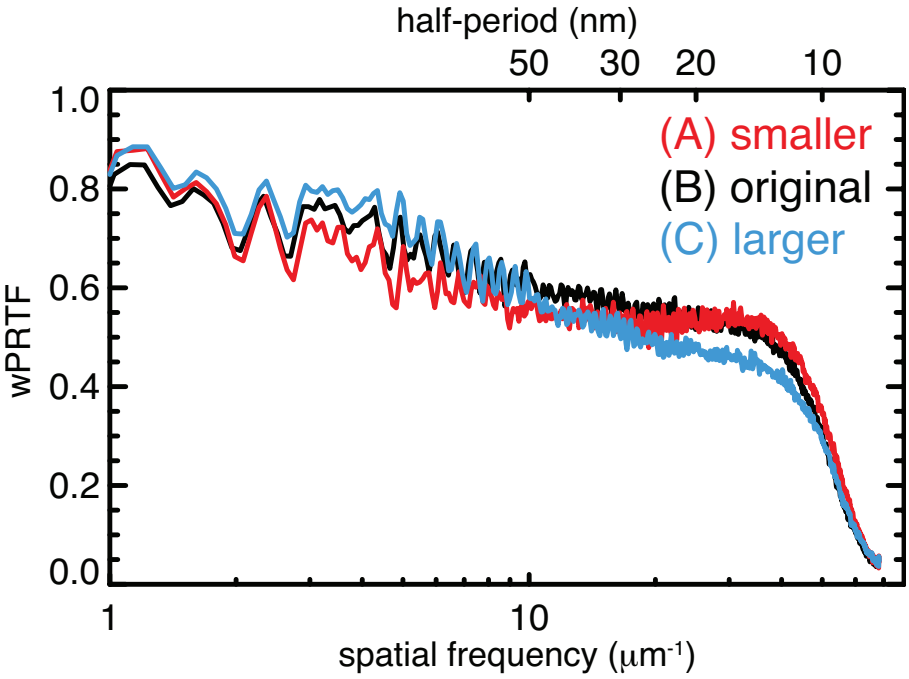

Figure 3.25: The Wiener filtered phase retrieval transfer functions (wPRTF) for the three slightly different supports from Fig. 3.25. The curve for the original support found using a combination of `Shrinkwrap` and hand modifications is shown in black (Fig. 3.25 B). The PRTF for a support that is slightly smaller than the original is in red (Fig. 3.25 C) while the one for a slightly larger support is shown in blue (Fig. 3.25 A). The larger support performs poorest at high spatial frequencies probably due to a blurring of fine features from the reconstructed object shifting slightly inside the support. Also at these high spatial frequencies the smaller support reconstructs the phases more reliably than the original support. At low spatial frequencies the smaller support performs worse while the larger support reconstructs better than the original. The original support was chosen as the final support constraint because it performs well over the entire spatial frequency range.

object (Fig. 3.26, right), the algorithm is not able to compensate. Not only is the missing area incomplete, but the overall reconstruction appears to be of poorer quality.

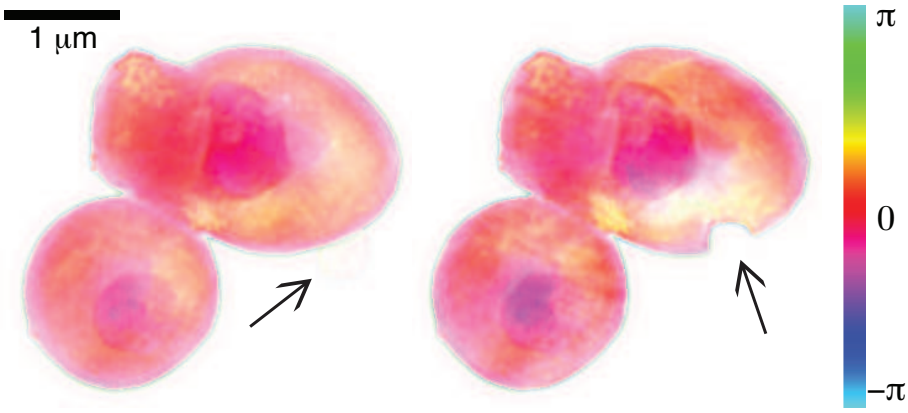

Figure 3.26: Reconstructions using the original support area with either an added (left) or removed (right) region. The Difference Map algorithm is easily able to ignore the extraneous support area (indicated with the arrow on the left) and added region is difficult to even discern. However, when a support guess does not include the entire object, the algorithm has difficulty and cannot complete the missing area (indicated by the right arrow). The identical reconstruction protocol as in Fig. 3.24 was used for both support guesses.

By plotting the respective Wiener filtered phase retrieval transfer function curves, one can also observe that the phases over all spatial frequencies are transfered more reliably when a support guess has an added, unnecessary region compared to missing a required region. Figure 3.27 shows that the wPRTF for reconstruction with an added area in the support guess (red) agrees very well with the reconstruction using the original support (black). The wPRTF for the support guess with a missing area is shown in blue. It is follows the general trend of the other two curves, but remains at a lower value for all spatial frequencies.

A similar study using simulated diffraction data from a fake, frozen hydrated cell was done with similar conclusions, but somewhat different results (Sec. 3.32 of [18]). As with the experimental data here, the Difference Map algorithm had little trouble ignoring the extraneous support area while struggling to fill in the information cropped by the support. Furthermore, the PRTF curves for reconstructions using the correct (black) and augmented (red) supports agreed with each other very well. The discrepancy between

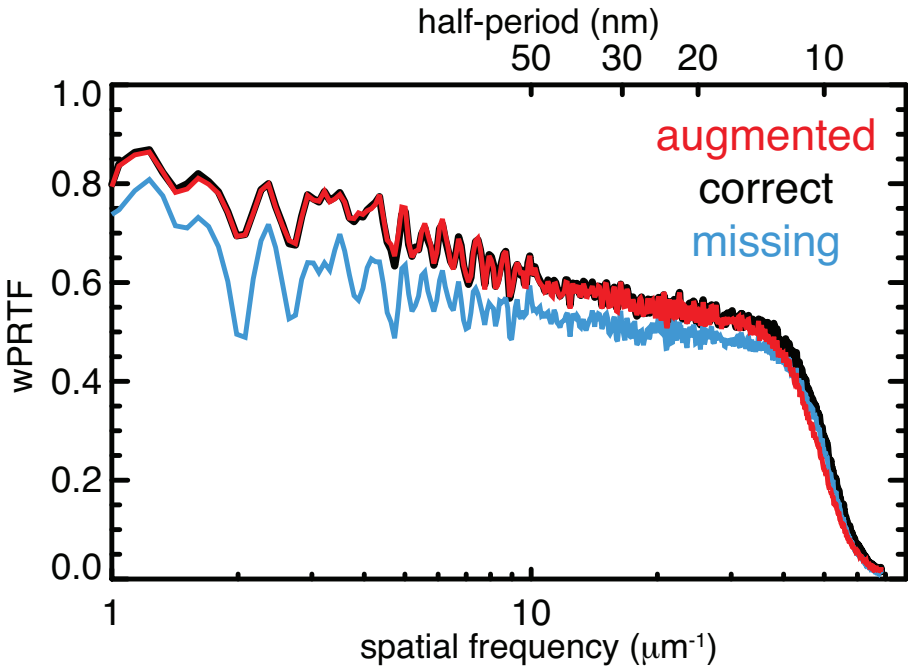

Figure 3.27: Wiener filtered phase retrieval transfer functions of the two reconstructed exitwaves in Fig. 3.26 compared to the original. The wPRTF of the reconstruction using a support with an added region (Fig. 3.26 left) is shown in red while the blue curve is the wPRTF using a support with a removed region (Fig. 3.26 right). The wPRTF of the reconstruction using the augmented support corresponds well with the wPRTF of the original support, which is plotted as a slightly thicker black curve. However, the wPRTF of the wavefield using the cropped support follows the trend of the other two curves, but is consistently lower. This supports the conclusions of Fig. 3.26.

the two studies only manifests in the PRTF of the reconstruction with the missing support area (blue). In the simulation study the PRTF jumps unnaturally high around 10 μm^{-1}, while in this study the curve follows the trend of the other two while remaining lower, even without the Wiener filtering (not shown). Repeating the simulation study using Wiener filtering on the PRTF curves would most likely suppress this jump in the PRTF.

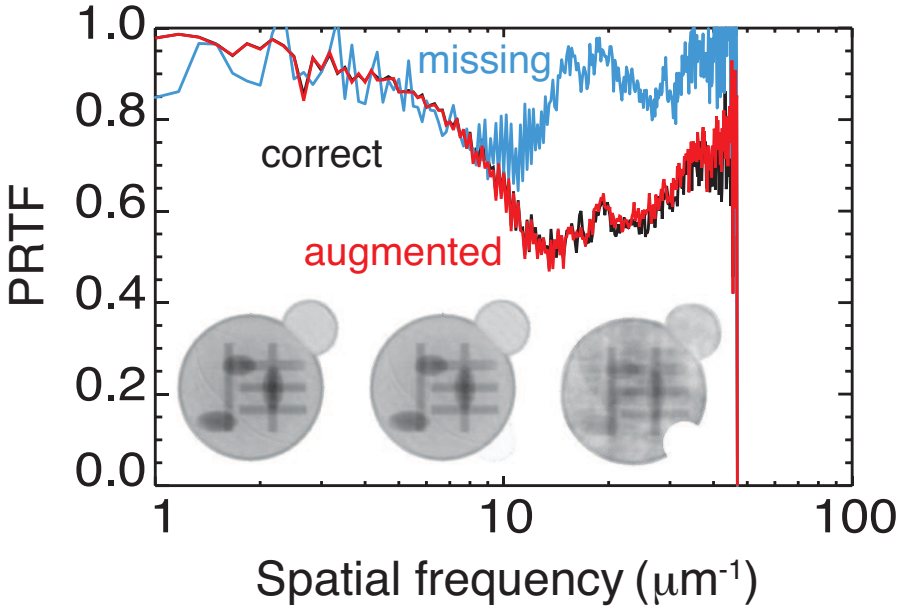

Figure 3.28: Phase retrieval transfer functions of the three reconstructed exit-waves of simulated diffraction intensities from a frozen hydrated cell (see inlay) using the perfect support (black), an augmented support (red), and a support with a missing region (blue). The PRTF of the reconstruction using the augmented support corresponds well with the PRTF of the perfect support. The support which is missing an area result in a reconstruction with a PRTF curve which appears unusually high. This is a drastically different result than from real data on freeze-dried yeast; however, this is unnatural jump would most likely be suppressed if the PRTF was Wiener filtered. Details of the simulation as well as the original figures can be found in Sec. 3.32 of [18].

The disagreement between these two studies highlights a two-pronged issue in XDM. Firstly, simulations, although invaluable, can sometimes lead to unrealistic results. Secondly, the use of the Wiener filtering is important for suppressing erroneous features in PRTF curves. Notably, despite the discrepancy, both investigations agree with the conclusion that extraneous regions in

a support guess are easily managed by Difference Map, while excluding part of an object from the support significantly reduces quality.

Both Figs. 3.27 and 3.25 mark the value of the PRTF curve in understand the quality of a reconstruction. Furthermore, they demonstrate the undeniable importance of the support constraint in achieving the most authentic reconstruction of the lost phase information. Significant amount of time and computer power can be spent on small modifications to the support constraints, but with the `Shrinkwrap` algorithm's ability to produce many subtly different support guesses using different initial phase starts and by employing the PRTF curves to quickly spotlight the premium supports, the process of finding the best support can become routine.

3.6.2 Performance of DM vs. HIO

Since Gerchberg and Saxton's [29] first phase recovery algorithm (Error Reduction) in 1972, many generalizations, variations, and improvements of the algorithm have developed including Fienup's Hybrid Input-Output [33] and Elser's Difference Map [34]. For a more detailed overview of the algorithms see Sec. 2.2.4 and Appendix B. While numerous simulated diffraction intensities have been used to compare many of these different algorithms and whether or not they are able to avoid stagnating at local minima [18, 33, 54], very little has been done in comparing algorithms on real data. In fact, any systematic comparison using real data is problematic since the true phases remain unknown.

Here we compare the results from reconstructing the phases of the freeze-dried yeast at 0° with two different algorithms, Difference Map (DM) (Appendix B.1) and Hybrid Input-Output (HIO) (Appendix B.2). Both algorithms are designed with feedback mechanism to avoid local minima. The reconstruction conditions used are identical to those described in section 3.3 and the support is the original (Fig. 3.24b). The results from the two different algorithms agree very well and both resulting wavefields have favorable features (Fig. 3.29). The three black arrows highlight examples of structures for which they are more visible on their respective reconstructions. From the wPRTF curves (Fig. 3.30) one can see that DM (black) slightly outperforms HIO (red) at low spatial frequencies, but they are otherwise equivalent. This poorer reconstruction of phases at lower spatial frequencies can be seen in the HIO reconstructed wavefield as the overall purple hue in the smaller, lower cell.

This short study comparing the Difference Map and Hybrid Input-Output algorithms is by no means comprehensive and further experiments using real data to investigate differences in performance of various algorithms are needed.

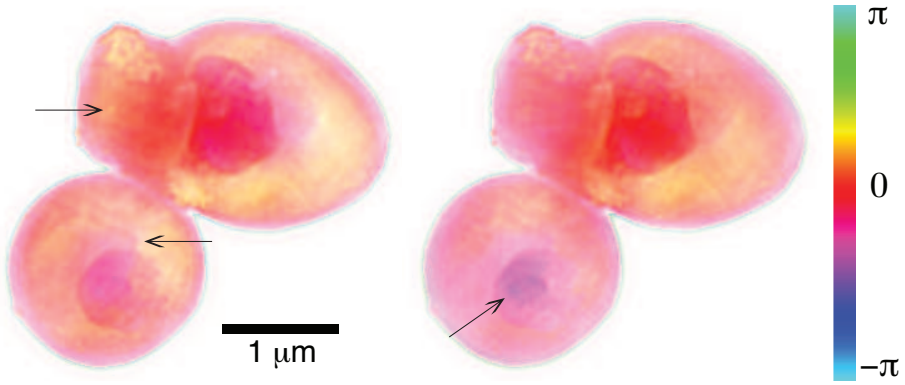

Figure 3.29: The complex exitwaves of the freeze-dried yeast at 0° reconstructed using the Difference Map algorithm (right) and Hybrid Input-Output (left) using the support from Fig. 3.24 B. The two algorithms result in very similarly retrieved phases and it is difficult to determine which algorithm is better for this particular coherent diffraction intensity pattern. The black arrows highlight three structures which are more visible on their respective images.

Nonetheless this study does gives more credibility to the reliability of the recovered phases. An interesting study would be a comparison of how well each algorithm finds a high quality, tight support. However, it is not clear to the author how this could be done on a biological specimen since using `Shrinkwrap` without any manual adjustments does not produce adequate support estimates.

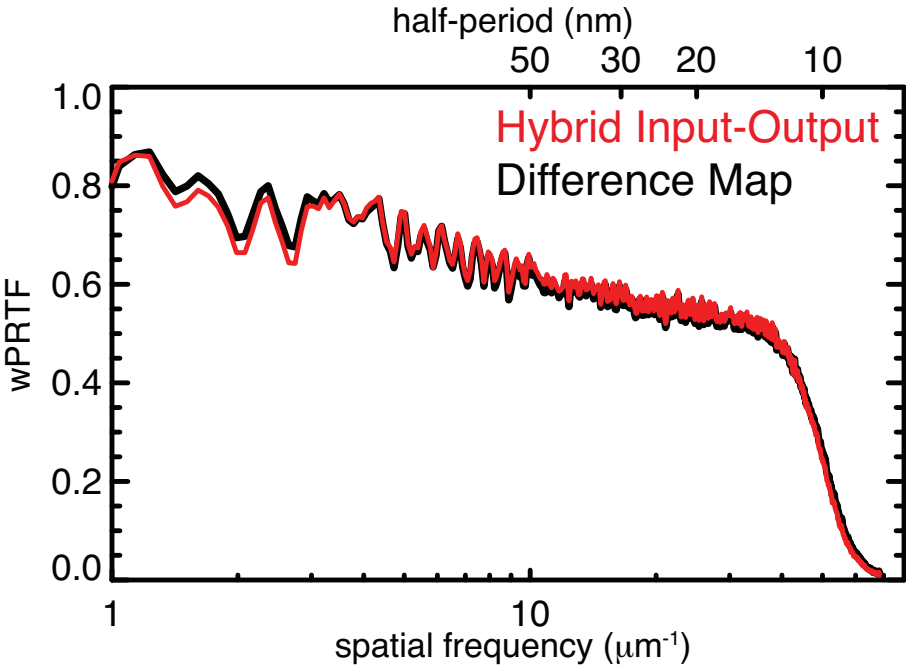

Figure 3.30: The wPRTF curves for both Hybrid Input Output in red and Difference Map in slightly thicker black using the support from Fig. 3.24b. Difference Map performs slightly better than Hybrid Input-Output at low spatial frequencies.

Chapter 4

XDM on frozen hydrated yeast

Chapter 3 describes in detail x-ray diffraction microscopy on freeze-dried yeast. Although the images boasts superb resolution and we have been able to determine the relative depths of different immunogold labels, a notable benefit of using X-rays over electrons was not exploited when imaging the specimen. X-rays can image biological samples embedded in much thick ice than electrons and their energy can be tuned to have sharp absorption contrast between water and organic material (Sec. 1.4.2). These properties of X-rays allow the much more biologically significant imaging of frozen hydrated material.

Cryogenic x-ray diffraction microscopy, although challenging, has already been demonstrated with our microscope on yeast using soft X-rays [55] and concurrently by another research team using harder X-rays on bacteria [56]. Since our collection of these frozen hydrated diffraction intensity data which have been successfully reconstructed, attempts have been made to collect higher quality frozen hydrated 2D data and move towards successfully reconstructing a frozen biological sample in 3D. The following chapter will discuss the biological motivation behind cryogenic imaging, summarize refinements which have been made to the microscope to improve frozen hydrated data, and outline a few potential weaknesses in the current system.

4.1 Benefits and complications of imaging frozen hydrated specimens

Section 1.4.1 highlights the increased radiation hardiness of samples that are imaged at cryogenic temperatures, but the true advantage of imaging in a frozen hydrated state extends beyond radiation damage. Water dominates the total volume of a cell, therefore it is not surprising that significant damage can be done by its removal. Substantial morphological differences have been seen

using electron microscopy between frozen hydrated cells and ones that have been fixed and critical-point dried [57]. Yet the majority of high resolution imaging to date is still performed on dehydrated cells.

One of the disenchantments of high resolution hydrated imaging is the stringent thickness limits electron microscopy sets on samples. Figure 4.1 plots the dose required to detect a 10 nm protein feature in various thicknesses of ice using either zero loss electron microscopy or 520 eV X-rays assuming ideal optics and detectors [58]. Three different electron beam voltages are shown as solid lines while the dashed lines show the absorption and phase contrast of 520 eV X-rays. From this plot it is clear that electron microscopes excels at ice thicknesses below 0.5 μm and high resolution images can be achieved at minimal doses. However with ice thicknesses greater than $1-2$ μm X-rays are necessary as the electron microscopy dose skyrockets. Despite this advantage, presently only two x-ray microscopes world-wide are equipped to routinely image frozen hydrated biological material; one in Berkeley, CA [59] and the second in Berlin, Germany [10]. Typically high resolution imaging on large specimens such as eukaryotes and tissue samples are performed by freezing samples whole and subsequently slicing them into very thin sections for electron imaging [60]. This technique makes imaging small, individual structures such as the single spindle pole body depend on the luck of where the cell was sliced and 3D microscopy impossible. It can also introduce cutting artifacts.

To properly prepare specimens in a frozen hydrated state the water, both surrounding and internal, must be cooled to a vitreous state. If crystals assemble inside the specimen, internal structure can be damaged. To avoid crystallization during cooling, thin samples can be rapidly frozen by plunging them into cryogenically cooled gas such as ethane or propane. Liquid helium or nitrogen cannot be used directly for cooling because both cryogens create a layer of thermally insulating gas around a warm specimen significantly reducing the cooling rate (Leidenfrost effect). Samples thicker than 10 μm must be cooled at high pressure (200 MPa) because of the lower cooling rates of the samples' centers. However, cooling rates faster than what is required for the vitrification of water (10^3 K s^{-1} at ambient pressure) are preferred to reduce artifacts from structural and molecular rearrangement as the cooling front travels through the specimen [61]. Nevertheless, even a relatively slow cooling rate for cryogenic fixation is 10,000 times shorter than any alternative chemical fixation rate [62]. Because yeast with the *whi5* mutation average around $3-4$ μm in diameter, we are able to rapidly plunge freeze our samples using an automated vitrification device, Vitrobot, from FEI (Hillsboro, Oregon). The Vitrobot allows reproducible sample freezing for high quality

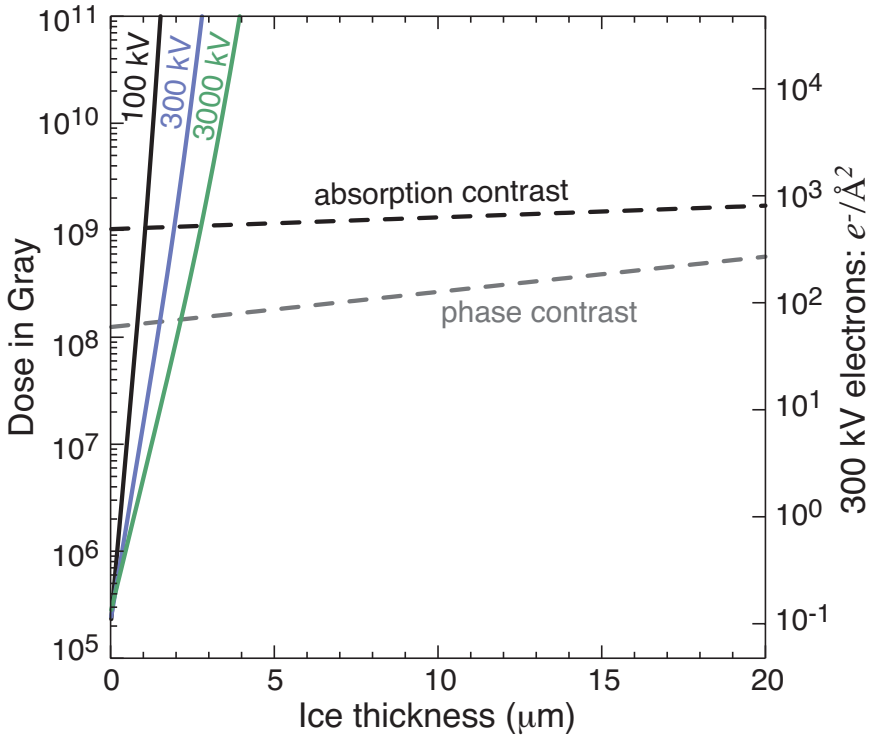

Figure 4.1: Plot of dose required to detect 10 nm protein in various thicknesses of ice with either electrons or X-rays [58]. Three different electron beam voltages are show as solid lines while the dashed lines are the absorption and phase contrast of 520 eV X-rays. XDM is sensitive to both the absorption and phase contrast. Although electron microscopes are ideal for imaging protein in less than 0.5 μm ice, beyond $1-2$ μm X-rays are required.

vitrification and high sample throughput.

4.1.1 Ice bubbling limit

Although frozen hydrated cells are dramatically more radiation hardy than room temperature samples, radiation damage has been documented in both cryo electron and x-ray microscopy. Carbon oxygen double bonds have been shown to break by x-ray doses of less than 10^6 Gray on liquid nitrogen cooled PMMA film while massloss was curtailed until the film was warmed [15]. In addition, hydrogen gas bubbles have been shown to form in the ice surrounding frozen polymer spheres exposed to electron doses above 10^9 Gray [63]. The gas is trapped by the surrounding ice and not able to inflict secondary damage to organic material. Some x-ray microscopy groups informally report experience with bubbling at high doses, but no systematic study has yet been published.

In an attempt to quantify the dose and x-ray energy at which bubbling occurs in cryo x-ray microscopy, we exposed frozen hydrated yeast to high doses of x-rays using a transmission x-ray microscope (TXM) at *Berlin Elektronen-speicherring-Gesellschaft für Synchrotronstralung II* (BESSY II) in Germany. The objective zone plate had an outer most zone width of 25 nm giving an estimated resolution of the microscope of 30.5 nm. TXM images of frozen hydrated *whi5* yeast were taken at different X-ray energies, either across the nitrogen K-shell absorption edge (from 395 eV to 415 eV) or the oxygen edge (from 525 eV to 545 eV) in 0.2 eV steps. Although both energy scans begin to show radiation damage after around 2 minutes of accumulated exposure, the particular manifestation of the damage seems to be energy dependent. The damage from the scan across the nitrogen absorption edge is internal structural damage and an expansion of the entire cell (Fig. 4.2), while the damage across the oxygen edge is exhibited with the formation of bubbles around the cell as well as some internal degradation (Fig. 4.3). The total exposure time for each of the scans ss around 3.4 minutes. Unfortunately no reliable measure of dose is avaliable; however, if one estimate the 2 second exposure as the minimum exposure required to detect 30 nm structure with 10% zone plate efficiency [58] then the 2 minutes of exposure before radiation damage was visible corresponds to a dose greater than 10^9 Gray.

4.2 Ice quality and cell identification

One of the most difficult challenges when imaging frozen hydrated specimens is that they must be kept frost free and below the crystallization transition temperature of ice (136 K) at all times. Typically frozen specimens

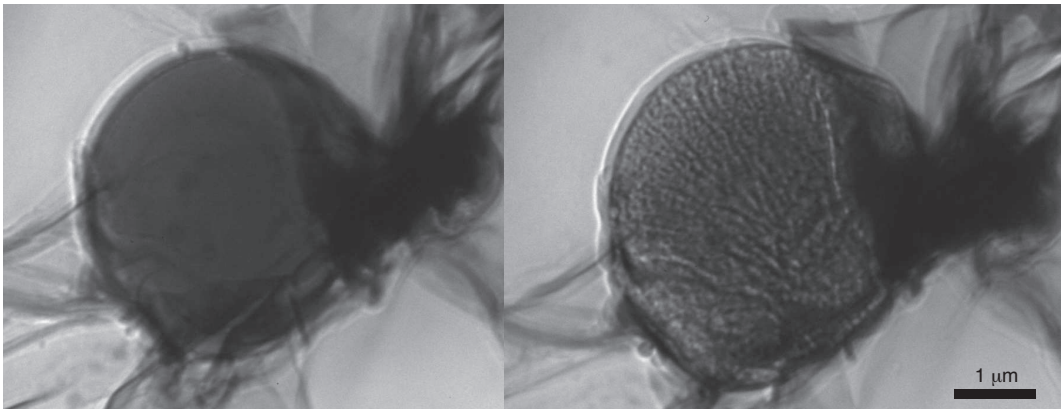

Figure 4.2: Transmission x-ray microscopy (TXM) images of frozen hydrated yeast at 395 eV before (left) and after (right) an energy scan across the nitrogen absorption edge from 395 eV to 415 eV in 0.2 eV steps. Radiation damage from the scan is evident in the lack of internal structure and the expansion of the cell (right). Damage first appeared after around 2 minutes of exposure, an estimated dose of more than than 10^9 Gray, and the total exposure time accumulated is around 3.4 minutes. Images were recorded at BESSY II in Berlin.

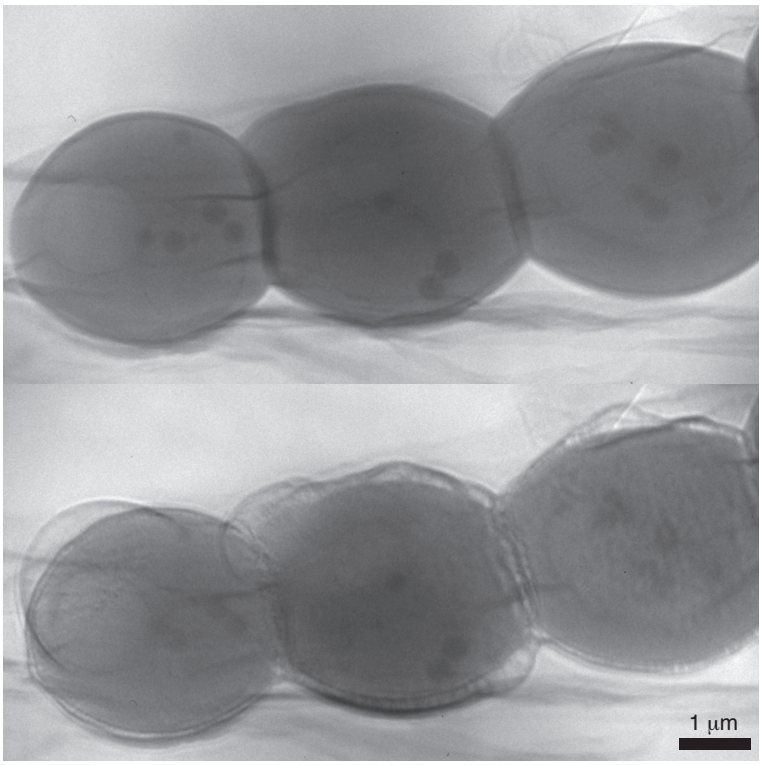

Figure 4.3: Transmission x-ray microscopy images of frozen hydrated yeast at 525 eV before (top) and after (bottom) an energy scan across the oxygen absorption edge from 525 eV to 545 eV in 0.2 eV steps. Radiation damage from the scan is most evident in the bubbles which have formed in the ice around the cell (right). Unlike the damage seen from the scan across the nitrogen absorption edge (Fig. 4.2), the internal structure after this scan is still visible. Damage first appeared after around 2 minutes of exposure, an estimated dose of more than than 10^9 Gray, and the total exposure time accumulated is around 3.4 minutes. Images were recorded at BESSY II in Berlin.

are stored under liquid nitrogen and imaged either in vacuum or in cold, dry nitrogen gas. This requirement gives frozen hydrated samples a very short lifetime in contrast to dried samples, which can be kept on a shelf without much difficulty for years. Furthermore, it makes the inspection of samples for ice crystallization and cell concentration difficult. Although not required, the ability to visualize specimens in real space before recording diffraction intensities is important.

Figure 4.4 shows a TXM image taken at BESSY II of a budding yeast with large ice crystals in the ice surrounding the cell as well as small crystals which have formed inside the cell's vacuole (indicated by an arrow). These crystals either formed during the rapid freezing process or as a result of the specimen warming during transfer into the microscope. Such characteristics of poor ice quality are difficult to determine from x-ray diffraction intensity information alone. In the following section, we outline a few upgrades we have implemented into our XDM experiment to extend our knowledge of our typical ice quality and be able to view grids before x-ray imaging.

4.2.1 Out-of-vacuum light microscope

With the intention of better understanding our vitreous ice quality in general and the possibility of correlative microscopy, we recently purchased a cryogenic specimen stage from Instec (Boulder, CO) which we have fit into a standard Nikon 50i light microscope (Fig. 4.5). The cryo stage uses dry, cold nitrogen gas to maintain a climate of 83 K for low resolution (0.3 numerical aperture) cryo imaging of up to nine EM grids. Warm, dry nitrogen is blown across the glass of the cryo stage to keep it defrosted. Currently the system images in transmission, but a long working distance phase contrast condenser is being designed by Instec to fit the phase rings on the objective lenses. With Zernike phase contrast we will be able to determine the ice thickness as well as better visualized cells and ice crystals which are both almost completely transparent to visible light. In addition, a second system has been purchased which also include fluorescence capability for visualizing DAPI (4',6-diamidino-2-phenylindole), Fluorescein isothiocyanate (FITC), and Texas Red fluorophores. This will allow easy differentiation of cells from round ice structures with DNA staining using DAPI as well as the possibility of correlative microscopy using fluorescence tags.

Using the currently available absorption contrast we have observed that ice can form droplets instead of a uniform film on the support film of the electron microscope (EM) grid on which we mount our frozen hydrated specimens. Figure 4.6 shows a distinct separation in ice which has formed $30 - 20$ μm diameter droplets and area of very smooth ice with no droplets. We have

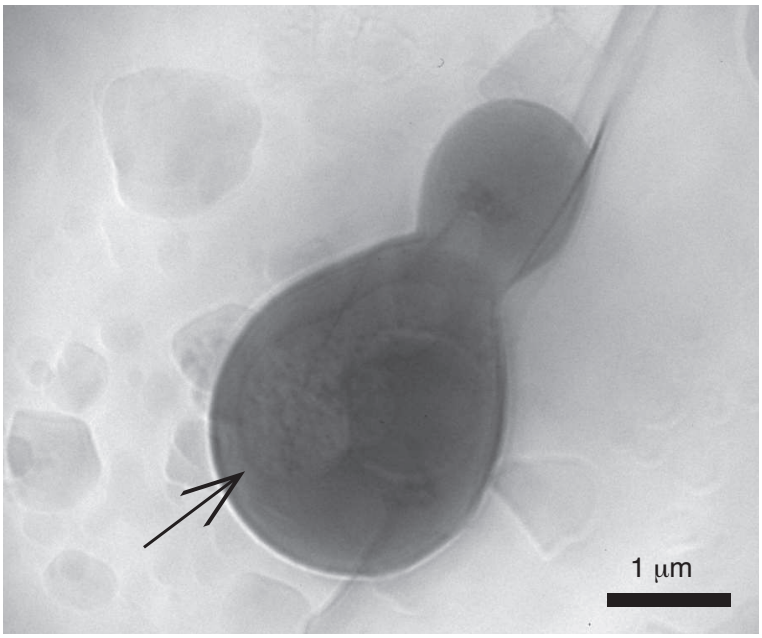

Figure 4.4: Transmission x-ray microscopy image of frozen hydrated budding yeast taken at 510 eV at BESSY II in Berlin. Large ice crystals can be seen in the surrounding ice as well as smaller crystals inside the cell's vacuole (indicated with an arrow), which appear as granular structure. Internal ice crystals such as these are difficult to determine from diffraction intensity information alone making pre-imaging inspection of cells important.

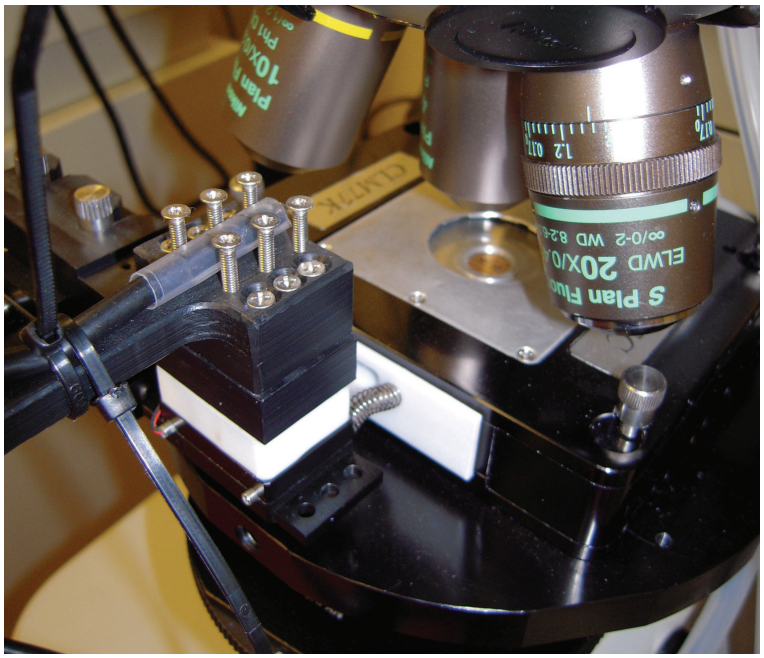

Figure 4.5: Cryo stage from Instec (Boulder, CO) mounted on a standard 50i Nikon microscope for low resolution imaging of frozen hydrated cells. The system currently operates using absorption contrast, but future upgrades will include Zernike phase contrast and fluorescence.

observed that the droplets can be prevented from forming by plasma cleaning EM grids before samples are frozen. Plasma cleaning increases the wettability of the grid substrate thereby increasing the likelihood that water will form a thin film. We believe this clear boundary stems from the uneven pressure applied to the grid by the Vitrobot's blotting pads when excess water is blotted from the grid immediately before rapid cooling. The nonuniform pressure leaves behind varying amounts of residual water. It is likely that the region with no droplets has little to no ice. Without phase contrast it is impossible to accurately estimate the thickness of the ice film. It is also unclear from the low resolution light microscope images whether or not the yeast in this area has air-dried before freezing. Typically the humidity around the grid during blotting and before plunging is kept near 100% to prevent air drying.

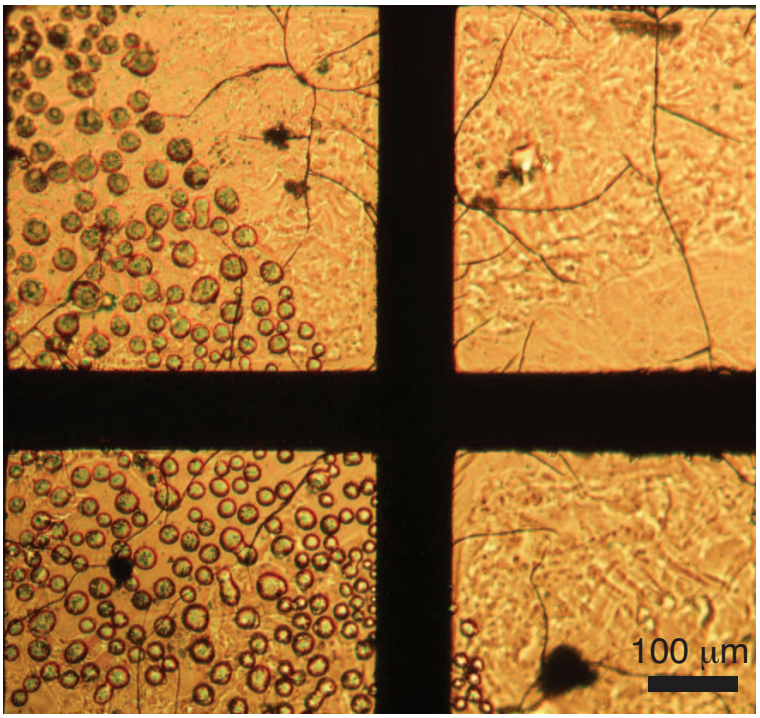

Figure 4.6: Absorption contrast image of a frozen hydrated electron microscope (EM) grid using the out-of-vacuum cryo visible light microscope. There is a clear boundary between the area on the left with large $30-20$ μm diameter ice droplets and the area on the right with a very thin or no ice film. Nonuniform pressure from the Vitrobot's blotting pads can account for these two distinct regions. The droplets can be prevented by plasma cleaning specimen grids before freezing.

4.2.2 In-vacuum light microscope

A second visible light microscope was built into the x-ray diffraction microscopy vacuum chamber to image specimens immediately before data collection. This microscope can be aligned to the x-ray beam using a pinhole mounted at the sample plane and is useful for locating particular areas of clean, uniform ice as well as specific cells. Previously, regions of interest were located using the shadow of the EM grid on the CCD from the pinhole scatter when the corner, which typically blocks the scatter, is removed (Sec. 2.3.2). Figure 4.7 shows an example of a shadow from a nonstandard, rectangular EM grid. Large structures such as cracks in either the substrate or the ice as well as some large ice structures caused by the frozen grid being exposed to humid air during grid handling are visible in the shadow image. Individual cells cannot be identified from the x-ray shadow since the projection from a single 3 μm cell is on the order of the size of one pixel on the CCD.

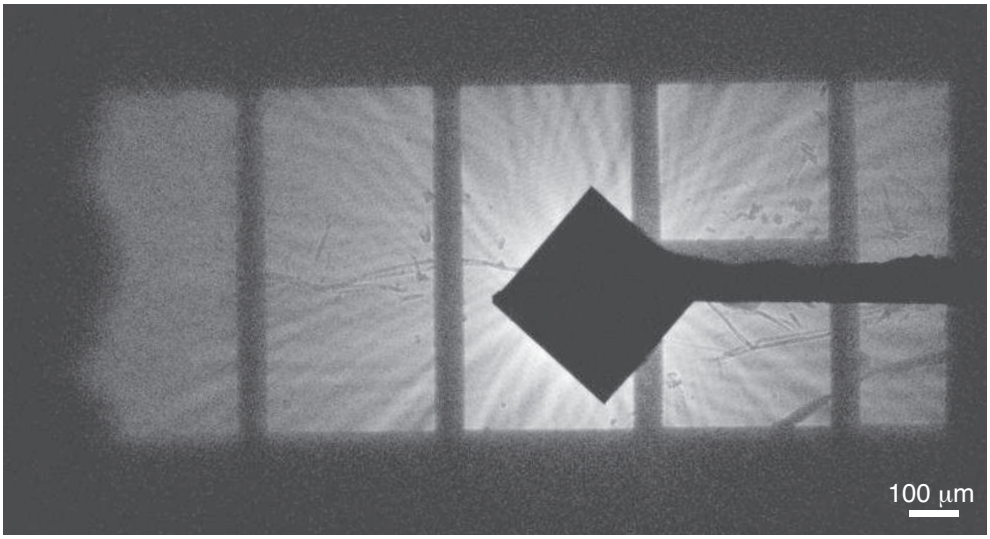

Figure 4.7: Example of a shadow produced from x-ray scattering from the pinhole when the corner is removed. Cracks in either the grid substrate or the ice are visible along with large ice structures which formed when the cold grid was accidentally exposed to humid air.

The in-vacuum light microscope operates by illuminating the specimen with an LED and collecting the transmitted light with a Nikon long working distance objective lens that can be either a 50× lens with 0.55 numerical aperture or a 20× objective with 0.4 numerical aperture for lower resolution,

but larger field of view. Unfortunately, due to a very tight constraint on available space, it is not possible to switch between objective lenses without venting the vacuum chamber. A single bounce off a dielectric prism mirror brings the light out of vacuum through a viewport and into a telephoto zoom lens with a CCD camera mounted directly behind it. All of the in-vacuum light microscope's optics are on motorized stages to allow quick transition between visible light and XDM imaging modes. The telephoto zoom lens is a manual zoom video lens that can screw directly into the front of the CCD camera. It has a focal length range of 2.0 – 200.0 mm and a 7× magnification. For this microscope setup the lens is set to image from infinity. The CCD camera is a Hitachi 1/2 inch color camera. Figure 4.8 is a schematic of the in-vacuum microscope setup.

Figure 4.9 shows ice droplets similar, yet smaller, to those seen in the out-of-vacuum light microscope (Fig. 4.6). This particular substrate has regularly spaced 5 μm holes, which are visible in this image as paler blue circles. We had thought that this holed substrate could be used to encourage cells to space themselves out if an individual cell would prefer to sit within a hole. However, from our experiences water tension appears to prevent this favorable settling of cells. The smallest of the round structures are most likely yeast cells instead of water droplets. This highlights the difficulty in distinguishing round ice structures from cells using a low resolution image. Ideally, a grid should be free of any ice droplets so the confusion is not possible and the ice layer is uniform.

Figure 4.10 demonstrates a second undesirable frozen hydrated condition also visible using the in-vacuum light microscope. In this case, the ice layer has not formed droplets, but instead what appears to be ice crystals. This ice texture is closely spaced compared to the droplets as well as being more irregular in shape. By moving the ice layer in and out of focus, we have also determined that this structure is notably thinner than the droplets. These ice crystals were caused either by a freezing rate that was too slow or from the frozen grid warming above the transition temperature between vitreous and crystalline ice (136 K) during sample handling.

Other notable flaws visible on this frozen grid are the two large, dark structures and the crack lined with yeast cells that runs the height of the image. The former is ice contamination which is a result of exposure to humid air. This blemish is also visible in the example of the x-ray shadow (Fig. 4.7). The latter illustrates the tendency of cells to collect along the length of cracks, suggesting that these cracks are imperfections in the substrate caused by the blotting of excess water from the grid before cells are frozen in place.

Figure 4.11 is an example of an EM grid with high quality ice visualized

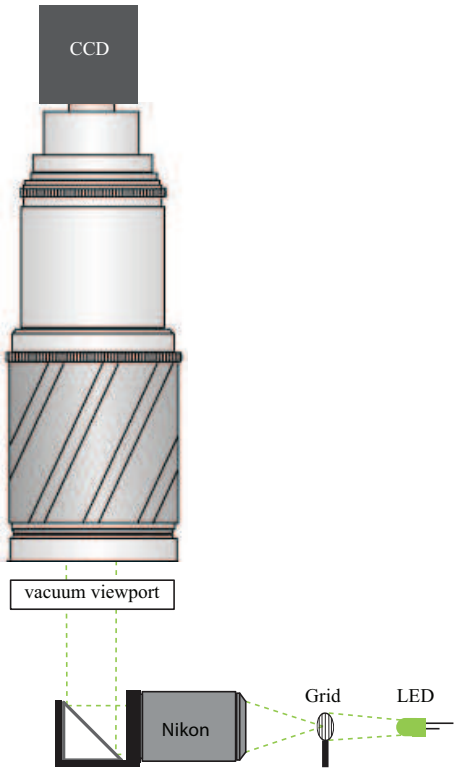

Figure 4.8: Schematic of in-vacuum light microscope. The EM grid is illuminated by an LED and the transmitted light is collected by a Nikon long working distance objective lens. A single bounce off a dielectric right angle mirror sends the light out of the vacuum chamber through a viewport and into a telephoto zoom lens attached in front of a Hitachi 1/2 inch CCD camera. Diagram is not to scale.

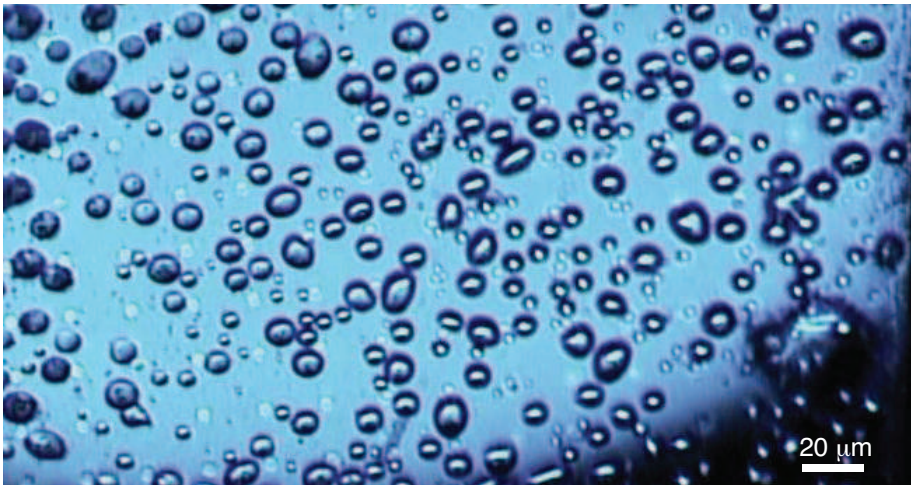

Figure 4.9: Transmission image of ice droplets on an EM grid with a substrate called Quantifoil which has regularly spaced 5 μm holes using the in-vacuum visible light microscope. The smallest of the droplets are most likely yeast cells, which highlights the uncertainty in distinguishing cells from droplets. The lower right shows uneven illumination from the limited motion of the motor on which the LED is attached.

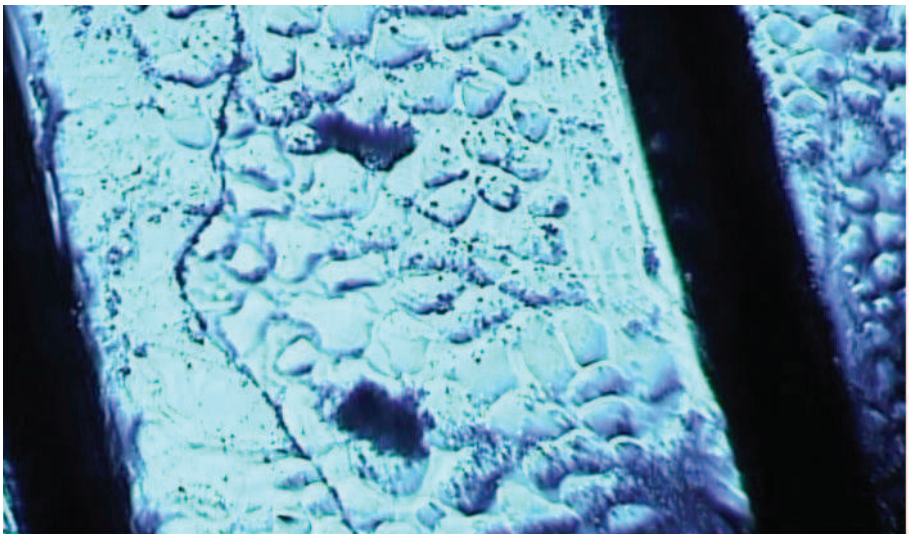

Figure 4.10: Transmission image of flaws on a frozen EM grid using the in-vacuum visible light microscope. The textured ice is thought to be crystals either from too slow of an ice cooling rate or allowing the frozen grid to warm above 136 K. The crack which runs the height of the image is dotted with cells revealing that this is a flaw in the substrate created before the cells were frozen in place. Finally the two large, dark structures are ice contamination from contact with humid air.

in the in-vacuum light microscope. The small, dark circles are assumed to be yeast cells, while the lighter circles are cells that are out of focus and a few are dust particles on the prism mirror. The very large, dark mass in the upper left corner attached to the grid bar is ice contamination similar to that visible in other images. An ice crystal with cells contained within is visible on the right.

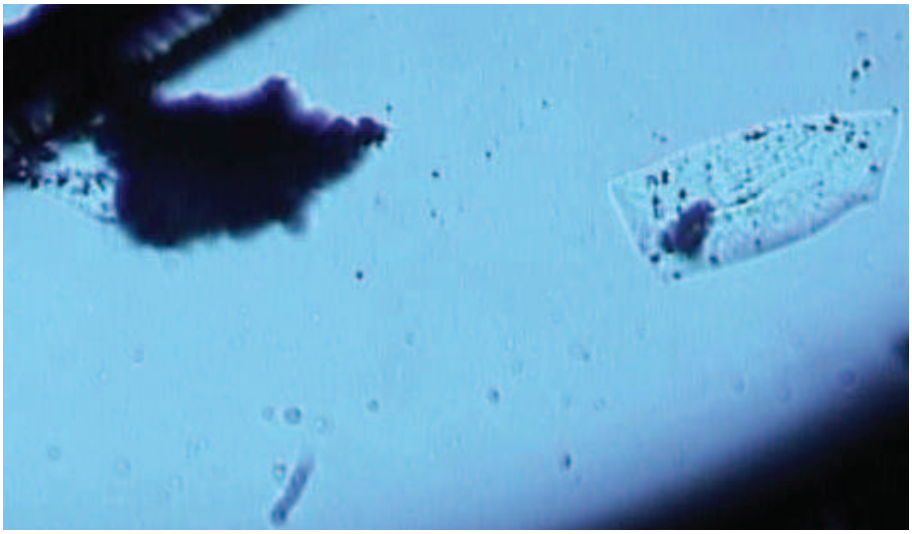

Figure 4.11: Transmission image of an EM grid with high quality ice using the in-vacuum visible light microscope. The small, dark circles are assumed to be yeast cells, while the lighter circles are mostly cells which are out of focus and a few are dust particles on the prism mirror. The very large, dark mass in the upper left corner is ice contamination from contact with humid air and an ice crystal is visible on the right. The lower right shows uneven illumination from the limited motion of the motor on which the LED is attached.

4.2.3 In-vacuum ice accumulation

An additional potential show-stopper for imaging frozen hydrated specimens is the collection of ice and other contaminates onto the cold grid while it sits inside the microscope vacuum chamber. The insertion of a frozen sample into the vacuum introduces moisture to the chamber and the cold sample acts as a cryopump as contaminates tend to condense on its surface. This phenomenon is not visible at the resolution of the in-vacuum light microscope, but does manifest as a broad peak in the diffraction pattern (Fig. 4.12). This

peak is characteristic of scattering from randomly distributed particles in the size range of 50 to 100 nm [28] and can dramatically reduce the visibility of coherent scattering from a frozen hydrated sample.

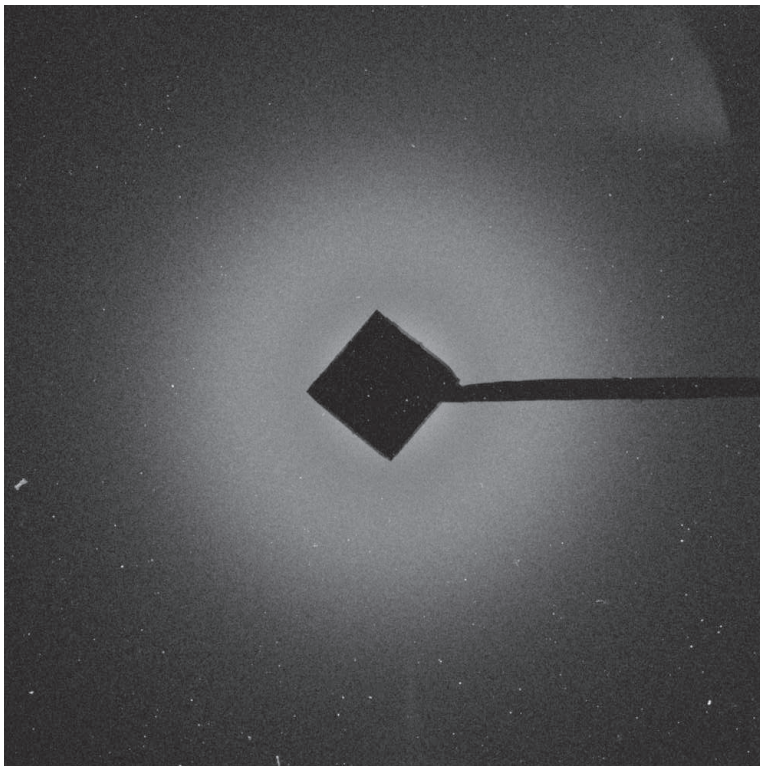

Figure 4.12: An example of diffraction from a clean area of a cold grid which has become contaminated by molecules condensing on its cold surface. Such background scattering can drastically reduce the visibility of coherent scattering from a frozen hydrated sample. This image was taken in February 2010.

Such contamination buildup is also observable in cryo electron microscope (EM) studies and anti-contamination devices are used to reduce the collection of contaminates onto the sample [60]. These devices are typically cryogenically cooled shields which cover at least two surfaces of the sample. A similar system was added to our microscope and has been shown to increase the time before the diffraction ring develops on a clean, cold sample grid from one hour to more than 16 hours [18, 64].

Since the initial test of our anti-contamination device, we have considered two factors which may additionally contribute to ice contamination. The first is the possible dependence on the particular EM cryo sample holder used.

Figure 4.13 shows our two sample holders from Gatan (Pleasanton, CA) both of which allow imaging of frozen hydrated samples to high tilt angles. (A) is a Gatan 630 which is the older of the two holders and uses nonstandard, rectangular EM grids. The published ice contamination tests were performed using this holder [18, 64]. (B) is a Gatan 914 which is newer and uses the standard, round 3 mm EM grids. The second possible contributing factor to ice contamination is how recently vacuum grease was applied to the two o-rings which create the vacuum seal on the cryo sample holder (labeled in Fig. 4.13).

To test these two factors the ice contamination was tracked similarly to the earlier studies [18, 64] using the anti-contamination device and either the Gatan 914 holder with greased and ungreased vacuum o-rings or the Gatan 630 holder with greased o-rings. Figure 4.14 shows the change in the power spectral density (PSD) from a clean area of a cold, dry grid sitting in the vacuum chamber for an hour for the three scenarios. The ungreased Gatan 914 test was done on February 23, 2010, with a microscope chamber pressure of 2.4×10^{-7} torr. The greased Gatan 630 test was done in the same month on the 28^{th} also with a chamber pressure of 2.4×10^{-7} torr. Finally, the greased Gatan 914 test was done the on May 3, 2010, with a chamber pressure of 3.5×10^{-7} torr. The tests were performed using different CCD detectors and varying incident flux. Although the PSD have not been normalized to account for these differences, a distinct peak centered approximately around 10 μm^{-1} is evident in both tests using a grid mounted in the 914 holder. These peaks (shown in black and cyan) correspond to the accumulation of particles averaging 50 nm in size. Because the CCD counts have not been normalized, comparing the relative sizes of peaks cannot inform us on whether the greased o-rings results in a slight improvement. In drastic comparison, the red line shows no significant change in the power scattering from the clean grid after one hour in the vacuum using the older 630 holder with greased o-rings. These results are also independent of the time between the last venting of the vacuum chamber and the implementation of the test. This time frame for the Gatan 630 holder was six days and was one day or five days for the Gatan 914 holder for the ungreased or greased o-rings respectively.

It is evident that the Gatan 914 does not seal as well as the older Gatan 630, but allows moist air to enter through the sample airlock and contaminate the grid within an hour of exposure to the vacuum. Since the poor vacuum seal is very close to the sample, the anti-contamination device is not able to capture the moisture before it collects on the grid. Perhaps the cryo holder could be returned to Gatan for a quality inspection and a possible swap of vacuum o-rings. Otherwise, dry nitrogen gas could be blown across the sample airlock area to displace the moist air. One could even consider creating a small,

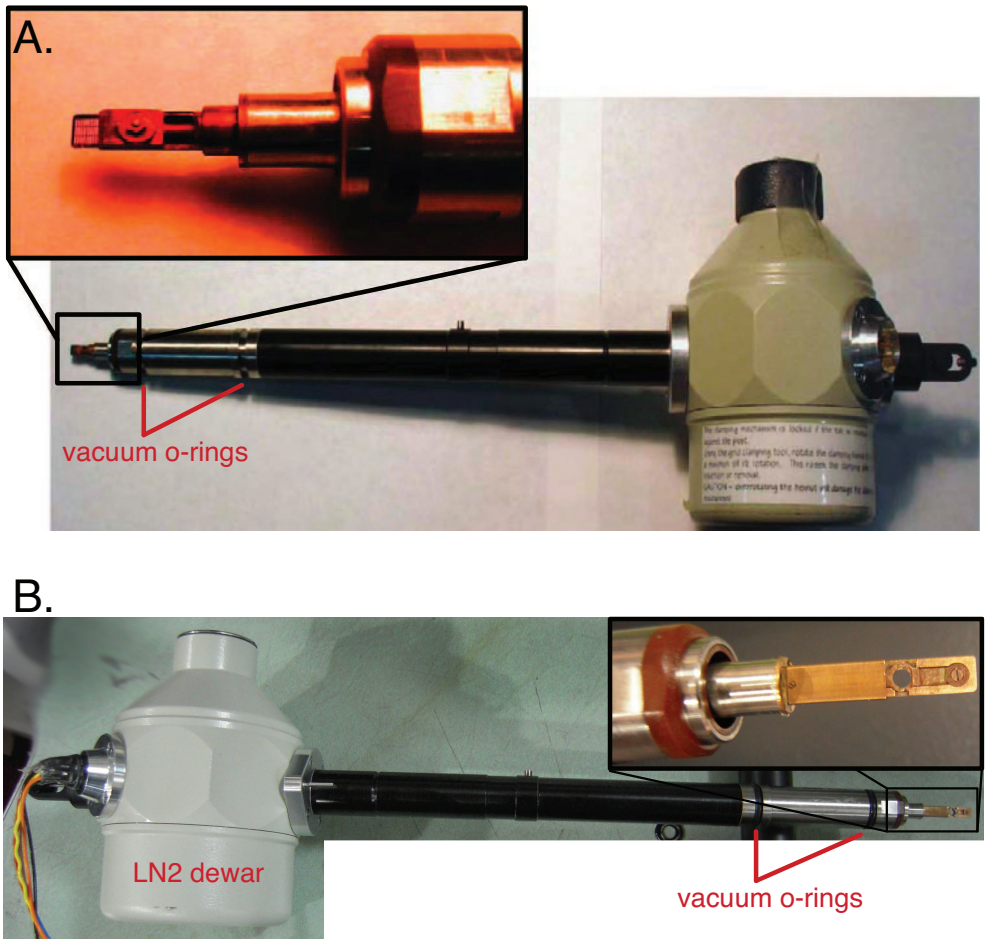

Figure 4.13: Two cryo sample holders from Gatan which allow high tilt imaging of frozen samples mounted on electron microscope (EM) grids that are cooled conductively through a rod attached to a small liquid nitrogen dewar. (A) is an older Gatan 630 holder which requires nonstandard, rectangular EM grids. The zoomed-in image of the tip shows a mounted, rectangular grid that can be covered for transfer through air by retracting it into the tip. (B) is a newer Gatan 914 holder which can hold the standard, round EM grids. A copper sheath can be slid over the grid for frost-free transfers through air. Ice contamination on the cold grid while sitting in the microscope vacuum chamber may depend on the cryo holder used or on how recently the two vacuum o-rings have been greased.

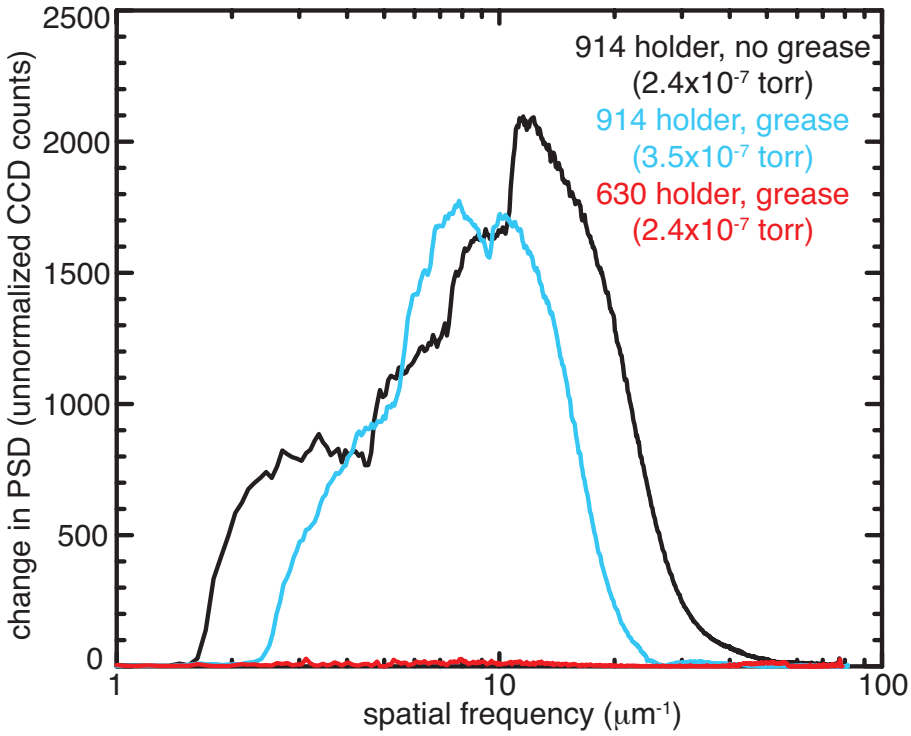

Figure 4.14: Plot of the change in power spectral density (PSD) from a clean area of a dry, cold grid after one hour of exposure to the vacuum. Scattering drastically increases for spatial frequencies around 10 μm^{-1} for a grid mounted in the Gatan 914 cryo holder whether or not the holder's vacuum o-rings have recently been greased (black, cyan). No change in scattering is seen with a similar grid mounted on the Gatan 630 cryo holder after an hour in vacuum (red).

contained environment such as a re-sealable bag around the sample holder and airlock into which dry nitrogen could be pumped.

4.3 Higher energy contamination

A potential source of poor coherent diffraction intensity pattern quality from cryo samples is contamination from a higher energy when working with 520 eV X-rays. Although not exclusive to frozen hydrated specimens, typically this lower energy is used only with frozen samples when it is advantageous to work below the oxygen K-shell absorption edge (Sec. 1.4.2). Because of the nature of using a zone plate monochromator with pinhole (Sec. 2.3.1), different energies of different zone plate orders can fall on the same focal distance as the desired energy, thereby contaminating the monochromaticity of the beam through the pinhole.

Previous x-ray diffraction microscopy reconstructions of frozen hydrated specimens were from data collected prior to an upgrade to the grazing-incidence mirror which bends the undulator X-rays down 9.0.1 beampipe and using a order sorting mirror system which eliminated the 1040 eV energy [55, 65]. This new grazing-incidence, multilayer mirror has a significantly different reflectivity curve than the previous nickel one and the set of order sorting mirrors were removed from the beamline because they were difficult to align and were believed to be nonessential.

At our typical room temperature sample imaging energy of 750 eV the higher order energies are not a consern. The higher energies which would focus to the same pinhole location are either from a second order zone plate focus (1500 eV), which is theoretically focused at 0% efficiency or are reflected poorly off the new multilayer mirror (2250 eV).

In this section we will calculated the expected ratio of CCD counts from unwanted energies to the 520 eV signal. We will then demonstrate that although the signal from 1560 eV photons on the detector is not theoretically negligible, reconstructions of contaminated diffraction patterns from simulated frozen hydrated cells are still possible.

4.3.1 Calculation of unwanted energies

To calculated the expected ratio of other energy signal to 520 eV signal on the CCD, we must consider how the different x-ray energies from the undulator are treated by the beamline optics. Upstream of the x-ray diffraction microscopy vacuum chamber are four components which alter the peaked energies from the undulator (Fig. 4.15): the multilayer mirror, beryllium

mirror, aluminum coated silicon nitride window, and monochromator zone plate segment with pinhole.

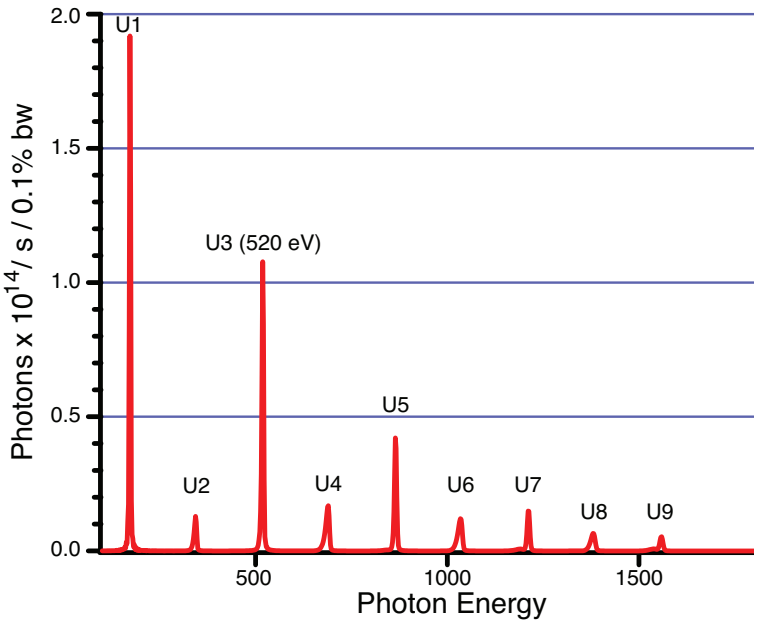

Figure 4.15: Theoretical plot of photons per second of different harmonics from the U10 undulator set to the energy gap used for 520 eV imaging. The 520 eV energy peak corresponds to the third harmonic (U3). The ninth harmonic (1560 eV) has a third order zone plate focus, which corresponds to the first order focus of 520 eV. Plot courtesy of Jan Steinbrener.

First let us consider which undulator energies will be indistinguishable by the monochromator zone plate and pinhole system. Figure 2.2 (Sec. 2.3.1) is a schematic of this system where different energies are focused to different locations along the beampipe. The pinhole is placed at the focal length of the 520 eV focus and blocks all unfocused light. However, zone plates have multiple foci where only approximately 10% of the X-rays are focused to the first order focal length and $\sim 1.1\%$ are focused to the third order. There is only one undulator harmonic that has a higher order zone plate foci, which would contaminate the 520 eV first order focus. The ninth harmonic's third order zone plate focus (1560 eV) will overlap the third harmonic's first order focus (520 eV). The sixth harmonic's second order focus (1040 eV) would also coincide; however, even ordered foci have theoretically zero efficiency so that they can be considered negligible.

Next let us calculate the relative efficiency of 520 eV and 1560 eV from the beamline optics. The relative undulator output for 1560 eV is 5% of the 520 eV output. The multilayer mirror reflectivity curve shown in Fig. 4.16 favors the 500 to 1000 eV energy range with a second reflectivity peak around 1500 eV. The mirror reflects approximately 70% of the 520 eV photons and 52% of 1560 eV. Both the beryllium window and the aluminum coated silicon nitride window favor higher energies. Their transmission curves are plotted in Fig. 4.17. The 0.5 μm thick beryllium transmits 50% at 520 eV and 97% at 1560 eV, while the 200 nm aluminum coated silicon nitride window transmits 41% and 80% respectively.

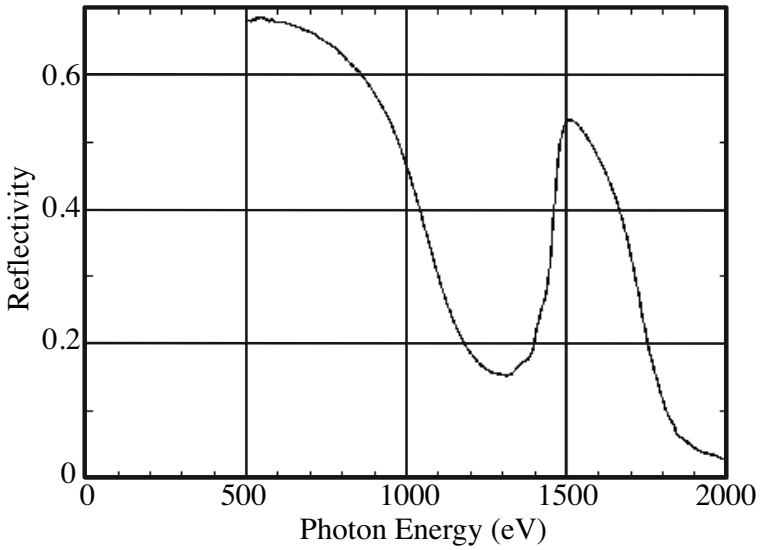

Figure 4.16: Reflectivity of the multilayer mirror at a grazing angle of 2.25°. The curve favors the 500 to 1000 eV energy range and has a second reflectivity peak at 1500 eV.

As mentioned previously, the zone plate focusing efficiencies of the first and third orders are 10% and 1.1%. Finally, if we wish to compare counts on the CCD we must consider that a 1560 eV photon will create three times as many electron-hole pairs as a 520 eV photon. Considering all of these relative efficiencies, approximately 1.8% of the total CCD counts will be from 1560 eV X-rays.

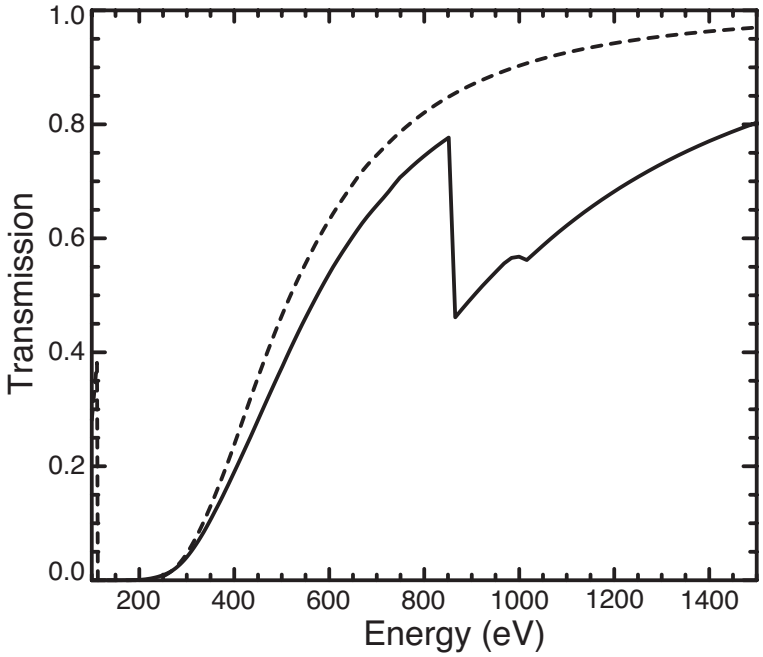

Figure 4.17: Plot of the transmission of the 0.5 μm thick beryllium window (dashed line) and the 200 nm thick aluminum coated Si_3N_4 window (solid line).

4.3.2 Higher energy contamination simulation

Although the theoretical contamination of 1560 eV CCD counts is small compared to the 520 eV signal, let us ensure that such an energy contamination is in fact inconsequential by simulating such a diffraction pattern and recovering its phases. Simulations were done by constructing a sphere of β and δ for a fake cell composed of protein, lipids, and water in a cube of pure ice at 520 eV and 1560 eV using `tomo_buildcell.pro` written by Chris Jacobsen. The volumes of ice had dimensions more than twice the length as the simulated cell to ensure proper sampling of the autocorrelation of the image (Sec. 2.2.2). Coherent diffraction intensities with photon noise added were calculated using `tomo_multiprop.pro` also written by Chris Jacobsen for both 520 eV and 1560 eV. The diffraction intensities were then added together with 90% scattering contribution from 520 eV and 10% from 1560 eV. The reconstructions were performed using Difference Map for 200 iterations then the supports were updated automatically using `Shrinkwrap` twice with 20 iterations in between. Difference Map was then continued for 10 iterations before averaging every second iteration for another 300 iterations. The original supports were determined in an automated fashion by thresholding the autocorrelation and reducing the size by half in each dimension.

Figure 4.18 shows the resulting reconstructed wave fields with (B) and without (A) 10% of the simulated CCD counts from the scattering of 1560 eV X-rays. Despite the higher energy scattering information, the phase retrieval algorithm is able to find a good support estimate and the reconstructed phases look similar to those from a diffraction pattern with pure 520 eV incident X-rays. Both reconstructions are of somewhat poor quality for simulated data because of a number of reasons. First the support guesses were found in a completely automated fashion and only one random phase start was used for each reconstruction. Furthermore, the simulated cell is very round with nothing to break its symmetry such as a nearby point scatterer. Therefore, the reconstruction contains the object and its enantiomorph both of which are valid solutions to the simulated diffraction intensities.

The Wiener filtered phase retrieval transfer functions (wPRTF) in Fig. 4.19 of the two reconstructions show that the missing phases have been reconstructed equally well. The variations between the pure 520 eV curve shown in gray and the red curve from reconstructing scattered intensity with 1560 eV contamination are no more than what is expected from two independent random phase starts with two independently determined support constraints. The plummeting of the wPRTF curves around 30 nm is due to the limited features with dimensions below that length scale. The signal-to-noise ratio decreases because very little scattered information extends to those high spatial

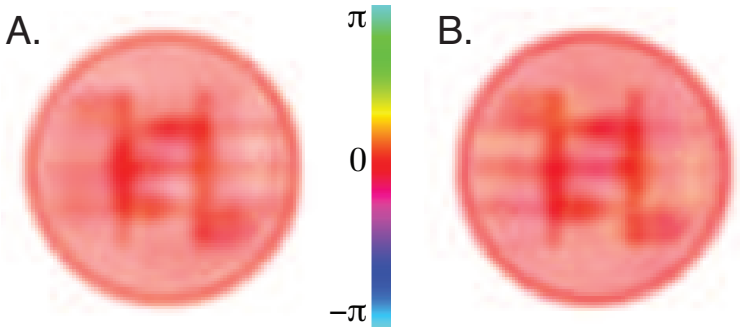

Figure 4.18: Complex display of reconstructed wave field from a simulated cell in ice with (A) no higher energy contamination and (B) with 10% of the total CCD counts from 1560 eV using support constraints which were found using `Shrinkwrap`. There appears to be no adverse effects from moderately low contaminated scatter from 1560 eV X-rays. Both reconstructed wavefields contain the object and its enantiomorph since the envelope of the object is symmetric.

frequencies. Noise dominates the PRTF curves after the drop; however, the Wiener filter successfully suppresses the noisy signal.

We have established that the theoretically calculated CCD counts from the 1560 eV energy is less than 2% of the total counts and simulations have shown no adverse effects on reconstruction quality from coherent diffraction intensity patterns with 10% CCD counts from 1560 eV. Thus, we can conclude that the modifications to the beamline since the collection of data from the frozen hydrated sample that could be reconstructed should not be a cause for the inability to reconstruct recently measured frozen hydrated diffraction data.

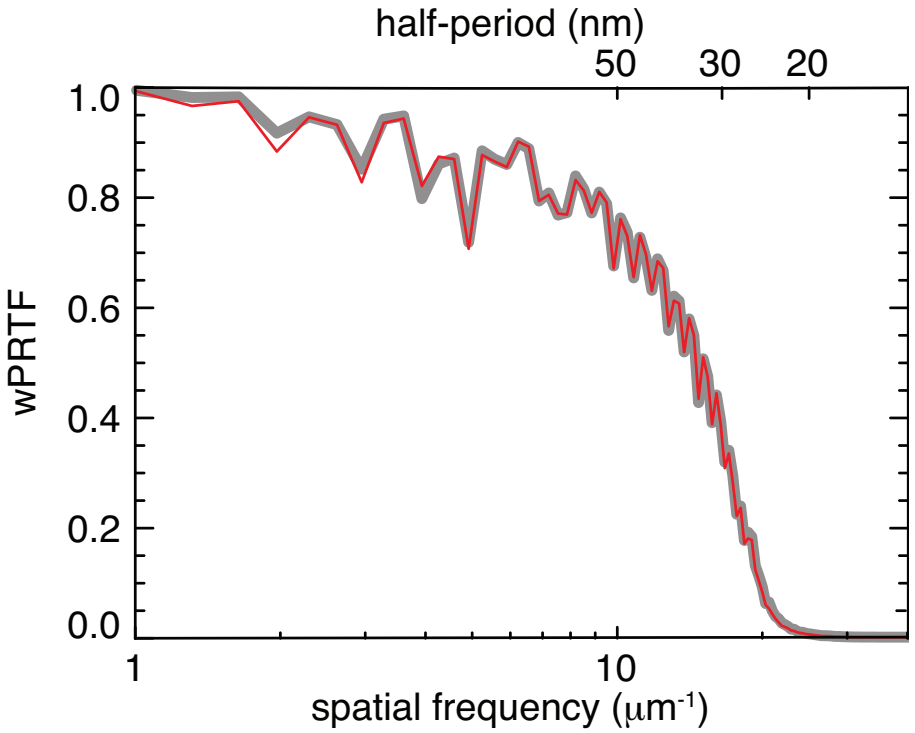

Figure 4.19: Wiener filtered Phase retrieval transfer function of reconstructed cell in ice with no higher energy contamination (gray) and with 10% of total CCD counts from 1560 eV (red). The variation in wPRTF curves is no more than is expected from two independent random phase starts with two independently determined support constraints.

Chapter 5

Outlook

High resolution imaging of whole eukaryotes both freeze-dried [19, 52] and frozen hydrated [55] has been shown to be feasible in 2D using x-ray diffraction microscopy. Thus far we have had significantly more success in achieving high resolution, high contrast micrographs of room temperature, freeze-dried yeast in comparison to the more biologically relevant frozen hydrated yeast. Beyond the expected challenges typical of imaging frozen hydrated specimens, we have found coherent scattering from surrounding ice which violates the isolated specimen assumption of the phase retrieval algorithm to be the largest hurdle. Significant upgrades to our microscope have been implemented as well as the capability of preview frozen specimen grids at low resolution (Sec. 4.2).

One possible means of overcoming ice background scatter is to eliminate the need for an isolated specimen. A recent development in x-ray microscopy combines the scanning feature of a STXM with the reconstruction of scattered intensity patterns of XDM. Scanning XDM replaces the compact support constraint with an overlapping illumination constraint. If successfully implemented on frozen hydrated specimens, it would retrieve the lost phase information of both the specimen and the ice background. Furthermore, it is not limited to isolated cells so tissue samples could also be considered. A brief discussion of this technique is given in Sec. 5.1.

In addition to high resolution imaging of whole, hydrated eukaryotes in 2D, we wish to extend this imaging technique into the third dimension. With 3D imaging, the positive identification of specific organelles is more feasible because comparative densities are known as well as their relative orientation in 3D. Furthermore, there is no longer the added complication of overlapping information from projecting a 3D object into a 2D image. Unlike lens-based imaging with its diverging illumination, XDM using a plane wave illumination has reconstructed information from all focal planes at equal strengths. This overlapping information can significantly reduce contrast in 2D images. In

Sec. 5.2 an overview of 3D x-ray diffraction microscopy is given.

5.1 Scanning x-ray diffraction microscopy

Scanning x-ray diffraction microscopy (SXDM) is often referred to as *ptychography*, the name given to a similar yet noniterative technique of overlapping illumination fields first investigated by Hoppe in electron crystallography [66]. SXDM requires the collection of coherent diffraction intensities from overlapping illumination areas on the specimen. This overlap of illuminated regions replaces the support constraint in standard full-field XDM. The iterative *ptychography* technique was first demonstrated by Rodenburg *et al.* using He–Ne laser light in 2006 [67] and then with hard x-rays in the following year [68].

More recently it has been shown that the illumination probe need not be known completely, but a starting guess can be given to the algorithm and this guess will be updated as the phases of the object are found [69, 70]. The reconstruction of the probe can then be used to speed up subsequent reconstructions of more difficult specimens if the illumination does not change significantly. For example one can conceive of performing SXDM on a strongly scattering object such as gold balls of various sizes. Immediate afterwards, SXDM data can be recorded on a more weakly scattering biological specimen. This technique has yet to be demonstrated.

The first successful use of SXDM on a biological specimen was of unstained, whole freeze-dried *Deinococcus radiodurans* by Giewekemeyer *et al.* [71]. A resolution of approximately 85 nm was achieved, limited by the poor signal-to-noise ratio of the high spatial frequency information collected.

Although not yet realized, by using SXDM one can take advantage of the additional information that can be collected in a scanning system. For example, by using hard x-rays the collection of x-ray fluorescence can give trace elemental maps of metals that are important in subcellular processes [72]. This lower resolution fluorescence information could be recorded simultaneously with the high resolution SXDM information which minimizes the required dose for the combined information.

Scanning XDM does not come without additional complications. The simplicity of the plane wave XDM setup has the benefit of requiring minimal alignment of optics and is extremely forgiving with respect to vibrations and thermal drifts in the system. Since a translation of the object only changes the phase of the far-field diffraction pattern, an object can drift as much as $\sim 10\ \mu$m without changing the measured diffraction intensities except perhaps the overall scaling if the specimen is no longer illuminated by the most intense

region of the x-ray beam. On the other hand, scanning systems require significantly more stability between the specimen and the illumination because the beam footprint on the specimen is much smaller. Furthermore, the algorithm uses the overlap of illumination as a known parameter. If the scanning motors are not reliable that overlap will not be consistent.

Our current microscope is not equipped for high resolution scanning so we have had limited success thus far on recording SXDM intensity information. For details about these experiments see [20]. In addition, a CCD detector is very poor at collecting large dynamic range diffraction intensity patterns. As described in Sec. 2.3, we must move our beamstop and corner around to collect the full range of information. Significant time is wasted by these motor movements, making SXDM very slow. A large dynamic range, low noise detector is imperative for routine SXDM experiments.

5.2 3D x-ray diffraction microscopy

It has been shown that XDM can be naturally extended to 3D [22, 73]. Coherent diffraction intensity patterns are collected at different specimen angles and then combined into a single 3D diffraction cube in reciprocal space. The same iterative phase retrieval algorithms can be applied to reconstruct the objects phases in 3D. Although the technique has been demonstrated on air-dried human chromosomes by Nishino *et al.*, the achieved resolution was severely limited by radiation dose [74]. To successfully image eukaryotic cells in 3D to a high resolution, we must image at cryogenic temperatures.

Our current microscopy is fully equipped to record high resolution 3D XDM intensity data and we have collected 3D data on both room temperature, non-biological samples (such as nonporous glass and carbon) and frozen hydrated yeast. Violation of the isolated support constraint has made phase retrieval of these specimens difficult, especial since the beam footprint on the specimen elongates at the very high tilt angles. To avoid the x-ray beam scattering from a grid support bar, we must used EM grids with very widely spaced support bars. Such wide spacing requires the transparent substrate on the grid to span much longer distances, adding to the likelihood that sections of the substrate will break during plunge freezing or handling of the frozen grid.

As with the scanning XDM, full 3D data collection is very time consuming without a large dynamic range detector. We have begun an effort to perform quick, low resolution phase retrieval in 2D as data is collect and have demonstrated that such reconstructions can be performed in a timely fashion (Turner *et al.*, manuscript in preparation). The idea is to evaluate the quality of a specimen with a 2D reconstruction before determining if the specimen is

of high enough quality to collect 3D data. The newly developed automated merging program (AMP), used in Sec. 3.2.1 and described in detail in [20, 47], allows quick merging of diffraction data which is required for such online 2D reconstructions.

Bibliography

[1] Attwood, DT, Henke, BL, eds (1981) *Low Energy X-ray Diagnostics* (American Institute of Physics, New York) Vol. 75 Monterey, 1981.

[2] Thompson, A et al. (2001) X-ray data booklet. (Lawrence Berkeley National Laboratory, University of California, Berkeley, CA 94720) Online at http://xdb.lbl.gov/.

[3] Born, M, Wolf, E (1999) *Principles of Optics* (Cambridge University Press, Cambridge), Seventh edition.

[4] Kirz, J, Jacobsen, C, Howells, M (1995) Soft x-ray microscopes and their biological applications. *Quarterly Reviews of Biophysics* 28:33–130.

[5] Henke, BL, Gullikson, EM, Davis, JC (1993) X-ray interactions: Photoabsorption, scattering, transmission, and reflection at E=50–30,000 eV, Z=1–92. *Atomic Data and Nuclear Data Tables* 54:181–342.

[6] Langmore, JP, Smith, MF (1992) Quantitative energy-filtered electron microscopy of biological molecules in ice. *Ultramicroscopy* 46:349–373.

[7] Hecht, E (1987) *Optics* (Addison-Wesley, Reading, Massachusetts), Second edition.

[8] AtreNet (2010) Xradia: Products - X-ray optics - zone plates. http://www.xradia.com/products/xray-optics/zone-plates.php.

[9] Beetz, T (2004) Ph.D. thesis (Department of Physics and Astronomy, Stony Brook University).

[10] Heim, S, Guttmann, P, Rehbein, S, Werner, S, Schneider, G (2009) Energy-tunable full-field x-ray microscopy: Cryo-tomography and nano-spectroscopy with the new BESSY TXM. *Journal of Physics: Conference Series* 186:012041.

[11] Chao, W, Kim, J, Rekawa, S, Fischer, P, Anderson, E (2009) Demonstration of 12 nm resolution Fresnel zone plate lens based soft x-ray microscopy. *Optics Express* 17:17669–17677.

[12] Okada, S (1970) in *Radiation Biochemistry*, eds Altman, KI, Gerber, GB, Okada, S (Academic Press, New York) Vol. I.

[13] Maser, J et al. (2000) Soft x-ray microscopy with a cryo STXM: I. Instrumentation, imaging, and spectroscopy. *Journal of Microscopy* 197:68–79.

[14] Howells, M et al. (2009) An assessment of the resolution limitation due to radiation-damage in x-ray diffraction microscopy. *Journal of Electron Spectroscopy and Related Phenomena* 170:4–12.

[15] Beetz, T, Jacobsen, C (2003) Soft x-ray radiation-damage studies in PMMA using a cryo-STXM. *Journal of Synchrotron Radiation* 10:280–283.

[16] Barker, AI, Southworth-Davies, RJ, Paithankar, KS, Carmichael, I, Garman, EF (2009) Room-temperature scavengers for macromolecular crystallography: increased lifetimes and modified dose dependence of the intensity decay. *Journal of Synchrotron Radiation* 16:205–216.

[17] Schneider, G (1998) Cryo x-ray microscopy with high spatial resolution in amplitude and phase contrast. *Ultramicroscopy* 75:85–104.

[18] Huang, X (2009) Ph.D. thesis (Department of Physics and Astronomy, Stony Brook University).

[19] Nelson, J et al. (2010) High-resolution x-ray diffraction microscopy of specifically labeled yeast cells. *Proceedings of the National Academy of Sciences* 107:7235–7239.

[20] Steinbrener, J (2010) Ph.D. thesis (Department of Physics and Astronomy, Stony Brook University).

[21] Huang, X et al. (2009) Signal-to-noise and radiation exposure considerations in conventional and diffraction x-ray microscopy. *Optics Express* 17:13541–13553.

[22] Chapman, H et al. (2006) High resolution *ab initio* three-dimensional x-ray diffraction microscopy. *Journal of the Optical Society of America A* 23:1179–1200.

[23] Sayre, D (1952) Some implications of a theorem due to Shannon. *Acta Crystallographica* 5:843.

[24] Goodman, JW (1968) *Introduction to Fourier Optics* (McGraw-Hill, San Francisco).

[25] Nyquist, H (1928) Certain topics in telegraph transmission theory. *Trans. AIEE* 47:617–644.

[26] Shannon, C (1949) Communication in the presence of noise. *Proceedings of the Institute of Radio Engineers* 37:10–21.

[27] Spence, J, Howells, M (2002) Synchrotron soft x-ray and field-emission electron sources: a comparison. *Ultramicroscopy* 93:213–222.

[28] Miao, H (2008) Ph.D. thesis (Department of Physics and Astronomy, Stony Brook University).

[29] Gerchberg, RW, Saxton, WO (1972) A practical algorithm for the determination of phase from image and diffraction plane pictures. *Optik* 35:237–246.

[30] Fienup, J (1978) Reconstruction of an object from the modulus of its Fourier transform. *Optics Letters* 3:27–29.

[31] Fienup, J (1987) Reconstruction of a complex-valued object from the modulus of its Fourier-transform using a support constraint. *Journal of the Optical Society of America A* 4:118–123.

[32] Bates, RHT (1982) Fourier phase problems are uniquely solvable in more than one dimension. I. Underlying theory. *Optik* 61:247–262.

[33] Fienup, J (1982) Phase retrieval algorithms: a comparison. *Applied Optics* 21:2758–2769.

[34] Elser, V (2003) Phase retrieval by iterated projections. *Journal of the Optical Society of America A* 20:40–55.

[35] Luke, D (2005) Relaxed averaged alternating reflections for diffraction imaging. *Inverse Problems* 21:37–50.

[36] Marchesini, S (2004) Benchmarking iterative projection algorithms for phase retrieval. *arXiv:physics/0404091v1.*

[37] Williams, G, Pfeifer, M, Vartanyants, I, Robinson, I (2007) Effectiveness of iterative algorithms in recovering phase in the presence of noise. *Acta Crystallographica A* 63:36–42.

[38] Beetz, T et al. (2005) Apparatus for x-ray diffraction microscopy and tomography of cryo specimens. *Nuclear Instruments and Methods in Physics Research A* 545:459–468.

[39] Howells, M, Charalambous, P, He, H, Marchesini, S, Spence, J (2002) *An off-axis zone-plate monochromator for high-power undulator Radiation* ed Mancini, D (SPIE), Vol. 4783, pp 65–73.

[40] Broennimann, C et al. (2006) The PILATUS 1M detector. *Journal of Synchrotron Radiation* 13:120–130.

[41] Denk, W, Strikler, JH, Webb, WW (1990) Two-photon laser scanning fluorescence microscopy. *Science* 248:73–76.

[42] Hell, S (2007) Far-field optical nanoscopy. *Science* 316:1153–1158.

[43] Grimm, R et al. (1997) Energy filtered electron tomography of ice-embedded actin and vesicles. *Biophysical Journal* 72:482–489.

[44] Jorgensen, P, Nishikawa, JL, Breitkreutz, BJ, Tyers, M (2002) Systematic identification of pathways that couple cell growth and division in yeast. *Science* 297:395–400.

[45] Tkacz, J, Barbara Cybulska, E, Lampen, J (1971) Specific staining of wall mannan in yeast cells with fluorescein-conjugated concanavalin A. *Journal of Bacteriology* 105:1–5.

[46] Steinbrecht, RA, Zierold, K, eds (1987) *Cryotechniques in Biological Electron Microscopy* (Springer-Verlag, Berlin).

[47] Steinbrener, J et al. (2010) High fidelity reconstructions in x-ray diffraction microscopy. *Optics Express* (Accepted).

[48] Shapiro, D (2004) Ph.D. thesis (Department of Physics and Astronomy, Stony Brook University).

[49] Thibault, P, Elser, V, Jacobsen, C, Shapiro, D, Sayre, D (2006) Reconstruction of a yeast cell from x-ray diffraction data. *Acta Crystallographica A* 62:248–261.

[50] Marchesini, S et al. (2003) X-ray image reconstruction from a diffraction pattern alone. *Physical Review B* 68:140101.

[51] Chen, CC, Miao, J, Wang, CW, Lee, TK (2007) Application of optimization technique to noncrystalline x-ray diffraction microscopy: Guided hybrid input-output method. *Physical Review B* 76.

[52] Shapiro, D et al. (2005) Biological imaging by soft x-ray diffraction microscopy. *Proceedings of the National Academy of Science* 102:15343–15346.

[53] Spence, J, Weierstall, U, Howells, M (2002) Phase recovery and lensless imaging by iterative methods in optical, x-ray and electron diffraction. *Philosophical Transactions of the Royal Society of London A* 360:875–895.

[54] Marchesini, S (2007) Quantitative biological imaging by ptychographic x-ray dffraction microscopy. *Review of Scientific Instruments* 78:011301.

[55] Huang, X et al. (2009) Soft x-ray diffraction microscopy of a frozen hydrated yeast cell. *Physical Review Letters* 103:198101.

[56] Lima, E et al. (2009) Cryogenic x-ray difrraction microscopy for biological samples. *Physical Review Letters* 103:198102.

[57] O'Toole, E, Wray, G, Kremer, J, McIntosh, JR (1993) High voltage cryomicroscopy of human blood platelets. *Journal of Structural Biology* 110:55–66.

[58] Jacobsen, C, Medenwaldt, R, Williams, S (1998) *A perspective on biological x-ray and electron microscopy* eds Thieme, J, Schmahl, G, Umbach, E, Rudolph, D (Springer-Verlag, Berlin), pp II–93–102.

[59] Larabell, C, Le Gros, M (2004) X-ray tomography generates 3-D reconstructions of the yeast, *Saccharomyces cerevisiae*, at 60-nm resolution. *Molecular Biology of the Cell* 15:957–962.

[60] Dubochet, J et al. (1988) Cryo-electron microscopy of vitrified specimens. *Quarterly Reviews of Biophysics* 21:129–228.

[61] Bachmann, L, Mayer, E (1987) in Steinbrecht and Zierold [46] pp 3–34.

[62] Sitte, H, Edelmann, L, Neumann, K (1987) in Steinbrecht and Zierold [46] pp 87–113.

[63] Talmon, Y (1987) in Steinbrecht and Zierold [46] pp 64–84.

[64] Miao, H et al. (2009) Cryo diffraction microscopy: Ice conditions and finite supports. *Journal of Physics: Conference Series* 186:012055.

[65] Lima, E (2006) Ph.D. thesis (Department of Physics and Astronomy, Stony Brook University).

[66] Hoppe, W (1969) Beugung im inhomogenen Primärstrahlwellenfeld. I. Prinzip einer Phasenmessung von Elektronenebeugungsinterferenzen. *Acta Crystallographica* A 25:495–501.

[67] Rodenburg, J, Hurst, A, Cullis, A (2006) Transmission microscopy without lenses for objects of unlimited size. *Ultramicroscopy* 107:227–231.

[68] Rodenburg, J et al. (2007) Hard-x-ray lensless imaging of extended objects. *Physical Review Letters* 98:034801.

[69] Thibault, P et al. (2008) High-resolution scanning x-ray diffraction microscopy. *Science* 321:379–382.

[70] Thibault, P, Dierolf, M, Bunk, O, Menzel, A, Pfeiffer, F (2009) Probe retrieval in ptychographic coherent diffractive imaging. *Ultramicroscopy* 109:338–343.

[71] Giewekemeyer, K et al. (2010) Quantitative biological imaging by ptychographic x-ray diffraction microscopy. *Proceedings of the National Academy of Sciences* 107:529–534.

[72] Paunesku, T, Vogt, S, Maser, J, Lai, B, Woloschak, G (2006) X-ray fluorescence microprobe imaging in biology and medicine. *Journal of Cellular Biochemistry* 99:1489–1502.

[73] Barty, A et al. (2008) Three-dimensional coherent x-ray diffraction imaging of a ceramic nanofoam: Determination of structural deformation mechanisms. *Physical Review Letters* 101:055501.

[74] Nishino, Y, Takahashi, Y, Imamoto, N, Ishikawa, T, Maeshima, K (2009) Three-dimensional visualization of a human chromosome using coherent x-ray diffraction. *Physical Review Letters* 102:018101.

[75] Thibault, P (2007) Ph.D. thesis (Department of Physics, Cornell University).

[76] Miao, J et al. (2003) Imaging whole *escherichia coli* bacteria by using single-particle x-ray diffraction. *Proceedings of the National Academy of Sciences* 100:110–112.

[77] Jiang, H et al. (2008) Nanoscale imaging of mineral crystals inside biological composite materials using x-ray diffraction microscopy. *Physical Review Letters* 100:038103.

[78] Song, C et al. (2008) Nanoscale imaging of buried structures with elemental specificity using resonant x-ray diffraction microscopy. *Physical Review Letters* 100:025504.

[79] Williams, G et al. (2008) High-resolution x-ray imaging of *Plasmodium falciparum*-infected red blood cells. *Cytometry Part A* 73A:949–957.

Appendix A

Far-field scattering in the Born approximation

Consider a plane wave propagating in the positive z direction $\psi_0 e^{-\mathrm{i}k\hat{\boldsymbol{z}}\cdot\boldsymbol{r}}$ incident on an object of inhomogeneous material with complex refractive index $\tilde{n}$ (Fig. A.1) that satisfies the wave equation

$$\nabla^2\psi(\boldsymbol{r}) + k^2\tilde{n}^2(\boldsymbol{r})\psi(\boldsymbol{r}) = 0. \tag{A.1}$$

The scattering by the object can be written as

$$\psi(\boldsymbol{r}) = \int o(\boldsymbol{r}')\psi(\boldsymbol{r}')\frac{e^{\mathrm{i}k|\boldsymbol{r}-\boldsymbol{r}'|}}{|\boldsymbol{r}-\boldsymbol{r}'|}\mathrm{d}^3\boldsymbol{r}', \tag{A.2}$$

where $o(\boldsymbol{r}')$ is the refractive index dependent scattering potential (see for example Born and Wolf [3]). Assuming far-field limit we can simplify the scattered wave as

$$\psi(\boldsymbol{r}) = \frac{e^{ik|\boldsymbol{r}|}}{|\boldsymbol{r}|}\int o(\boldsymbol{r}')\psi(\boldsymbol{r}')e^{\mathrm{i}k\boldsymbol{r}'\cdot\hat{\boldsymbol{r}}}\mathrm{d}^3\boldsymbol{r}', \tag{A.3}$$

where we have assumed that the distance $|\boldsymbol{r}| \gg |\boldsymbol{r}'|$ and the scattering potential is

$$o(\boldsymbol{r}) = \frac{k^2}{4\pi}[1 - n^2(\boldsymbol{r})] \simeq \frac{k^2}{2\pi}[\delta(\boldsymbol{r}) + \mathrm{i}\beta(\boldsymbol{r})]. \tag{A.4}$$

To further simplify Eq. A.3 one can assume that the object scatters weakly such that the scattering is only of the incident wave $\psi(\boldsymbol{r}') \simeq \psi_0 e^{-\mathrm{i}k\hat{\boldsymbol{z}}\cdot\boldsymbol{r}}$. This approximation is called the first-order Born approximation and is valid when the refractive index is near unity.

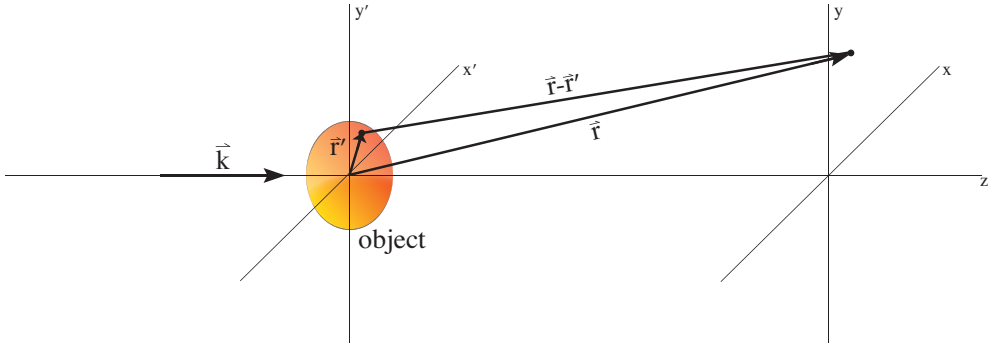

Figure A.1: Diagram of scattering of a plane wave $\psi_0 e^{-\mathrm{i}k\hat{\boldsymbol{z}}\cdot\boldsymbol{r}}$ off an object. For the far-field limit, the distance $|\boldsymbol{r}| \gg |\boldsymbol{r}'|$.

Using the first-order Born approximation, the scattering in the far-field is

$$\psi(\boldsymbol{r}) \simeq \psi_0 \frac{e^{\mathrm{i}kz}}{z} \int o(\boldsymbol{r}') e^{-\mathrm{i}k(\hat{\boldsymbol{z}}-\hat{\boldsymbol{r}})\cdot\boldsymbol{r}'} \mathrm{d}^3\boldsymbol{r}', \tag{A.5}$$

where $|\boldsymbol{r}| \simeq z$ for small angle scattering. In Cartesian coordinates $(\hat{\boldsymbol{z}} - \hat{\boldsymbol{r}}) \cdot \boldsymbol{r}' = \frac{xx'}{|\boldsymbol{r}|} + \frac{yy'}{|\boldsymbol{r}|} \simeq \frac{xx'}{z} + \frac{yy'}{z}$; therefore, we can write the scattering as

$$\psi(x, y, z) \simeq \psi_0 \frac{e^{\mathrm{i}kz}}{z} \int_{x'} \int_{y'} o(x', y') e^{-\mathrm{i}k(\frac{xx'}{z} + \frac{yy'}{z})} \mathrm{d}x' \mathrm{d}y'. \tag{A.6}$$

Now Eq. A.6 can be rewritten such that the Fourier transform property of far-field diffraction scattering is evident. The rewrite is

$$\begin{aligned} \psi(x, y, z) &\simeq \psi_0 \frac{e^{\mathrm{i}kz}}{z} \int_{x'} \int_{y'} o(x', y') e^{-\mathrm{i}2\pi(f_x x' + f_y y')} \mathrm{d}x' \mathrm{d}y' \\ &\equiv \psi_0 \frac{e^{\mathrm{i}kz}}{z} \mathcal{F}\{o(x', y')\} = \psi_0 \frac{k^2 e^{\mathrm{i}kz}}{2\pi z} \mathcal{F}\{\delta(x', y') + \mathrm{i}\beta(x', y')\}, \end{aligned} \tag{A.7}$$

where $f_x = \frac{x}{\lambda z}$ and $f_y = \frac{y}{\lambda z}$ are spatial frequencies. The CCD detector measures only the scattered intensity

$$I(x, y) = |\psi(x, y)|^2 = \psi_0^2 \frac{k^2}{4\pi^2 z^2} \Big| \mathcal{F}\{\delta(x', y') + \mathrm{i}\beta(x', y')\} \Big|^2. \tag{A.8}$$

Appendix B

Phase retrieval algorithms

Two algorithms Difference Map (DM) and Hybrid Input-Output (HIO) are described in detail below. As was shown by Elser [34], HIO can be formulated such that it is a special case of DM. Generally DM can be thought to search the parameter space more intelligently and in a manner more suited to avoiding local minima; however, a single DM iteration requires twice as many Fourier transforms as HIO. We chose to compare these two specific algorithms because DM is our preferred phase retrieval method while HIO is used by a larger number of researchers. Often HIO is used in combination with ER to rein in its "wandering" behavior [75]; however, this approach was not used in our experiments because it can give misleading results when multiple equally valid solutions are possible. This combined approach will more likely zero in on one of many solutions while HIO and DM alone will wander between many different, but equally likely solutions. These equally likely solutions are then averaged together in an attempt to form a solution where consistencies between solutions are constructively reenforced while inconsistencies are averaged out (Sec. 3.3.2).

B.1 Difference Map

The Difference Map algorithm is based on the idea of adding weighted differences of differently ordered projections to the current iterate, where a projection is the mapping of current points onto a constraint set using the shortest distance. A complete, mathematically rigorous definition can be found in [75]. The $(n+1)^{\text{th}}$ DM iterate is defined as

$$x_{n+1} = x_n + \beta(y_2 - y_1), \tag{B.1}$$

where

$$y_1 = P_1[(1+\gamma_2)P_2(x_n) - \gamma_2 x_n], \quad y_2 = P_2[(1+\gamma_1)P_1(x_n) - \gamma_1 x_n], \tag{B.2}$$

and β, γ_1, and γ_2 can be complex, but are generally defined as real, and P_i is a projection. The standard convention is to set the parameters such that

$$\gamma_1 = \beta^{-1} \text{ and } \gamma_2 = -\beta^{-1}. \tag{B.3}$$

In all of the experiments and simulations performed for this work β is set to -1.15.

Typically we use the following two projections: the modulus projection, P_{M}, which replaces the current Fourier magnitudes with those that were measured and the support projection, P_{S}, which leaves positive information inside the object's support region untouched while setting everything outside of the region and any negative values inside the support to zero. With the freeze-dried yeast and other specimens whose phase shift is less than π we also constrained the imaginary part inside the support region to be nonnegative.

The algorithm converges when a fixed point is found, although the fixed point (x_i) itself may not be a solution. Typically the current Fourier projection is taken as the solution since the Fourier magnitudes are well known. If the solution is also an intersection of the two parameters (very unlikely with real data) then the support projection will equal the Fourier projection.

B.2 Hybrid Input-Output

The Hybrid Input-Output algorithm can also be written in terms of projections as

$$x_{n+1} = x_n + \beta(y_2 - y_1), \tag{B.4}$$

where

$$y_1 = P_{\mathrm{M}}(x_n), \quad y_2 = P_{\mathrm{S}}[(1+\beta^{-1})P_{\mathrm{M}}(x_n) - \beta^{-1}x_n] \tag{B.5}$$

and P_{M} and P_{S} are the the modulus and support projections. Note that HIO is a special case of DM where $\gamma_1 = \beta^{-1}$ and $\gamma_2 = -1$. Similar to DM, the final solution is $P_{\mathrm{M}}(x_i)$ and not simply x_i.

Appendix C

Yeast preparation protocols

This section describes the protocols used to prepare the *Saccharomyces cerevisiae* yeast before imaging. Typically fresh yeast are grown in yeast peptone dextrose (YPD), immunolabeled if desired, fixed either chemically or in vitrified ice, and finally imaged in the frozen hydrated state or dehydrated either chemically or by sublimation.

C.1 Gold labeling protocols

It was found that the 1.8 nm gold labels produced the most reliable labeling; however, silver-enhancement is required to view the labels. The nanogold labels and the silver-enhancement kit with the initiator, moderator and activator solutions were purchased from Nanoprobes Incorporated (Yaphank, NY).

C.1.1 1.8 nm gold labeled conA with silver enhancement

This conjugate includes both a 1.8 nm gold label and a Texas Red fluorophore.

1. Spin down yeast overnight and wash in water
2. Incubate with 0.5 mL conA reporter conjugate (full concentration) at room temperature for 1 hour on nutating mixer
3. Spin down cells and wash in water
4. Incubate with 0.5 mL buffer and 25 μL Texas Red conjugate at room temperature for 1 hour on nutating mixer

5. Spin down cells and wash in water
6. Cells can be visualized using excitation at 590 nm and emission at 617 nm (or Texas Red filter set) under fluorescence microscope to ensure labeling
7. Incubate with 0.5 mL of the initiator solution (15 mL vial with purple cap) at room temperature for 5-10 minutes
8. Spin down cells and wash in water
9. Incubate with equal volumes of the initiator and moderator (15 mL vial with green cap) , and activator (15 mL vial with yellow cap) solutions for up to 20 minutes depending on desired silver development (can be visualized under a visible light microscope every 5 minutes to track silver development)
10. Spin down cells and wash a few times in water

Buffer solution:
50 μL 1M tris (tris(hydroxymethyl)aminomethane) (pH 8.0)
10 μL 10% BSA (bovine serum albumin)
2.5 μL 50% PEG (Polyethylene glycol)
0.5 mL 50% glycerol
9.5 mL water
Buffer solution does not keep once BSA is added.

C.1.2 Biotin-conA with 40 nm gold labeled streptavidin

1. Spin down yeast overnight and wash in water
2. Re-suspend in 0.5 mL PBS (phosphate buffered saline) and 50 μL biotin-conA
3. Incubate 1 hour at room temperature on nutating mixer
4. Spin down cells and wash in water
5. Re-suspend in 0.5 mL gold conjugate dilution buffer and 50 μL gold labeled streptavidin
6. Incubate 1 hour at room temperature on nutating mixer
7. Spin down cells and wash in water

C.1.3 10 nm gold labeled conA

1. Spin down *whi5* overnight and wash in water
2. Re-suspend in 0.5 mL buffer and 25 μL gold labeled conA
3. Incubate 1 hour at room temperature on nutating mixer
4. Spin down cells and wash in water

Buffer Solution:
2 mL 20× PBS
16 mL 50% glycerol
22 mL water

C.2 Chemical drying protocol for scanning electron microscope

1. Fix cells by suspending with 3% glutaraldehyde in Na^+ cacodylate for 1 hour at room temperature or 37% formaldehyde in YPD for 30 minutes at room temperature
2. Break silicon nitride wafer into fragments and allow poly-lysne to dry on them
3. Wash cells in water and resuspend in water
4. Pipette cell solution onto wafer fragments and let stand for 5 minutes
5. Wash wafer fragments with water
6. Dehydrate wafter fragments with acetone series
    - 2 × 10 minutes in 30% acetone
    - 2 × 10 minutes in 50% acetone
    - 2 × 10 minutes in 70% acetone
    - 2 × 10 minutes in 90% acetone
    - 2 × 10 minutes in 100% acetone
7. Critical point dry by washing 3× in hexamethyldisilazane (HMDS)

8. Do not sputter coat wafer fragments before imaging

Na^+ cacodylate:
2 mL 1M NaCu
0.1 mL 1M $CaCl_2$

C.3 Freeze-drying protocol for x-ray diffraction microscopy

1. Dilute cells with water to proper concentration
2. Pipette cell solution on formvar-coated, carbon stabilized electron microscopy grid and let stand for 1–5 minutes
3. Plunge into liquid ethane with manual blot plunge freezer or automatic blot FEI vitrobot (Hillsboro, OR)
4. Keep grid either under liquid nitrogen or in cold ($< -140°C$), dry nitrogen gas.
5. Freeze-dry grids in a cooled, evacuated EMS775X turbo freeze-drier from Electron Microscopy Sciences (Hatfield, PA), see page 58 of [48] for a standard freezing protocol
6. Store grids away from moisture to keep from rehydration

Appendix D

Fresnel Propagation

Here we describe the procedure for Fresnel or near-field propagation of a coherent wave traveling from one plane to another. A wavefield traveling primarily in the z direction and propagating from $(x_0, y_0, z_0 = 0)$ to (x, y, z) can be represented as a plane wave at $z_0 = 0$ modulated by a function $g(x_0, y_0)$. We can then treat the wavefield at $z_0 = 0$ as the sum of Huygens point sources or spherical wavelets $\psi = \frac{\psi_0}{r} e^{-\mathrm{i}kr}$, with each point source modulated by its value of $g(x_0, y_0)$. In the Cartesian system this modulation of the sum of many spherical wavelets can be expressed as

$$\psi(x, y, z) = \psi_0 \frac{\lambda}{A} \int_{x_0} \int_{y_0} g(x_0, y_0) \frac{e^{-\mathrm{i}kr}}{r} \cos\theta \, \mathrm{d}x_0 \, \mathrm{d}y_0, \tag{D.1}$$

where the $1/A$ area term is required to cancel the integration over x_0 and y_0 and the $\cos\theta$ is the obliquity factor, which describes the directionality of the wavelets and can typically be ignored. To simplify let us perform a binomial expansion on $r = \sqrt{(x - x_0)^2 + (y - y_0)^2 + z^2}$, which is written as

$$\begin{aligned} r &= z\sqrt{1 + \left(\frac{x - x_0}{z}\right)^2 + \left(\frac{y - y_0}{z}\right)^2} && \text{(D.2)} \\ &= z\left[1 + \frac{(x - x_0)^2 + (y - y_0)^2}{2z^2} - \frac{(x - x_0)^4 + (y - y_0)^4}{8z^4} \ldots\right] && \text{(D.3)} \end{aligned}$$

(see for example Born and Wolf [3]). In the Fresnel approximation we can ignore the quadratic terms and higher. We can rewrite the Fresnel propagation of the wavefield as

$$\psi(x, y, z) = \psi_0 e^{\frac{-\mathrm{i}2\pi z}{\lambda}} \frac{\lambda}{z} \frac{1}{A} \int_{x_0} \int_{y_0} g(x_0, y_0) e^{\frac{-\mathrm{i}\pi}{\lambda z}[(x - x_0)^2 + (y - y_0)^2]} \, \mathrm{d}x_0 \, \mathrm{d}y_0. \tag{D.4}$$

The propagation of wavefield can be rewritten in terms of a convolution, which is defined as

$$f(x) * h(x) \equiv \int f(x)h(x-a)\mathrm{d}a \tag{D.5}$$

and has the property in reciprocal space such that

$$\mathcal{F}\{f(x) * h(x)\} = F(u)H(u), \tag{D.6}$$

where a capital letter refers to the Fourier transform of a function represented with the corresponding lowercase letter. We can write propagated wavefield as

$$\psi(x,y,z) = \psi_0 e^{\frac{-\mathrm{i}2\pi z}{\lambda}} \frac{\lambda}{z}\frac{1}{A}[g(x_0,y_0) * p(x_0,y_0)], \tag{D.7}$$

where $p(x_0, y_0)$ is the propagator function which is defined as

$$p(x_0,y_0) \equiv e^{\frac{-\mathrm{i}\pi}{\lambda z}(x_0^2+y_0^2)} \tag{D.8}$$

and in reciprocal space as

$$P(f_x,f_y) = e^{-\mathrm{i}\pi\lambda z(f_x^2+f_y^2)} = e^{\frac{-\mathrm{i}\pi}{\lambda z}(x^2+y^2)}. \tag{D.9}$$

As in Sec. 2.2.1, $f_x = \frac{x}{\lambda z}$ is a spatial frequency (the equivalent holds for f_y). Therefore, to Fresnel propagate a complex wave by a distance z, one can simply Fourier transform the wavefield, multiply by the Fresnel propagator $P(f_x, f_y)$, and then perform an inverse Fourier transform.

Appendix E

XDM resolutions summary

Pixel/Voxel Size	Resolution	Method of Determining Resolution
18 nm	30 nm	PSD inspection [76]
10 nm	30 nm	PRTF, consistency of ∼30 nm structures [52]
12 nm	24 nm	double the pixel size [77]
9.5 nm	22 nm	$q_{\max}$ of diffraction signal [78]
N/A	35 nm	reliably fit by algorithm, smallest feature [79]
20.5 nm	38 nm (2D) 120 nm (3D)	PRTF (plot not shown) [74]
17 nm	20 – 30 nm	PRTF and line scan of feature [55]
30 nm	$\leq$ 50 nm	feature size [56]
N/A [1]	85 nm	power law of PSD (PRTF ∼1) [71]
10.6 nm	11 – 13 nm	PRTF, 2D fit of feature [19]

Table E.1: Summary of all published x-ray diffraction microscopy (XDM) work on biological material beginning in 2003. Listed are the pixel or voxel size of the real-space image, the estimated resolution, and the method in which the resolution was estimated. The range of biological samples imaged dry at room temperature include single cells [19, 52, 71, 76, 79], viruses [78], bone [77], and chromosomes [74] with two examples of XDM on frozen hydrated cells [55, 56].

[1] This represents the first demonstration of scanning XDM on biological material.